University of Tennessee, Knoxville
Trace: Tennessee Research and Creative Exchange

Doctoral Dissertations | Graduate School

5-2019

Microstructural Characterization and Mechanical Behaviors of High Entropy Alloys at Room and Elevated-Temperatures

Shuying Chen
University of Tennessee, schen38@vols.utk.edu

Follow this and additional works at: https://trace.tennessee.edu/utk_graddiss

Recommended Citation

Chen, Shuying, "Microstructural Characterization and Mechanical Behaviors of High Entropy Alloys at Room and Elevated-Temperatures. " PhD diss., University of Tennessee, 2019.
https://trace.tennessee.edu/utk_graddiss/5416

This Dissertation is brought to you for free and open access by the Graduate School at Trace: Tennessee Research and Creative Exchange. It has been accepted for inclusion in Doctoral Dissertations by an authorized administrator of Trace: Tennessee Research and Creative Exchange. For more information, please contact trace@utk.edu.

Microstructural Characterization and Mechanical Behaviors of High Entropy Alloys at Room and Elevated-Temperatures

A Dissertation Presented for the

Doctor of Philosophy

Degree

The University of Tennessee, Knoxville

Shuying Chen

May 2019

Copyright © 2019 by Shuying Chen

All rights reserved..

DEDICATION

This work is dedicated to all my beloved family members, Bingjin Chen, Fengying Dong, Fuhui Chen, Chunjuan Ma, and Ruiyang Chen, for their encouragement, understand, and full support under any circumstances.

ACKNOWLEDGEMENTS

I would like to express my sincere gratitude to my major advisor, Prof. Peter K. Liaw, for their continuous academical and financial support of my Ph.D study and related research, as well as for his patience, motivation, and immense knowledge. It is a great honor for me to have him as my advisor, who is professional and knowledgeable, and one of the top pioneering scientists on high-entropy alloys. I really appreciate his guidance throughout the time of research and writing of this thesis.

Besides my advisors, I would like to thank my thesis committee members, Dr. Yanfei Gao, Dr. Thomas T. Meek, and Dr. Hairong Qi for their insightful comments and encouragement. I am grateful to Dr. Yang Ren from Argonne National Laboratory (ANL) at the ID-11 Advanced Photon Sources (APS) for synchrotron diffraction data analyses and Dr. Jianguo Wen from ANL at the Center for Nanoscale Materials (CNM) . My sincere thanks go to Dr. Jonathan Poplawsky and Dr. Wei Guo from Oak Ridge National Laboratory (ORNL), Dr. Xiandong Xu, Dr. Fan Zhang, and Dr. Mingwei Chen from Tohoku University for microstructural characterizations. I would like to thank Dr. Junwei Qiao from Taiyuan University of Technology, Mr. K.-K. Tseng, and Dr. Jien-Wei Yeh from National Tsing Hua University for providing the materials. I appreciated Dr. Michael Gao from National Energy Technology Laboratory and AECOM for thermodynamic calculations. I am grateful to Dr. Karin Dahmen at the University of Illinois at Urbana-Champaign for instructive support and discussion about my study on the intrinsic feature of serration behavior. I appreciate my great friends, Mr. Douglas E. Fielden of Mechanical

Systems Group, Mr. John Dunlap of Microscopy Facility, and all the stall of MSE department at University of Tennessee (UT) for their valuable help in the past five years.

I would also like to thank our group members and my friends for their kindness during my Ph.D. study. Many thanks to Dr. Xie Xie, Dr. Haoling Jia, Dr. Zhi Tang, Dr. Gian Song, Dr. Louis J. Santodonato, Dr. Bilin Chen, Dr. Haoyan Diao, Mr. Rui Feng, Mr. Chanho Lee, Mr. Shaoyu Wang, Mr. Peiyong Chen, Mr. Zongyang Lv, Mr. Xuesong Fan from Dr. Liaw's group; Dr. Wei Zhang, Dr. Tingkun Liu, Ms. Xue Wang, and Ms. Di Xie from Dr. Gao's group; Ms. Hui Wang and Mr. Zengquan Wang from Dr. Egami group, and Ms. Ling Wang from Dr. Zinkle's group at UT for their help in my research, and all the other friends who give me support and help.

I would like to acknowledge the financial support from the Department of Energy, Office of Fossil Energy, The US National Science Foundation (NSF) (CMMI-1100080, and DMR 1611180, and DMR) with program directors Dr. C. Cooper, Dr. G. Shiflet, and D. Farkas. National Energy Technology Laboratory (NETL) (DE-FE-0008855 and DE-FE-0011194) with Mr. Vito Cedro and Dr. J. Mullen as program managers.

ABSTRACT

High entropy alloys (HEAs) are proposed as solid-solution alloys containing five or more principal elements in equimolar or near-equimolar ratios, possessing a single crystal structure rather than several ordered phases. Several studies of HEAs have been performed, with focus on the mechanical behavior and characterization of microstructures. The mechanical behavior and properties of HEAs under various conditions, i.e., strain rates, grain sizes, and temperatures, exhibit great differences, such as strong work hardening, homogeneous macroscopic flow, and excellent compression or tension ductility with obvious serrations at room temperature, and partial or complete dynamic recrystallization at high temperatures. The strong and ductile single-phase body-centered-cubic (BCC) HfNbTaTiZr refractory high-entropy alloy (RHEA) is a potential structural material for high-temperature applications. The present work will focus the mechanical properties and serration behavior in HfNbTaTiZr HEAs, by applying transmission electron microscopy (TEM), atom probe tomography (APT), synchrotron diffraction, and scanning electron microscopy (SEM) to the study of plastic deformation and fatigue behaviors in HEAs under different conditions (covering a wide range of strain rates, temperatures, and tension behaviors), in order to reveal the underlying mechanisms of the plastic deformation for HEAs and to predict the fracture stress. Specifically, an anomaly in strain hardening was observed at elevated temperatures–the strain-hardening exponent decreases expectedly from 77 K to 298 K but reverts to an anomalous ascending trend afterwards. Flow serrations at 673 and 773 K implied the dynamic strain aging (DSA) as an extra strengthening mechanism contributing to the intensified strain hardening at elevated temperatures. The

superior fatigue properties during cyclic loading were investigated at room temperature, which present a series of substructures, including dislocation loops, jogs, and dislocation network. The resulting dislocation network was formed by the interaction between dislocations with different Burgers vectors, which can act as the obstacle to dislocation motion to strengthen the fatigue behavior and release the strain energy and stress concentration to improve the resistance to cyclic loading. Moreover, the recrystallization, grain growth and phase transformation of HfNbTaTiZr HEAs were investigated as well in the certain range of temperatures to better understand their grain growth kinetics and phase stability in body centered-cubic (bcc) HEAs, which will be helpful for the materials design and optimization.

TABLE OF CONTENTS

LIST OF TABLES

LIST OF FIGURES

CHAPTER I INTRODUCTION

1.1 Concept of HEAs

In the last decades, a new concept of materials, named HEAs, has been proposed and developed [1], attracting worldwide attention for their unique properties. Five or more principal elements, with equal or near-equal atomic percentages, are included in alloys, which can be distinguished from the conventional alloys, with one or two based elements as major constituents. Even though more than 5 elements, only single solid solutions could be formed. Criteria and calculations to predict the solid solution formation from thermodynamics viewpoint were proposed in published papers [13-15]. One important and accepted assumption was proposed by Takeuchi and Inoue [16], for multi-component alloy system: the difference in Gibbs free energy between soli- and liquid state, ΔG, could be expressed as:

$$\Delta G_{mix} = \Delta H_{mix} - T\,\Delta S_{mix} \quad (1)$$

where T is the absolute temperature, ΔH_{mix} is the enthalpy of mixing, and ΔS_{mix} is the entropy of mixing.

To simplify the calculation, the enthalpy of mixing for multi-component alloys with n elements could be determined by the form:

$$\Delta H_{mix} = \sum_{i=1, i\neq j}^{n} \Omega_{ij} c_i c_j \quad (2)$$

where $\Omega_{ij} (= 4\Delta H_{AB}^{mix})$ is the regular solution interaction parameter between the ith and jth elements, ci or cj is the atomic percentage of the ith or jth component, and ΔH_{AB}^{mix} is the mixing enthalpy of binary liquid alloys, which can be obtained from Ref. [17].

Based on the Boltamenn's hypotheses, ΔS_{mix} is the mixing entropy of n-elements regular solution, which could be defined as:

$$\Delta S_{mix} = -R\sum_{i=1}^{n}(c_i \ln c_i) \quad (3)$$

where c_i is the molar percent of the ith element, $\sum_i^n c_i = 1$, and R is the gas constant (= 8.314JK^{-1}/mol). It is revealed that increasing temperature will reduce the Gibbs free energy and may stabilize the solid solution, especially at elevated temperatures.

1.2 Structures of HEAs

Alloy microstructures must be stable for elevated-temperature applications, because phase transformations occuring during use could deterirate properties and lead to failure. The high ΔS_{mix} stabilizes disordered solid solutions at elevated temperatures. On the other hand, phase-transformation kinetics decrease with temperature, and the formation of intermetallic phases may require long annealing times [18]. At the same time, suppressed kinetics may lead to the precipitation of exceptionally-fine, nanometer-sized particles and considerably improve properties of these alloys at ambient temperatures. Therefore, studying the phase and microstructure stability in HEAs is important for candidate high-temperature structural materials. Based on the concept of HEAs, multi-components tend to form the single-solid solution, including body-centered-cubic (bcc), face-centered-cubic (fcc), and hexagonal-closed-packed (hcp) crystal structure. It is proposed that the structure formation of the bcc or fcc phases could be determined by the component and valance electron concentration (VEC). Tong et al. [10] studied the crystal-structure evolution with the Al content changing in the typical $Al_xCoCrCuFeNi$ HEA. They found that with x

increasing from 0 to 3, the crystal structure tends to form the single fcc (with x = 0 - 0.5), fcc + bcc (with x = 1.0 - 2.0), then single bcc (with x = 2.3 – 3.0) phases. Guo et al. [14] proposed that the stability of fcc and bcc solid solutions is well delineated by the VEC. More specifically, fcc phases were found to be stable at higher VEC (≥ 8) and bcc phases, however, are stable at lower VEC (< 6.87). The relationship among the VEC, the FCC, and BCC stabilities was shown in Figure 1. 1.

1.3 Mechanical behaviors of HEAs

These new high-performance materials have excellent properties for the performance improvement of existing fossil-energy power-generation systems and advanced longer-term fossil-energy applications. HEAs possess high-temperature softening resistance [19] (resulting from a high-entropy effect), high ductility [5, 19, 20], great fatigue resistance [6], and excellent wear resistance [21]. Their properties are potentially useful for the harsh operating conditions of advanced boilers and steam turbines at 1,033 K/35 MPa and higher, and advanced gas turbines with inlet temperatures above 1,973 K.

Since high strength and ductility are important for structural materials, research efforts have been made to the applications with promising mechanical properties. Numerous equiatomic multi-component alloys have been reported in the literature, and some mechanical properties have been assessed with mixed results during past years. Even though HEAs tend to form single solid solutions, as mentioned above, many tested alloys contain multiple phases, including secondary solid-solution phases and/or intermetallic compounds. Two of the most studied compositions are Alx-Co-Cr-Fe-Ni and Co-Cr-Fe-

Mn-Ni systems. Yeh's group [1] studied very well on the Alx-Co-Cr-Fe-Ni system. As shown in Figure 1. 2, three compositions show the relationship between the yield strengths and temperatures. It is observed that the the low Al-content alloys exhibits low yield strength. However, it decreases slowly with increasing temperatures.

Otto et al. [22] investigated the influence of temperature and microstructure on the tensile properties of CoCrFeMnNi HEAs. As shown in Figure 1. 3, for two grain sizes, the alloy showed a strong increase in the yield strength and ultimate tensile strengths with decreasing temperature. Elongation to fracture also increased with decreasing temperature, expecially when temperature was down to the cryogenic environment, 77K. The other one is the new system, termed as refractory HEAs, proposed by Senkov [23], including refractory elements with high melting points, rather than the transition metals. It is well accepted that Ni-based superalloys have the great combination of elevated temperature properties, including creep resistance, corrosion resistance, and damage tolerance, but operating temperatures are reaching the theoretical limits of these materials. To meet the requirement of elevated-temperature applications, refractory HEAs were proposed and developed, as shown in Figure 1. 4. [4]. It illustrated the specific yield-strength change with increasing the temperature for TaNbHfTi, TaNbMoW, TaNbVMoW, and $CrCoCuFeNiAl_{0.5}$ cast alloys. It should be noticed that the high epecific yield strength of the $CrCoCuFeNiAl_{0.5}$ HEAs can be sustained over to 1,100K, and the TaNbMoW HEA can sustain its high specific strength to 1,800K. However, these refractory HEAs system possess high densities, and they are not applicable for the aerospace engineering. In order to solve this critical issue, the heavy elements of V, Ta, and W could be replaced by lighter

elements, such as Cr, Mo, and Zr in NbMoTaW and VNbMoTaW alloys. Thus, the the new modified refractory $NbCrMo_{0.5}Ta_{0.5}TiZr$ HEAs showed the improved yield strength and ductility with reduced densities of $8.2g/cm^3$, as shown in Figure 1. 5 [24, 25].

For a better understanding of the mechanical behaviors in HEAs, the comparison of specific strength, defined as yield strength over the density of materials, of HEAs with other conventional materials is presented in Figure 1. 6. [24]. It is interesting to see that the HEAs have densities close to the steel but rather high specific strength.

1.4 HEA applications

1.4.1 Fatigue applications

Besides the monotonic loading, the fatigue behavior and lifetime prediction during cyclic loading are one of the important applications. However, limited publications on the fatigue properties of HEAs were reported. Hemphill et al. and Tang et al. [6, 26] studied the fatigue behavior of the Al0.5CoCrCuFeNi HEA. From the comparison of the fatigue ratio of HEAs with other materials, such as steels, titanium alloys, and advanced BMGs (as shown in Figure 1. 7), it it shown that HEAs present the superior combination of mechanical properties of both yield strength and fatigue, suggesting that HEAs may be a good candidate for the fatigue applications. However, more work on the fatigue behavior need to be performed to have a deep understanding of deformation mechanisms of HEAs.

1.4.2 Corrosion applications

Since most studied HEAs contain passivating elements, such as Al, Cr, Mo, etc, which facilitate the formation of passive layers, similar to the case of stainless steels, it is expected to be resistant to corrosion. Furtehrmore, HEAs tend to be free of impurities or inclusions, which usually act as the corrosion-initiation site. Shi et al. [27] investigate the corrosion resistance in AlxCoCrFeNi HEAs, compared with conventional alloys. (as shown in Figure 1. 8). By comparing the E_p, resistance to pitting corrosion, and I_{corr}, the corrosion rate of Alx HEAs in the 3.5 weight percent (wt. %) NaCl solution with other conventional alloys, HEAs exhibit a higher pitting potentials and lower corrosion current densities than those of Al alloys, Cu alloys, and some Ti alloys. Based on the reported investigation on corrosion behavior, the comparison between conventional corrosion-resistant alloys and HEAs in the 3.5 wt. % NaCl solution is summurized in Figure 1. 9 [28]. It is observed that the corrosion current density of some HEAs tend to be much lower, suggesting a lower corrosion rate.

1.4.3 Bio-materials

The most important requirements for hte bio-materials are high specific strength, good corrosion resistance, good biocompatibility, and low elastic modulus. Todai et al. [29] invesitigate the biocompatibility of novel TiNbTaZrMo HEA with considerable strength. Figure 1. 10 shows the quatitative analysis of the cell density after 24 h cultivation on these materials. The annealed TiNbTaZrMo HEA exhibits superior biocompatibility, as compared to commercial pure Ti (CP-Ti). Wang et al. [30] study the potentiodynamic-polarization behavior in the phosphate buffer solution (PBS), as presented in Figure 1. 11.

As shown in Figure 1. 11, the TiZrNbTaMo HEA exhibits excellent corrosion resistance comparable to the Ti6Al4V alloy, and pitting resistance remarkably superior to the 316L SS and CoCrMo alloy. It is generally accpted that another important requirement for bio-materials is the low elastic modulus. Fazakas et al. [31] calculated the elastic modulus of TaNbHfZrTi, which are around 104 GPa, while the experimental researchs by Feuerbacher [32] and Dirras [33] present 79 GPa and 78.5 GPa, respectively, which is much lower than those of Ti-6Al-4V, the conventional orthopedic implants, indicating that TaNbHfZrTi may be the potential candidate for the application of orthopedic implants.

References

[1] J.-W. Yeh, S.-K. Chen, Su-Ji en Lin, J.-Y. Gan, T.-S. Chin, T.-T. Shun, C.-H. Tsau and S.-Y. Chang, "Nanostructured High-entropy Alloys with Multiple Principal Elements: Novel Alloy Design Concepts and Outcomes", Advanced Engineering Materials, 2004, 6(5), pp. 299-303.

[2] W.-H. Wu, C.-C. Yang, L. Yeh, Industrial development of high-entropy alloys. Annales De Chimie-Science Des Materiaux: Paris; New York: Masson, 1978-; 2006. p. 737.

[3] J.-W. Yeh, Recent progress in high-entropy alloys. Annales de Chimie Science des Matériaux. 2006;31:633-48.

[4] O. N. Senkov, J. M. Scott, F. Meisenkothen, S. V. Senkova, D. B. Miracle and C. F. Woodward, "Microstructure and elevated temperature properties of a refractory TaNbHfZrTi alloy", J Mater Sci, 2012, 47, pp. 4062-4074 Wang X, Zhang Y, Qiao Y, Chen G. Novel microstructure and properties of multicomponent CoCrCuFeNiTix alloys. Intermetallics. 2007;15:357-62.

[5] M. A. Hemphill, T. Yuan, G. Y. Wang, J. W. Yeh, C. W. Tsai, A. Chuang and P. K. Liaw, "Fatigue behavior of $Al_{0.5}$CoCrCuFeNi high entropy alloys", Acta Materialia, 2012, 60(16), pp. 5723-5734.

[6] Z. Liu, S. Guo, X. Liu, J. Ye, Y. Yang, X.-L. Wang, L. Yang, K. An and C. T. Liu, "Micromechanical characterization of casting-induced inhomogeneity in an Al0.8CoCrCuFeNi high-entropy alloy", Scripta Materialia, 2011, 64(9), pp. 868-871.

[7] O. N. Senkov, G. B. Wilks, J. M. Scott and D. B. Miracle, "Mechanical properties of Nb25Mo25Ta25W25 and V20Nb20Mo20Ta20W20 refractory high entropy alloys". Intermetallics. 2012;19:698-706

[8] C.-J. Tong, M.-R. Chen, S.-K. Chen, J.-W. Yeh, T.-T. Shun, S.-J. Lin and S.-Y. Chang, "Mechanical Performance of the AlxCoCrCuFeNi High-Entropy Alloy System with Multiprincipal Elements". Metall Mater Trans A. 2005;36A:1263-71.

[9] C.-J. Tong, Y.-L. Chen, S.-K. Chen, J.-W. Yeh, T.-T. Shun, C.-H. Tsau, S.-J. Lin and S.-Y. Chang,"Microstructure Characterization of AlxCoCrCuFeNi High-Entropy Alloy System with Multiprincipal Elements". Metall Mater Trans A. 2005;36A:881-93.

[10] K. Dahmen, Y. Ben-Zion and J. Uhl, "Micromechanical Model for Deformation in Solids with Universal Predictions for Stress-Strain Curves and Slip Avalanches". Physical Review Letters. 2009;102:175501-1--4.

[11] N. Friedman, A. T. Jennings, G. Tsekenis, J.-Y. Kim, M. Tao, J. T. Uhl, J. R. Greer and K. A. Dahmen, "Statistics of Dislocation Slip Avalanches in Nanosized Single Crystals Show Tuned Critical Behavior Predicted by a Simple Mean Field Model", Physical Review Letters. 2012;109.

[12] Y. Zhang, Y. J. Zhou, J. P. Lin, G. L. Chen and P. K. Liaw, "Solid-solution phase formation rules for multi-component alloys", Advanced Engineering Materials, 2007, 10, pp. 534-538.

[13] C. N. Sheng Guo, Jian Lu, and C. T. Liu, "Effect of valence electron concentration on stability of fcc or bcc phase in high entropy alloys". Journal of applied physics 2011;109:5.

[14] X. Yang and Y. Zhang, "Prediction of high-entropy stabilized solid-solution in multi-component alloys". Materials Chemistry and Physics. 2012;132:6.

[15] A. Takeuchi and A. Inoue, "Quantitative evaluation of critical cooling rate for metallic glasses". Materials Science and Engineering A. 2001;304-306:446-51.

[16] A. Takeuchi and A. Inoue, "Classification of bulk metallic glasses by atomic size difference, heat of mixing and period of constituent elements and its application to characterization of the main alloying element". Materials Transactions. 2006;46:13.

[17] C. Ng, S. Guo, J. Luan, S. Shi and C. T. Liu, "Entropy-driven phase stability and slow diffusion kinetics in an $Al_{0.5}$CoCrCuFeNi high entropy alloy". Intermetallics. 2012;31:165-72.

[18] W. H. Wu, C. C. Yang and J. W. Yeh, Annales De Chimie-Science Des Materiaux. 2006;31:737-47.

[19] S. Varalakshmi, M. Kamaraj and B. S. Murty, "Processing and properties of nanocrystalline CuNiCoZnAlTi high entropy alloys by mechanical alloying", Materials Science and Engineering A. 2010;527:1027-30.

[20] C. P. Lee, Y. Y. Chen, C. Y. Hsu, J. W. Yeh and H. C. Shih, "The Effect of Boron on the Corrosion Resistance of the High Entropy Alloys $Al_{0.5}CoCrCuFeNiB_x$", Journal of The Electrochemical Society, 2007, 154(8), pp. C424-C430.

[21] F. Otto, A. Dlouhý, C. Somsen, H. Bei, G. Eggeler and E. P. George, "The influences of temperature and microstructure on the tensile properties of a CoCrFeMnNi high-entropy alloy". Acta Materialia. 2013;61:5743-55.

[22] O. N. Senkov, G. B. Wilks, D. B. Miracle, C. P. Chuangd and P. K. Liaw, "Refractory high-entropy", Intermetallics. 2010;18:1758-65.

[23] Y. Zhang, T. T. Zuo, Z. Tang, M. C. Gao, K. A. Dahmen, P. K. Liaw and Z. P. Lu, "Microstructures and properties of high-entropy". Progress in Materials Science. 2014;61:93.

[24] O.N. Senkov and C. F. Woodward, "Microstructure and properties of a refractory $NbCrMo_{0.5}Ta_{0.5}TiZr$ alloy". materials science and Engineering A. 2011;529:311-20.

[25] Z. Tang, T. Yuan, C.-W. Tsai, J.-W. Yeh, C. D. Lundin and P. K. Liaw, "Fatigue behavior of a wrought Al0.5CoCrCuFeNi two-phase high-entropy alloy". Acta Materialia. 2015;99:247-58.

[26] Y. Shi, B. Yang, X. Xie, J. Brechtl, K. A. Dahmen and P. K. Liaw, "Corrosion of Al xCoCrFeNi high-entropy alloys: Al-content and potential scan-rate dependent pitting behavior", Corrosion Science, 2017, 119, pp. 33-45.

[27] Z. Tang, L. Huang, W. He and P. Liaw, "Alloying and Processing Effects on the Aqueous Corrosion Behavior of High-Entropy Alloys". Entropy. 2014;16:895-911.

[28] M. Todai, T. Nagase, T. Hori, A. Matsugaki, A. Sekita and T. Nakano, "Novel TiNbTaZrMo high-entropy alloys for metallic biomaterials", Scripta Materialia, 2017, 129, pp. 65-68.

[29] S.-P. Wang and J. Xu, "TiZrNbTaMo high-entropy alloy designed for orthopedic implants: As-cast microstructure and mechanical properties", Materials Science and Engineering: C, 2016, 73, pp. 80–89.

[30] É. Fazakas, V. Zadorozhnyy, L. K. Varga, A. Inoue, D. V. Louzguine-Luzgin, F. Tian and L. Vitos, "Experimental and theoretical study of Ti20Zr20Hf20Nb20X20 (X=V or Cr) refractory high-entropy alloys", International Journal of Refractory Metals and Hard Materials, 2014, 47, pp. 131-138.

[31] M. Feuerbacher, M. Heidelmann and C. Thomas, "Plastic deformation properties of Zr–Nb–Ti–Ta–Hf high-entropy alloys", Philosophical Magazine, 2015, 95(11), pp. 1221-1232.

[32] G. Dirras, L. Lilensten, P. Djemia, M. Laurent-Brocq, D. Tingaud, J. P. Couzinié, L. Perrière, T. Chauveau and I. Guillot, "Elastic and plastic properties of as-cast equimolar TiHfZrTaNb high-entropy alloy", Materials Science and Engineering: A, 2016, 654, pp. 30-38.

Appendix

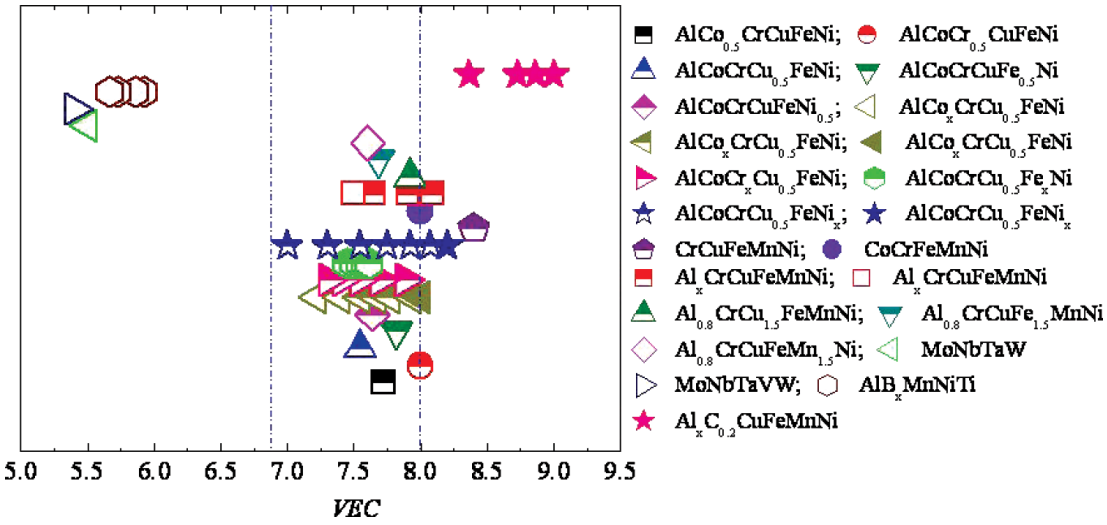

Figure 1. 1. Relationship among the VEC, the FCC, and BCC phases. Note on the legend: fully-closed symbols for sole fcc phases; fully-open symbols for the sole bcc phase; top-half closed symbols for mixed fcc and bcc phases.

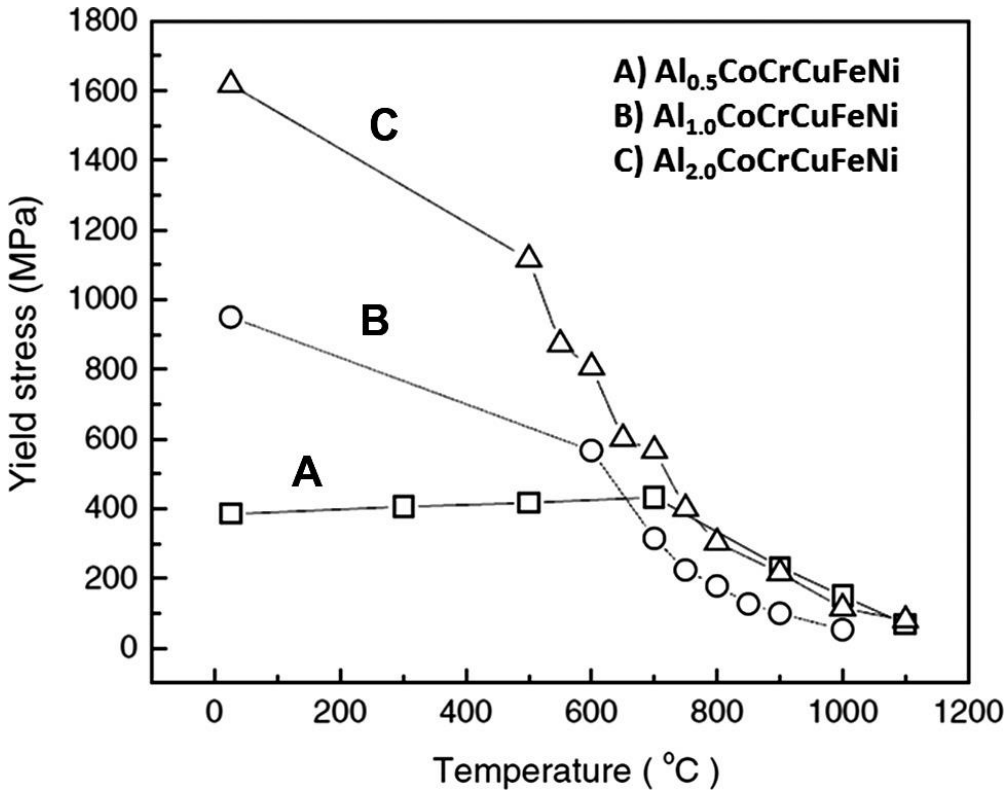

Figure 1. 2. Compressive yield strengths of $CuCoNiCrAl_xFe$ alloy system tested at different temperatures [1]

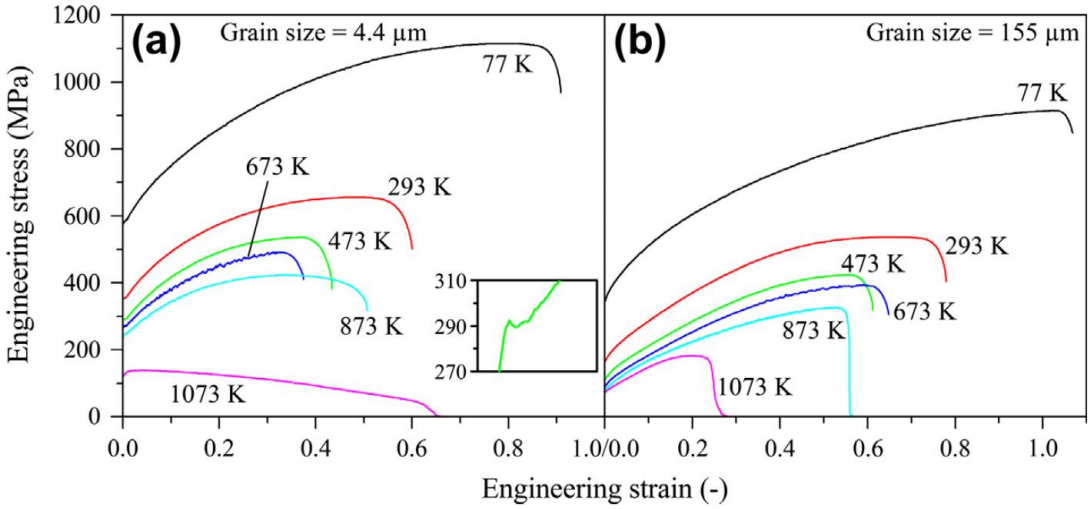

Figure 1. 3. Representative engineering stress–strain curves of the CoCrFeMnNi alloy at the six testing temperatures for the (a) fine-grained (grain size of 4.4 µm) and (b) coarse grained (grain size of 155 µm) materials. The inset in (a) shows a small load drop after yielding for a fine-grained sample that was tested at 473 K [22]

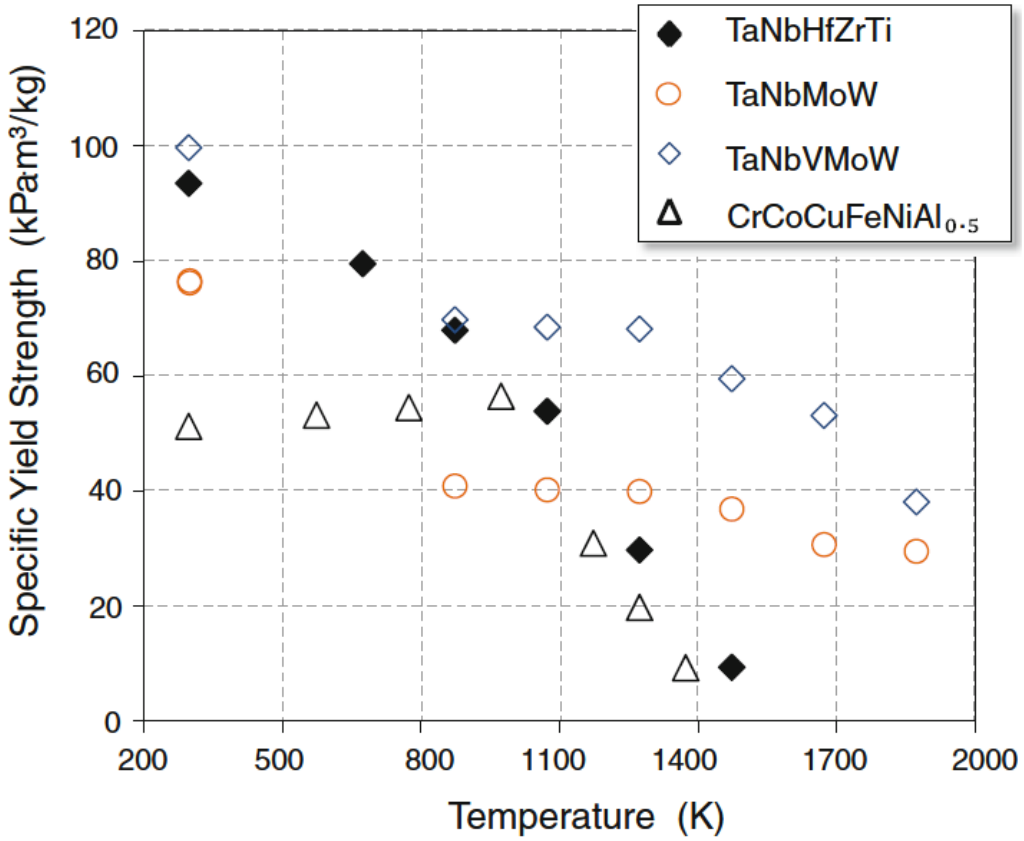

Figure 1. 4. The temperature dependence of the specific yield strength of the TaNbHfZrTi alloy in comparison with that for TaNbMoW [16], TaNbVMoW [16], and $CrCoCuFeNiAl_{0.5}$ [4] cast alloys

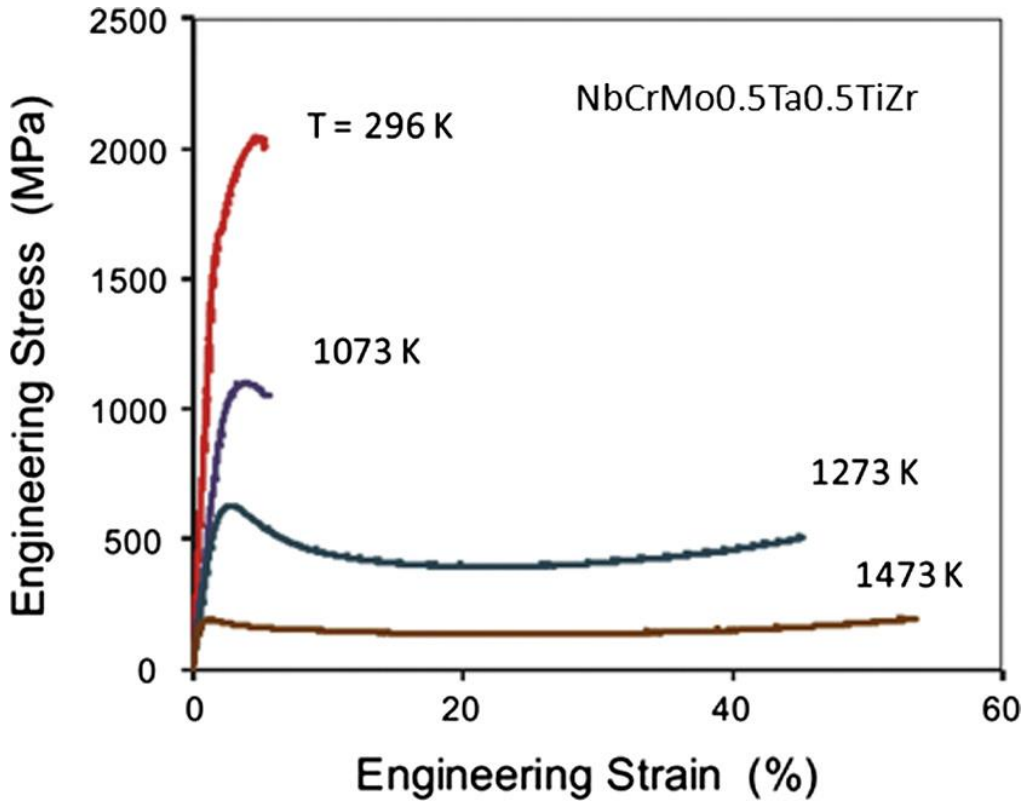

Figure 1. 5. The engineering stress vs. engineering strain compression curves of HIPd $NbCrMo_{0.5}Ta_{0.5}TiZr$ alloy samples at 296 K, 1,073 K, 1,273 K, and 1,473 K.

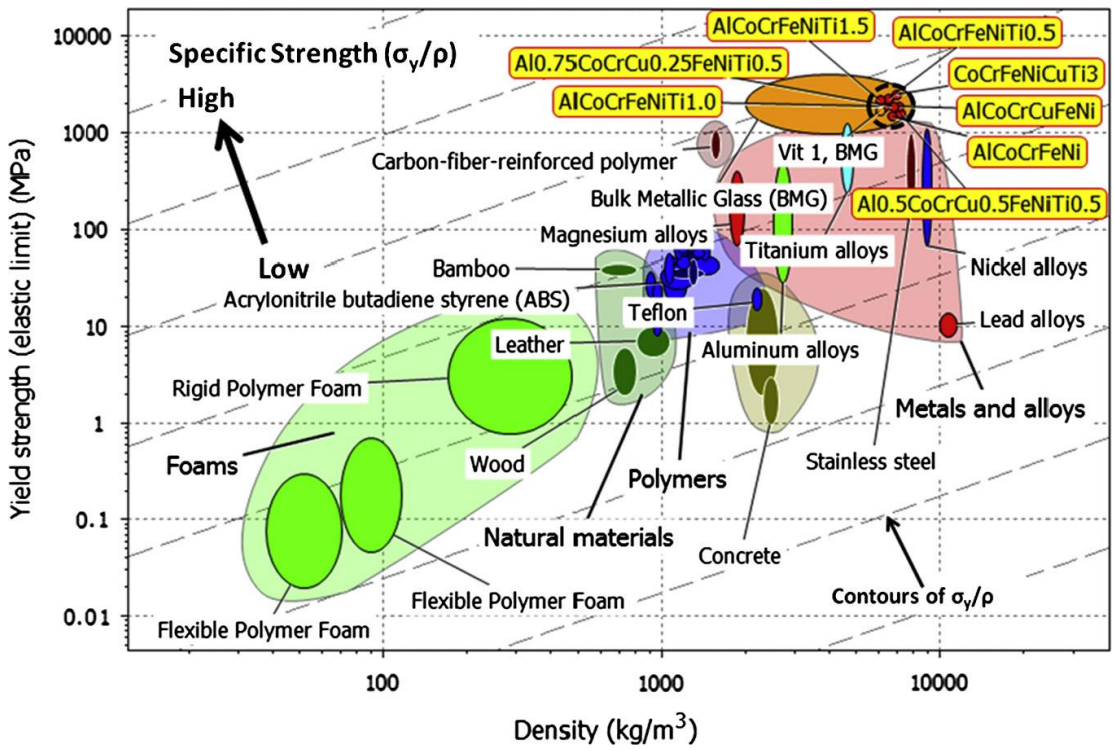

Figure 1. 6. An Ashby map showing yield strength (σ_y) versus Young's modulus (E) ranges at room temperature for foams, natural materials, elastomers, ceramics, polymers, composites, and metals, along with data for BMGs and some HEAs. The contours show the material indices or guide lines for the resilience, σ_y 2/E [24].

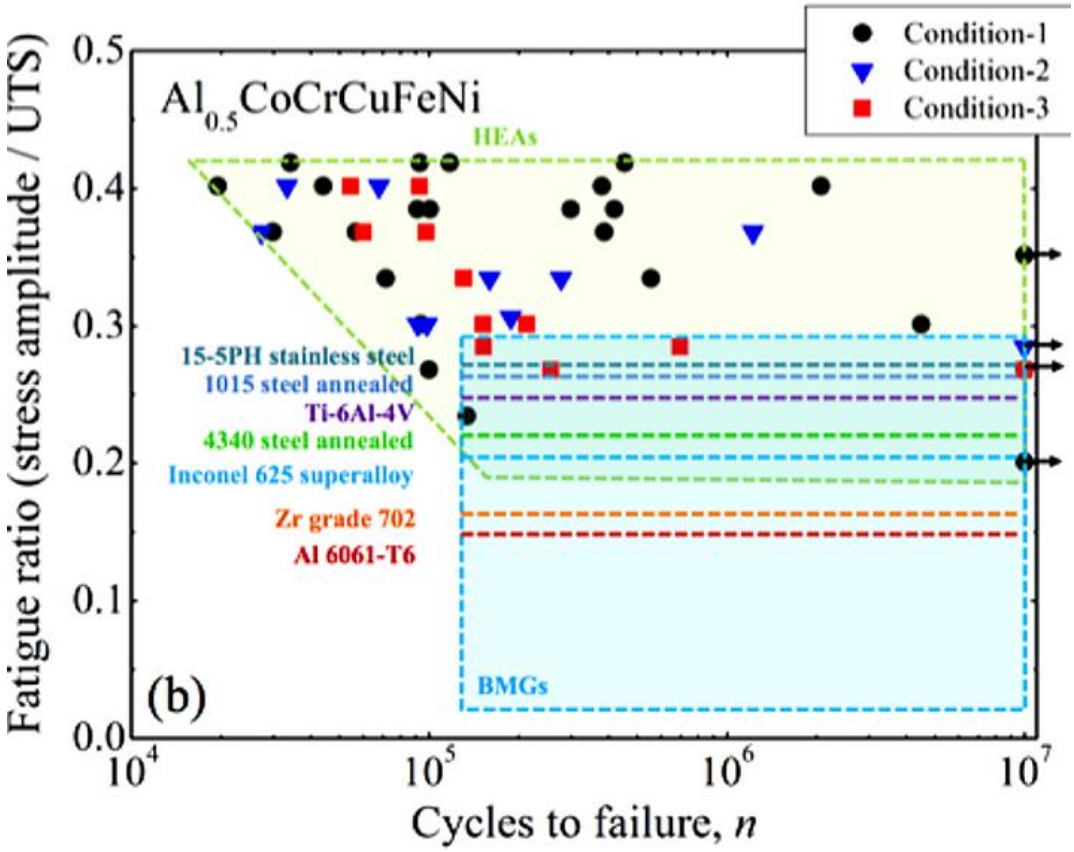

Figure 1. 7. S–N curves comparing the fatigue ratios of the $Al_{0.5}CoCrCuFeNi$ HEA, other conventional alloys, and BMGs. Colored dashed lines denote the endurance limit of each alloy [6, 26]

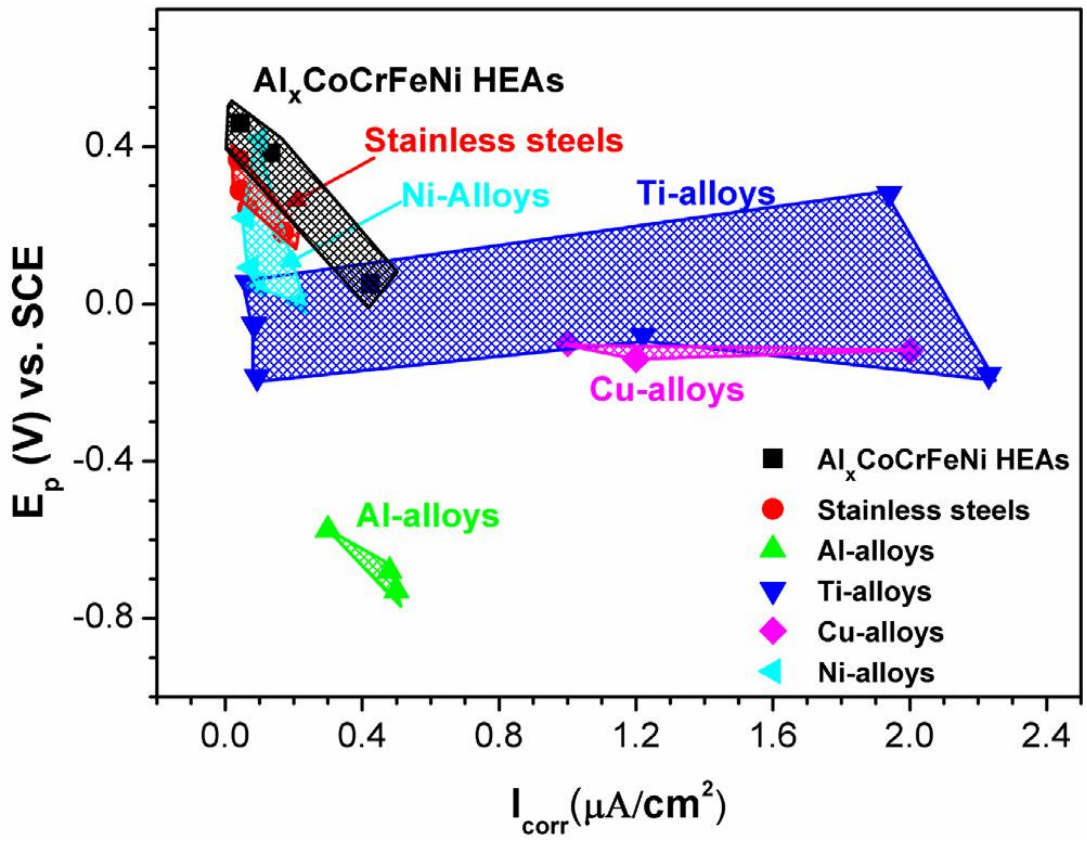

Figure 1. 8. Comparison of E_p and I_{corr} between $Al_xCoCrFeNi$ (x = 0.3, 0.5, and 0.7) HEAs and other conventional alloys in the 3.5 wt.% NaCl solution at room temperature [27]

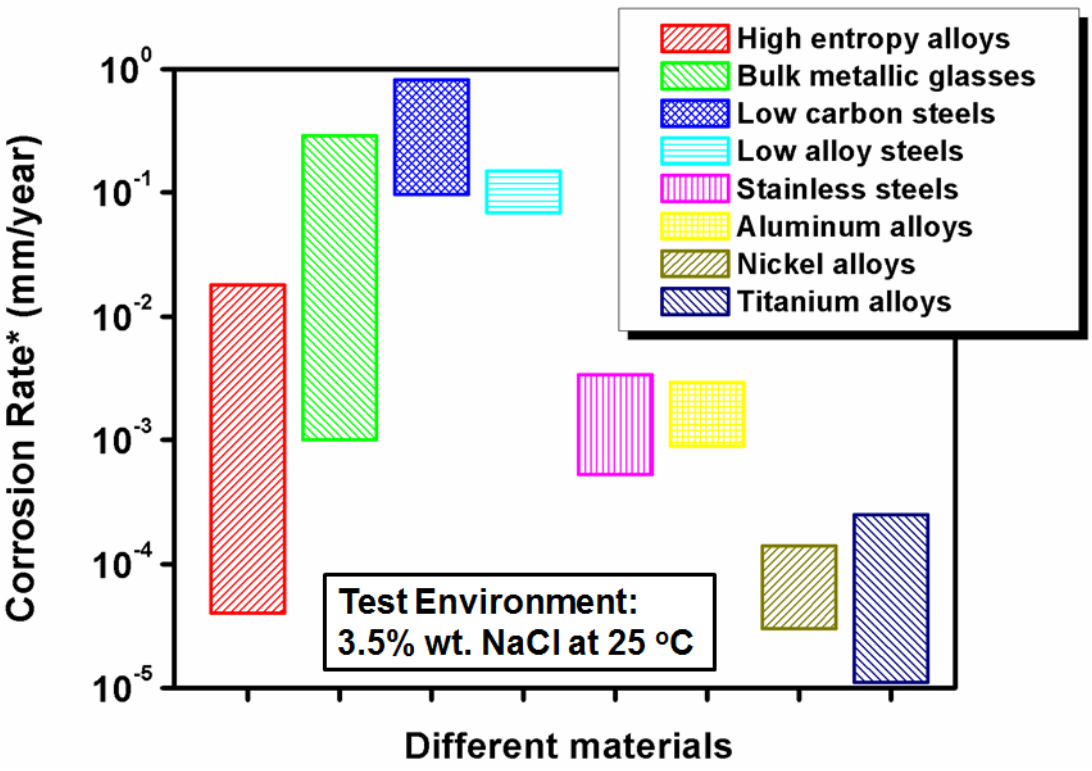

Figure 1. 9. A comparison to average corrosion rates (mm/year) between HEAs and conventional alloys in the 0.5 M H_2SO_4 solution at room temperature [28]

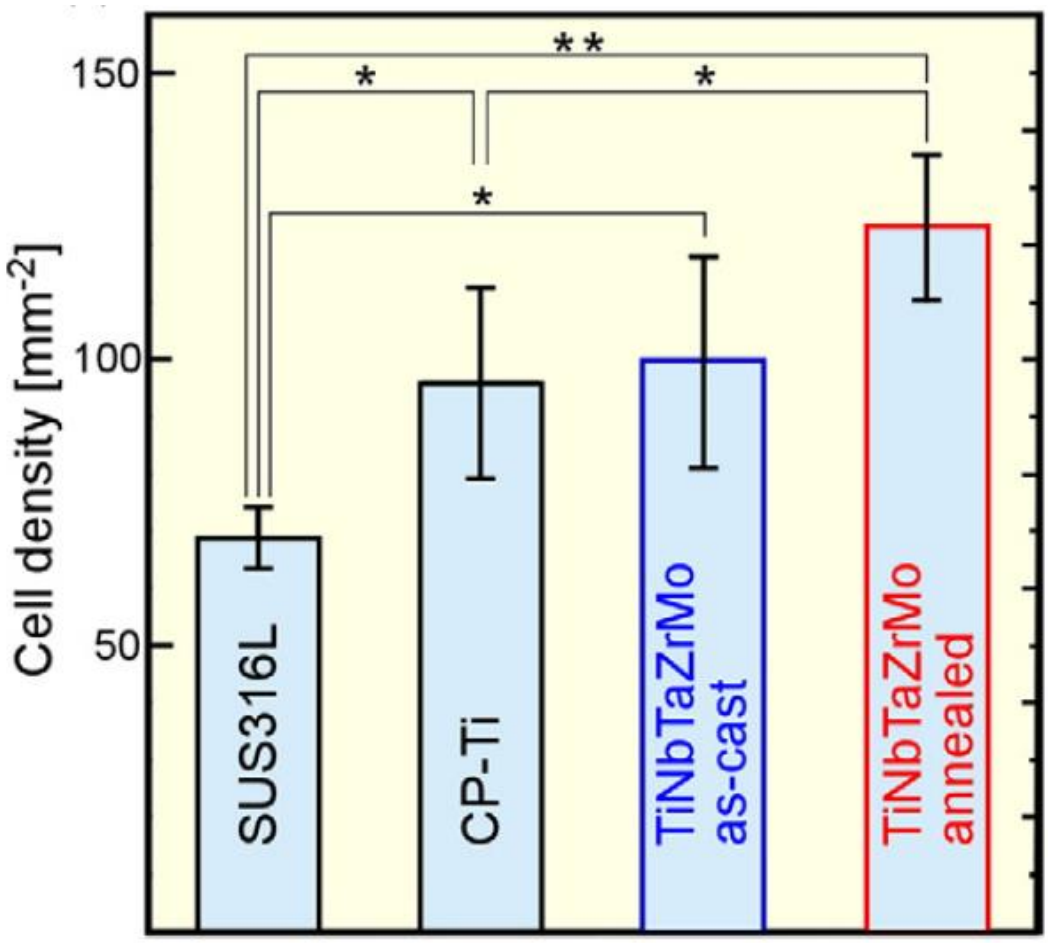

Figure 1. 10. Giemsa staining of the osteoblasts cultured quantitative analysis of cell density after 24 h cultivation on each alloy [29]

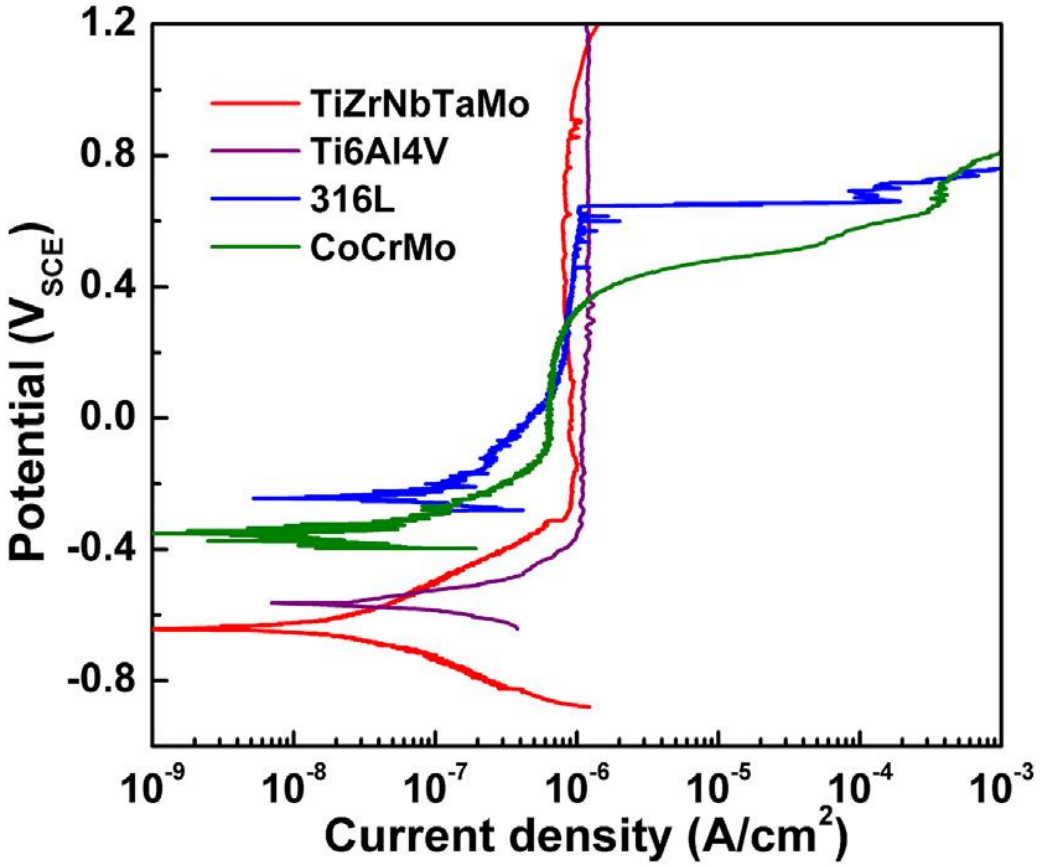

Figure 1. 11. Potentiodynamic polarization curves of the arc-melted TiZrNbTaMo HEA, as well as Ti6Al4V, 316L SS, and Co28Cr6Mo alloys in PBS at 37 °C for comparison. [30]

CHAPTER II GRAIN GROWTH AND HALL-PETCH RELATIONSHIP IN A REFRACTORY HFNBTAZRTI HIGH-ENTROPY ALLOY

A version of this chapter was originally submitted by Shuying Chen, Yang, Tong, Weidong Li, Ko-Kai. Tseng, Che-Wei Tsai, Jien-Wei Yeh, and Peter K. Liaw in 2019:

Authors:

S. Y. Chen, Yang Tong, W. D. Li, and Peter K Liaw

Department of Materials Science and Engineering, The University of Tennessee, Knoxville, TN 37996, USA

K. - K. Tseng, Che-Wei Tsai, J.- W. Yeh

Department of Materials Science and Engineering, National Tsing Hua University, Hsinchu, 30013, Taiwan

High Entropy Materials Center, Department of Materials Science and Engineering, National Tsing Hua University, Hsinchu 30013, Taiwan

S. Chen's involvement in the article: design experimental procedures, prepared the samples, performed the heat treatment and microstructural characterization, analyzed the experimental data, wrote and revised the article.

Co-researcher's contributions are listed as follow:

Y. Tong and W. Li helped Shuying with the designation and the discussion of data and revised the article.

K. Tseng and C Tsai helped Shuying with the fabrication of samples.

J.-W. Yeh and P.K. Liaw provided research guidelines and helped with the data analysis and paper revision.

Abstract

Understanding the effect of temperature variation on the microstructural evolution is particularly important to refractory high-entropy alloys (RHEAs), given their potential high-temperature applications. Here, we experimentally investigated the grain-growth behavior of the HfNbTaZrTi RHEAs during recrystallization at temperatures from 1,000 to 1,200 ^{o}C for varied durations, following cold rolling with a 70% thickness reduction. Following the classical grain-growth kinetics analysis, grain growth exponent and activation energy of the alloy were determined to be 2.2-2.4 and 303 kJ/mol, respectively. Moreover, the yield strength – grain size relation was found to be well described by the Hall-Petch relation in the form of $\sigma_y = 942 + 270D^{-0.5}$, where σ_y is the yield strength and D is the grain size. It was revealed that the friction stress, 942 MPa, in the HfNbTaZrTi HEA is higher than that of tungsten alloys, which indicates the high intrinsic stress in the BCC-RHEA. The coefficient, 270 MPa/μm $^{-1/2}$, is much lower than that in the 316 stainless steel and $Al_{0.3}$CoCrFeNi HEAs, which indicates low grain-boundary strengthening.

2.1 Introduction

High-entropy alloys (HEAs) were coined by Yeh [1] in 2000's, and have attracted the rapidly-increasing attention in the past decade due to their stabilized microstructures and remarkable mechanical properties [2,3]. HEAs typically consist of five or more metallic elements in equal or nearly-equal atomic percent and are inclined to form solid solution phases including body-center-cubic (BCC) [3-5], face-center-cubic (FCC) [6-9], and hexagonal-close-packed (HCP) structure [10-13] by the stabilization of the high configurational entropy [7,14]. Prior research has demonstrated that HEAs possess superior properties in many facets, including high yield strength [14], good microstructural stability, retained mechanical strength at elevated temperatures [15, 16], and excellent resistance to wear [17], corrosion [18, 19], creep [20, 21], fracture [22], and fatigue [23-30].

Studying the grain-growth behavior of HEAs is important, as the improper thermal exposure may significantly degrade an alloy's mechanical properties, e.g., fatigue-strength drop. But sluggish diffusion, considered as one of the core effects for HEAs, can stabilize grains by slowing down their growth. Liu et al. [31] investigated the grain growth in the CoCrFeMnNi HEAs in a temperature range of 850 ^{o}C to 950 ^{o}C and determined the activation energy for growth to be 321.7 kJ/mol. Wu et al. [32] reported a grain-growth exponent of 4 in the CoCrFeNi HEA at 900 ^{o}C. Dan Sathiaraj [33] found that the sluggish diffusion in the CoCrFeMnNi HEAs can significantly influence the texture development during the grain growth. However, it remains unclear whether this phenomenon is general to RHEAs.

Painting a clear picture about the grain growth and its effect on mechanical properties in RHEAs is even more important than doing so in non-refractory HEAs, simply because RHEAs are primarily targeted for high-temperature applications and are expected to expose to elevated temperatures for long durations. The HfNbTaZrTi RHEA is becoming of great interest recently because it manifests excellent softening resistance at elevated temperatures, making it very promising for high-temperature applications [15]. Also, this BCC HfNbTaZrTi RHEA has outstanding phase stability at temperatures greater than 1,000 °C [15] and excellent malleability at low temperatures. Senkov et al. [34] first conducted a preliminary investigation on the grain growth in this RHEA upon cold rolling and annealing. Juan et al. [35] performed a detailed study on the cold-rolled (70% thickness reduction) as-cast HfNbTaZrTi RHEA in a temperature range of 1,200 – 1,350 °C, and reported the grain-growth exponent and activation energy to be 3.5 and 389 kJ/mol, respectively. The later work by Senkov et al. [36] examined the grain-growth kinetics in a homogenized, cold-forged, and then cold-rolled (89% thickness reduction) HfNbTaZrTi RHEA at 800 – 1,200 °C, and suggested a grain-growth exponent of 2 and activation energy of 246 kJ/mol. However, opposite conclusions can be drawn based on the considerably different values from these two studies. The major difference between these two cases is the sample processing. In an as-cast HfNbTaZrTi RHEA, compositional heterogeneity exists in dendrite and inter-dendrite regions [34], which can impose a significant influence on the grain growth due to the solute-dragging effect. On the other hand, the cold-forging treatment [36] can highly induce dynamic recovery and dynamic recrystallization, which should not be ignored when comparing these two studies.

To reduce the extrinsic effects mentioned above, the present work examined the grain-growth behavior during annealing at lower temperature range, 1,000, 1,100 and 1,200 °C, on the cold-rolled as-cast HfNbTaZrTi RHEA. The intent is to offer a complementary viewpoint on the grain-growth kinetics in the HfNbTaZrTi RHEA. Meanwhile, the effect of grain size on its mechanical properties was also studied.

2.2 Material and experimental procedures

The HfNbTaTiZr RHEA ingots were prepared by arc melting the constituent elements [purity > 99.9 weight percent (wt.%)] in a water-cooled copper crucible under the argon atmosphere. To ensure the compositional homogeneity, the melts were overturned and re-melted for multiple times prior to dropping to copper molds for solidification. After finishing the round slugs from the bowl-shape copper mold, several slugs were re-melted again in the rectangular mold with the cavity dimensions 20 × 30 × 60 mm. The slab ingots were machined into the dimensions of 13.5 × 25× 50 mm for the subsequent cold-rolling process. There is no homogenization treatment prior to rolling. Individual reduction per pass was 0.2 mm. Specimens were cold-rolled to a final thickness of 4 mm (a thickness reduction of 70%). The cold-rolled sheets were then sealed in vacuum-quartz tubes and annealed at 1,000, 1,100, and 1,200 °C for 0.5, 2, 6, and 24 hours, followed by water quenching. All heat-treated samples were ground and polished on a Buehler rotating grinder and polisher to remove surface defects, with the 400, 600, 800, and 1,200 grit sandpapers used in sequence. Then samples were placed on the vibratory polisher for 24 hours, with polishing suspension of colloidal silica of 0.05μm to obtained the final polished specimens with mirror surface. No etching was performed. The average grain sizes of

differently-processed alloys were determined by applying the linear intercept method to microscopic images taken from the scanning electron microscope (SEM, Zeiss, EVO MA15).

The phases that are present in differently-treated alloys were identified through X-ray diffraction (XRD, Panalytical Empyrean) with the Cu Kα radiation. The detailed parameters are: slit: soller slits 0.04 rad; mask: fixed incident beam mask 10 mm; step size: 0.013; speed:0.05□/s, respectively. The detailed microstructures in these alloys were examined with the SEM equipped with back-scattered diffraction. The acceleration voltage and filament current are 20 kV and 1 nA, respectively. The flat dog-bone-shaped tensile specimens are machined with a gauge length of 19 mm, thickness of 1 mm, and gauge section width of 3 mm. Tensile tests were carried out on selected RHEA samples with different grain sizes at room temperature and a strain rate of 1×10^{-4}/s.

2.3 Results

2.3.1 Phase and microstructure

After undergoing the cold-rolling reduction with a 70% thickness reduction and annealing at 1,000, 1,100, and 1,200 ℃ for 0.5, 2, 6, and 24 hours, the HfNbTaZrTi HEAs exhibits single BCC phase. Some representative XRD patterns samples annealed at 1,000 – 1,200 ^{o}C for 0.5 hours are shown in Figure 2. 1 (All tables and figures are located in the appendix). No second phases except single BCC phase form at this temperature range. During the annealing treatment, the elongated grains originated from cold rolling are consumed and turned into equiaxed grains after experiencing nucleation and growth stages.

The recrystallized grains of the samples after being annealed at 1,000 – 1,200 ºC for 0.5 and 24 hours were characterized with backscattered-electron (BSE) imaging, as given in Figure 2. 2. One microstructural feature worth emphasizing is that the equiaxed grains attained in the alloys are not uniform in size for all annealing conditions, as evidenced by the mixture of coarse and fine grains on the images of microstructures. Size variation in the recrystallized grains may be related with the varied energy storage in grains during the cold-rolling process, which is the driving force of recrystallization and grain growth [34].

2.3.2 Grain-growth kinetics phase and microstructure

Grain growth of the HfNbTaZrTi RHEA upon annealing was further quantitatively analyzed in this section. We first plot the average grain size as a function of the annealing temperature at the annealing time of 0.5 – 24 hours in Figure 2. 3. The grain size increases with the increase of both the annealing temperature and time. For a given annealing time, the variation of the grain size with the temperature approximately follows a linear trend. The rate of grain growth is slow at 1,000 °C, but gradually becomes faster when the temperature ramps up to 1,100 and 1,200 °C. The average grain sizes measured for the HfNbTaZrTi HEAs under various annealing conditions in the present work are listed in Table 2. 1. Alongside we also compile from the literature the grain sizes of the same HEA that have experienced similar heat treatments [34, 36]. Comparing the results in Table 2. 1, we found that the grain size drops, as the thickness reduction increases during cold rolling. For instance, when annealed at 1,000 ºC for 2 hours, the average grain sizes are 35, 31.5, 22, and 21.9 μm for the alloy with a thickness reduction of 65% [34], 70%, 84.6% [34], and 89% [36], respectively. The declining trend of the grain size with increasing the

thickness reduction during cold rolling is most likely associated with the variation in the available grain-nucleation sites in differently-deformed alloys. In heavily-deformed materials, a fairly-large amount of defects, including dislocation structures, grain boundaries, and other deformation heterogeneities, such as deformation bands [33], are potential sites for new grains to nucleate. As a consequence, compared to the counterparts with less deformation, more grains participate in competition among the course of recrystallization, resulting in a slower grain growth rate [33, 37].

The grain-growth kinetics in metals can be quantified by a parabolic model proposed by Burke and Turnbull [38]. The model was constructed, based on the hypothesis that recrystallized grains grow by grain-boundary migration. For the sake of the minimization of the grain-boundary area and the associated energy, the rate of boundary migration is thought of being inversely proportional to the radius of the curvature of grain boundaries, further to the diameter of grains [39]. Eventually, the evolution of the grain size over time is expressed as [40, 41]

$$D^n - D_0^n = kt, \quad (1)$$

where t is the time, D_0 is the initial grain size (at $t = 0$), D is the grain size at the time, t, for a given temperature, n is the grain-growth exponent, and k is a constant depending on the material composition and temperature. In the work previously reported, D_0 is usually ignored by assuming $D >> D_0$ [31]. This approximate treatment will undoubtedly cause errors when determining the value of n, and later the activation energy, posing questions on the credibility of the conclusions derived thereafter. To avoid any uncertainty caused by

approximation, here we use a differential method to treat D_0 explicitly. Specifically, we first take differentiation to both sides of Eq. (1) with respect to *t*, getting

$$\frac{dD^n}{dt} - \frac{dD_0^n}{dt} = k \cdot \frac{dt}{dt}. \tag{2}$$

Since D_0 is a constant, we have $\frac{dD_0^n}{dt} = 0$, Eq. (2) reduces to

$$\frac{dD^n}{dt} = k. \tag{3}$$

Given that *D* is a function of time *t*, i.e., $D = f(t)$, Eq. (3) can be further written as

$$\frac{dD^n}{dD} \cdot \frac{dD}{dt} = k, \tag{4}$$

and then

$$n \cdot D^{(n-1)} \cdot \frac{dD}{dt} = k. \tag{5}$$

Taking natural logarithm (or common logarithm) to both sides of Eq. (5), we have the following

$$\ln(n \cdot D^{(n-1)} \cdot \frac{dD}{dt}) = \ln k, \tag{6}$$

$$\ln n + \ln D^{(n-1)} + \ln \frac{dD}{dt} = \ln k, \tag{7}$$

$$\ln n + (n-1)\ln D + \ln \frac{dD}{dt} = \ln k. \tag{8}$$

Rearranging Eq. (8), we arrive

$$\ln \frac{dD}{dt} = -(n-1)\ln D + \ln k - \ln n \tag{9}$$

$$\ln \frac{dD}{dt} = -(n-1)\ln D + \ln \frac{k}{n} \tag{10}$$

Now we can use Eq. (10) to fit the experimental data.

The slope of the fitting curve is -(*n*-1), the intercept is $\ln\frac{k}{n}$. Knowing *n* and $\ln\frac{k}{n}$, *k* is determined from

$$k = n \cdot e^{intercept} \tag{11}$$

The grain-growth data at different temperatures is plotted in the form of ln(*dD*/*dt*) against ln*D* and linearly fitted in Figure 2. 4. From the slopes and intercepts of the linear fits, the *n* and *k* values for the HfNbTaZrTi HEAs annealed at 1,000, 1,100, and 1,200 °C are determined and listed in Table 2. 2.

From an atomic perspective, the grain growth is a diffusion process in which atoms diffuse across the grain boundary by thermal activation. The thermal-activation nature of the grain-growth law described in Eq. (1) is embedded in the constant, *k*, which is an Arrhenius-type equation written as [42]

$$k = k_0 \exp\left(-\frac{Q_g}{RT}\right), \tag{12}$$

where k_0 is a constant taking into account the activation energy of grain boundaries, Q_g is the activation energy, *T* is the temperature, and *R* is the gas constant. Taking logarithm to both sides of Eq. (12) reaches

$$\ln k - \ln k_0 = \left(-\frac{Q_g}{RT}\right), \tag{13}$$

with which we can perform a linear fit to the $\ln k$ against $1/T$ data to obtain the activation energy, Q_g, from the slope. As demonstrated in Figure 2. 5, Q_g is determined to be 303 kJ/mol for the HfNbTaZrTi RHEA in study.

2.3.3 Effect of grain size on mechanical properties

Annealing the RHEA samples at 1,000, 1,100, and 1,200 °C for 6 hours produces an average grain sizes of 40, 87, and 112 μm, respectively. The engineering stress – strain curves of these coarse- and fine-grained specimens measured from uniaxial tension are provided in Figure 2. 6, from which it is evident that the flow stress of the HEAs increases as the grain size decreases. Some key material properties, such as the yield strength taken at a plastic strain of 0.2%, ultimate tensile strength (UTS), and elongation, are extracted from the curves and listed in Table 2. 3 The HEA with the smallest grain size of 40 μm exhibits the highest yield strength of 985 MPa, followed by 972 MPa for the specimen with a grain size of 87 μm, and then 967 MPa for the specimen with a grain size of 112 μm. The same trend holds for the ultimate tensile strength (UTS) as well, as indicated in Figure 2. 6 and Table 2. 3. It is noted that the work hardening of the present RHEA during tension is quite low, which results in small increase in strength up to UTS. The reason for this is attributable to its distorted whole-solute BCC matrix with high-strength and large lattice distortion which could potentially raise the driving force to reduce overall strain energy and induce dynamic recovery [35]. Actually, the calculated lattice distortion in our treated HEAs is much higher than the reported ones [58].

The effectiveness of the grain refinement in enhancing the strength of polycrystalline metals is known to be ascribed to the grain-boundary hardening, and can be quantified by the well-known Hall-Petch relation [43-45]

$$\sigma_y = \sigma_0 + k_{HP} D^{-0.5}, \tag{14}$$

where σ_y is the yield strength, D is the average grain size, σ_0 is a constant that can be considered as either the frictional stress induced by dislocation motions or internal back stresses [45], k_{HP} is a constant that can be viewed as a measure of the grain-boundary resistance to slip transfer [45].

We apply this classical equation to our RHEA by plotting the experimental yield strength as a function of $D^{-0.5}$ in Figure 2. 7 and fitting the data with Eq. (14). From the fitting curve, σ_0 and k_{HP} can be retrieved as 942 MPa and 270 MPa/μm$^{-1/2}$ from the intercept and slope, respectively. Ultimately, the Hall-Petch relation for the present HfNbTaZrTi HEA has the form of $\sigma_y = 942 + 270D^{-0.5}$. The k_{HP} obtained for the HfNbTaTiZr RHEA in the present work, 270 MPa/μm$^{-1/2}$, is comparable with the value of 246 MPa/μm$^{-1/2}$ reported in Juan et al.'s work [35]. For a better comparison of the friction stress σ_0 and k_{HP} in various alloys, the data for other alloys is retrieved from the literature and plotted in Figure 2. 8 along with ours. It is apparent that the RHEA in the present work exhibits a much higher friction stress than that of the AISI 301 stainless steel, Mo, Nb and W alloys [46], and CoCrFeMnNi HEAs, etc. However, the k_{HP} value in the current HfNbTaTiZr RHEA is found to be much lower than that in the 316 stainless steel, CoCrFeMnNi, and $Al_{0.3}$CoCrFeNi HEAs. This is interesting and reasonable by consideration of the low work hardening in the present RHEA. In fact, grain size strengthening is preferentially explained by the pre-working hardening along grain boundaries before macroyielding, which has been verified by TEM observation of deformation zone along grain boundaries [47]. Before macro-yielding, the preferential yielding and plastic deformation along grain boundaries

induced by elastic incompatibility among neighboring grains in the elastic region explains the grain size strengthening effect [47].

2.4 Discussion

A typical value of $n = 2$ is usually noted for pure metals, in which diffusion governs the grain-growth kinetics. n values larger than 2, however, are often found in solid-solution alloys because of solute dragging effect at grain boundaries. In light of this assertion, Juan et al. [35] found a large value of $n = 3.5$ in the cold-rolled and annealed HfNbTaZrTi RHEA. They proposed that the solute-drag effect is significant in the whole-solute matrix of HEAs as compared with conventional solid solution alloy. This relates to the energy reason that the different sizes of abundant solutes along grain boundaries would in-situ adjust their relative positions to form the low-energy configuration of grain boundaries during boundary migration. In the cold-rolled and annealed HfNbTaZrTi RHEA studied in the present work, $n = 2.2 – 2.4$ is slightly larger than the typical value of 2 for pure metals, suggesting that chemical segregation and solute drag also plays a major role in slowing down grain growth [41]. It is noted that the main difference in the processing is the annealing temperature range: Juan's work used the annealing temperature from 1,200 to 1,350 °C whereas the present work used that from 1,000 to 1,200 °C. As the degree of short range chemical order due to bonding difference among atomic pairs is higher at lower temperature range and lower at higher one, it suggests that retardation to grain boundary migration is smaller with lower degree of short range ordering at higher temperatures. This means more random distribution of solute atoms yields a larger drag force to grain boundary. The phenomenon can be explained because the tendency to get low-energy

configuration of grain boundaries during boundary migration by in-situ adjustment of the abundant solutes along grain boundaries would be more significant than that with abundant short range order clusters which already in lower energy state [52, 56, 57, 60, 61]. This explanation relates with the abundant solute in the random solid solution state, so the mechanism is not found in conventional alloys based on one major element and low concentration of solute atoms. This means the phenomenon and its mechanism is new for the whole-solute matrix. As the grain boundaries are high diffusion path, the in-situ pinning along whole boundary continues even as grain boundary migrates. On the other hand, short range ordering gives a cluster distribution, preferential Nb,Ta-rich, and Hf,Ti,Zr-rich clusters due to chemical compatibility, dispersed in the grain interiors consume most solute atoms in the rest matrix and reduce the in-situ pinning force on grain boundaries. As clusters of short range are nanoscale in size, they do not behave like large precipitates or inclusions to give Zener pinning and have limited contribution to the drag force, as grain boundaries sweep across the cluster dispersion in the path.

On the other hand, Senkov's work gave n = 3 for the same temperature range from 1,100 to 1,200 °C indicating higher drag force to grain boundary migration [36]. This could be explained with the fact that Senkov's sample received a homogenization treatment at 1,200 °C for 24 hours, by which dendrite and interdendrite segregations were mostly eliminated to give more random distribution of solutes as compared with that of the present work.

Since the grain growth is a diffusion process in nature, the activation energy also plays a crucial role. Equation (10) essentially links the activation energy with the constant, *k*, in the governing equation of grain growth. In the present study, the activation energy for the HfNbTaTiZr RHEA is determined as Q_g = 303 kJ/mol. As stated above, the higher activation energy from 1,200 to 1,350 °C relates with higher degree of disorder, i.e., more random state. The mechanism explaining for n = 3.5 and high activation energy 389 kJ/mol is directly related to the volume diffusion through the lattice, whose rate is controlled by the slowest species, i.e. Nb and Ta. Migration of grain boundaries cannot proceed without increasing energy except the average composition is maintained, which could be controlled by the slow ones that determines the reaction rate [35]. On the other hand, the smaller activation energy from 1,000 to 1,200 °C relates with higher degree of short range order, preferential Nb,Ta-rich, and Hf,Ti,Zr-rich clusters due to chemical compatibility [52,56, 57, 60, 61]. The cluster distribution in the matrix would have less problem in waiting for the slow ones in keeping the homogenous equiatomic composition. Thus, the activation energy is no longer determined by Nb and Ta and has a lower value.

2.5 Conclusions

The grain growth of the cast HfNbTaTiZr HEA, subsequent to cold-rolling and annealing at 1,000 – 1,200 ℃ for up to 24 hours, was investigated. Experimental results determine the grain-growth exponent and average activation energy to be *n* = 2.2 – 2.4 and Q_g = 303 kJ/mol, respectively. The higher activation energy relates with higher degree of disorder, i.e., more random state. Grain boundary migration needs the volume diffusion

through the chemically-homogeneous lattice, whose rate is controlled by the slowest species, Nb and Ta. The grain-size strengthening follows the Hall-Petch relation in the form of $\sigma_y = 942 + 270D^{-0.5}$. The low k_{HP} coefficient, 270, is consistent with the low work hardening of the present RHEA since work hardening along grain boundaries could enhance macro-yield strength.

References

[1] J. W. Yeh, S. K. Chen, S. J. Lin, J. Y. Gan, T. S. Chin, T. T. Shun, C. H. Tsau, and S. Y. Chang, "Nanostructured high-entropy alloys with multiple principal elements: novel alloy design concepts and outcomes", Advanced Engineering Materials, 2004, 6(5), pp. 299-303.

[2] B. Cantor, I. T. H. Chang, P. Knight, and A. J. B. Vincent, "Microstructural development in equiatomic multicomponent alloys", Materials Science and Engineering A, 2004, 375-377, pp. 213-218.

[3] O. N. Senkov, G. B. Wilks, D. B. Miracle, C. P. Chuang, and P. K. Liaw, "Refractory high-entropy ", Intermetallics, 2010, 18, pp. 1758-1765.

[4] O. N. Senkov, J. M. Scott, S. V. Senkova, D. B. Miracle, and C. F. Woodward, "Microstructure and room temperature properties of a high-entropy TaNbHfZrTi alloy", Journal of Alloys and Compounds 2011, 509, pp. 6043-6048.

[5] S. Y. Chen, Y. Tong, K.-K. Tseng, J. W. Yeh, D. Poplawsky, J. G. Wen, M. C. Gao, G. Kim, W. Chen, Y. Ren, R. Feng, W. D. Li, and P. K. Liaw, "Phase transformations of HfNbTaTiZr high-entropy alloy at intermediate temperatures", Scripta Materialia, 2019, 158, pp. 50-56.

[6] S. Y. Chen, X. Xie, B. L. Chen, J. W. Qiao, Y. Zhang, Y. Ren, K. A. Dahmen, and P. K. Liaw, "Effects of temperature on serrated flows of $Al_{0.5}$CoCrCuFeNi high-entropy alloy", Jom, 2015, 67(10), pp. 2314-2320.

[7] Y. Zhang, T. T. Zuo, Z. Tang, M. C. Gao, K. A. Dahmen, P. K. Liaw, and Z. P. Lu, "Microstructures and properties of high-entropy", Progress in Materials Science, 2014, 61, pp. 1-93.

[8] S. Chen, X. Xie, W. Li, R. Feng, B. Chen, J. Qiao, Y. Ren, Y. Zhang, K. A. Dahmen and P. K. Liaw, "Temperature effects on the serrated behavior of an Al 0.5 CoCrCuFeNi high-entropy alloy", Materials Chemistry and Physics, 2018, 210, pp. 20-28.

[9] J. Brechtl, S.Y. Chen, X. Xie, Y. Ren, J.W. Qiao, P.K. Liaw and S. J. Zinkle, "Towards a Greater Understanding of Serrated Flows in an Al-Containing HighEntropy-Based", International Journal of Plasticity, 2018, in press.

[10] M. Feuerbacher, M. Heidelmann, and C. Thomas, "Hexagonal High-entropy Alloys", Materials Research Letters, 2014, 3(1), pp. 1-6.

[11] L. Lilensten, J. P. Couzinié, L. Perrière, J. Bourgon, N. Emery, and I. Guillot, "TaNbHfZrTi New structure in refractory high-entropy alloys", Materials Letters, 2014, 132, pp. 123-125.

[12] K. M. Youssef, A. J. Zaddach, C. Niu, D. L. Irving, and C. C. Koch, "A novel low-density, high-hardness, high-entropy alloy with close-packed single-phase nanocrystalline structures", Materials Research Letters, 2014, 3(2), pp. 95-99.

[13] M. C. Gao, B. Zhang, S. M. Guo, J. W. Qiao and J. A. Hawk, "High-Entropy Alloys in Hexagonal Close-Packed Structure", Metallurgical and Materials Transactions A, 2015, 47(7), pp. 3322-3332.

[14] D. B. Miracle and O. N. Senkov, "A critical review of high entropy alloys and related concepts", Acta Materialia, 2017, 122, pp. 448-511.

[15] O. N. Senkov, J. M. Scott, F. Meisenkothen, S. V. Senkova, D. B. Miracle, and C. F. Woodward, "Microstructure and elevated temperature properties of a refractory TaNbHfZrTi alloy", J Mater Sci, 2012, 47, pp. 4062-4074

[16] O. N. Senkov, G. B. Wilks, J. M. Scott, and D. B. Miracle "Mechanical properties of $Nb_{25}Mo_{25}Ta_{25}W_{25}$ and $V_{20}Nb_{20}Mo_{20}Ta_{20}W_{20}$ refractory high entropy alloys", Intermetallics, 2012, 19, pp. 698-706

[17] M.H. Chuang, M.H. Tsai, W.R. Wang, S.J. Lin, and J.W. Yeh. Microstructure and wear behavior of $Al_xCo_{1.5}CrFeNi_{1.5}Ti_y$ high-entropy alloys. Acta Mater 2011, 59, pp. 6308–17.

[18] Y. Shi, B. Yang, X. Xie, J. Brechtl, K. A. Dahmen, and P. K. Liaw, "Corrosion of Al_xCoCrFeNi high-entropy alloys: Al-content and potential scan-rate dependent pitting behavior", Corrosion Science, 2017, 119, pp. 33-45.

[19] Y. Shi, B. Yang, and P. K. Liaw, "Corrosion-resistant high-entropy alloys: A review", Metals, 2017, 7(2), pp. 1-18.

[20] W.D. Li, G. Wang, S.W. Wu, and P.K. Liaw. “Creep, fatigue, and fracture behavior of high-entropy alloys”, Journal of Materials Research, 2018, 33(19), pp. 3011-3034.

[21] S. Y. Chen, W. D. Li, X. Xie, J. Brechtl, B. L. Chen, P. Z. Li, G. F. Zhao, F. Q. Yang, J. W. Qiao, K. A. Dahmen and P. K. Liaw, "Nanoscale serration and creep

characteristics of $Al_{0.5}$CoCrCuFeNi high-entropy alloys", Journal of Alloys and Compounds, 2018, 752, pp. 464-475.

[22] W. D. Li, P.K. Liaw, and Y. F. Gao. “Fracture resistance of high entropy alloys: A review”, Intermetallics, 2018, 99, pp. 69-83.

[23] B. Guennec, V. Kentheswaran, L .Perrière, A. Ueno, I. Guillot, J-Ph. Couzinié, G. Dirras, “Four-point bending fatigue behavior of an equimolar BCC HfNbTaTiZr high-entropy alloy: macroscopic and microscopic viewpoints”, Materialia, 2018, in press.

[24] M. A. Hemphill, T. Yuan, G. Y. Wang, J. W. Yeh, C. W. Tsai, A. Chuang, and P. K. Liaw, "Fatigue behavior of $Al_{0.5}$CoCrCuFeNi high entropy alloys", Acta Materialia, 2012, 60(16), pp. 5723-5734.

[25] Z. Tang, T. Yuan, C. W. Tsai, J. W. Yeh, C. D. Lundin, and P. K. Liaw, "Fatigue behavior of a wrought $Al_{0.5}$CoCrCuFeNi two-phase high-entropy alloy", Acta Materialia, 2015, 99, pp. 247-258.

[26] S. Shukla, T. Wang, S. Cotton, and R. S. Mishra, "Hierarchical microstructure for improved fatigue properties in a eutectic high entropy alloy", Scripta Materialia, 2018, 156, pp. 105-109.

[27] K. Liu, M. Komarasamy, B. Gwalani, S. Shukla, and R. S. Mishra, "Fatigue behavior of ultrafine grained triplex $Al_{0.3}$CoCrFeNi high entropy alloy", Scripta Materialia, 2019, 158, pp. 116-120.

[28] K. V. S. Thurston, B. Gludovatz, A. Hohenwarter, G. Laplanche, E. P. George, and R. O. Ritchie, "Effect of temperature on the fatigue-crack growth behavior of the high-entropy alloy CrMnFeCoNi", Intermetallics, 2017, 88, pp. 65-72.

[29] P. Chen, C. Lee, S. Y. Wang, M. Seifi, J. J. Lewandowski, K. A. Dahmen, H. Jia, X. Xie, B. Chen, J. W. Yeh, C. W. Tsai, T. Yuan, and P. K. Liaw, "Fatigue behavior of high-entropy alloys: A review", Science China Technological Sciences, 2017, 61(2), pp. 168-178.

[30] B. Gludovatz, A. Hohenwarter, D. Catoor, E. H. Chang, E. P. George and R. O. Ritchie, "A fracture-resistant high-entropy alloy for cryogenic applications", Science, 2014, 345(6201), pp. 1153-1160.

[31] W. H. Liu, Y. Wu, J. Y. He, T. G. Nieh, and Z. P. Lu, "Grain growth and the Hall–Petch relationship in a high-entropy FeCrNiCoMn alloy", Scripta Materialia, 2013, 68(7), pp. 526-529.

[32] Z. Wu, H. Bei, F. Otto, G. M. Pharr, and E. P. George, "Recovery, recrystallization, grain growth and phase stability of a family of FCC-structured multi-component equiatomic solid solution alloys", Intermetallics, 2014, 46, pp. 131-140.

[33] G. Dan Sathiaraj and P. P. Bhattacharjee, "Effect of cold-rolling strain on the evolution of annealing texture of equiatomic CoCrFeMnNi high entropy alloy", Materials Characterization, 2015, 109, pp. 189-197.

[34] O. N. Senkov and S. L. Semiatin, "Microstructure and properties of a refractory high-entropy alloy after cold working", Journal of Alloys and Compounds, 2015, 649, pp. 1110-1123.

[35] C.-C. Juan, M.-H. Tsai, C. W. Tsai, W. L. Hsu, C. M. Lin, S.-K. Chen, S. J. Lin, and J. W. Yeh, "Simultaneously increasing the strength and ductility of a refractory high-entropy alloy via grain refining", Materials Letters, 2016, 184, pp. 200-203.

[36] O. N. Senkov, A. L. Pilchak, and S. L. Semiatin, "Effect of cold deformation and annealing on the microstructure and tensile properties of a HfNbTaTiZr refractory high entropy alloy", Metallurgical and Materials Transactions A, 2018, 49(7), pp. 2876-2892.

[37] C. M. Cepeda-Jiménez, J. M. Molina-Aldareguia, and M. T. Pérez-Prado, "Effect of grain size on slip activity in pure magnesium polycrystals", Acta Materialia, 2015, 84, pp. 443-456.

[38] J. E. Burke and D. Turnbull, "Recrystallization and grain growth", Progress in metal physics, 1952, 3, 220-292.

[39] H. V. Atkinson, "Overview no. 65 Theories of normal grain growth in pure single phase systems", Acta Metall., 1988, 36(3), pp. 469-491.

[40] B. Cherukuri, R. Srinivasan, S. Tamirisakandala, and D. Miracle, "The influence of trace boron addition on grain growth kinetics of the beta phase in the beta titanium alloy Ti–15Mo–2.6Nb–3Al–0.2Si", Scripta Materialia, 2009, 60(7), pp. 496-499.

[41] Y. F. Xu, D. Q. Yi, H. Q. Liu, B. Wang, and F. L. Yang, "Age-hardening behavior, microstructural evolution and grain growth kinetics of isothermal ω phase of Ti–Nb–Ta–Zr–Fe alloy for biomedical applications", Materials Science and Engineering: A, 2011, 529, pp. 326-334.

[42] T. Wang, H. Guo, L. Tan, Z. Yao, Y. Zhao, and P. Liu, "Beta grain growth behaviour of TG6 and Ti17 titanium alloys", Materials Science and Engineering: A, 2011, 528(21), pp. 6375-6380.

[43] E.O. Hall, "The Deformation and Ageing of Mild Steel: III Discussion of Results", Proceedings of the Physical Society, 1951, B64, pp. 747-753.

[44] N.J. Petch, "The cleavage strength of polycrystals", Journal of the Iron and Steel Institute, 1953, 174, pp. 25-28.

[45] N. Hansen, "Hall–Petch relation and boundary strengthening", Scripta Materlia, 2004, 51, pp. 801-806.

[46] Z. C. Cordero, B. E. Knight and C. A. Schuh, "Six decades of the Hall Petch effect a survey of grain size strengthening studies on pure metals", International Materials Reviews, 2016, 61, pp. 495-512.

[47] M. A. Meyers and K. K. Chawla, Mechanical Metallurgy-principles and applications, Prentice-Hall, Inc., New Jersey, 1984, pp. 502-506.

[48] X. H. Dong, X. T. Hong, F. Chen, B. R. Sang, W. Yu and X. P. Zhang, "Effects of specimen and grain sizes on compression strength of annealed wrought copper alloy at room temperature", Materials & Design, 2014, 64, pp. 400-406.

[49] L. L. Chang, Y. N. Wang, X. Zhao and M. Qi, "Grain size and texture effect on compression behavior of hot-extruded Mg–3Al–1Zn alloys at room temperature", Materials Characterization, 2009, 60(9), pp. 991-994.

[50] J. A. del Valle, F. Carreño and O. A. Ruano, "Influence of texture and grain size on work hardening and ductility in magnesium-based alloys processed by ECAP and rolling", Acta Materialia, 2006, 54(16), pp. 4247-4259.

[51] H. Y. Yasuda, H. Miyamoto, K. Cho and T. Nagase, "Formation of ultrafine-grained microstructure in Al 0.3 CoCrFeNi high entropy alloys with grain boundary precipitates", Materials Letters, 2017, 199, pp. 120-123.

[52] F. Otto, A. Dlouhý, C. Somsen, H. Bei, G. Eggeler and E. P. George, "The influences of temperature and microstructure on the tensile properties of a CoCrFeMnNi high-entropy alloy", Acta Materialia, 2013, 61(15), pp. 5743-5755.

[53] S. Yoshida, T. Bhattacharjee, Y. Bai and N. Tsuji, "Friction stress and Hall-Petch relationship in CoCrNi equi-atomic medium entropy alloy processed by severe plastic deformation and subsequent annealing", Scripta Materialia, 2017, 134, pp. 33-36.

[54] B. Kang, J. Lee, H. J. Ryu and S. H. Hong, "Ultra-high strength WNbMoTaV high-entropy alloys with fine grain structure fabricated by powder metallurgical process", Materials Science and Engineering: A, 2018, 712, pp. 616-624.

[55] B. Kang, J. Lee, H. J. Ryu and S. H. Hong, "Microstructure, mechanical property and Hall-Petch relationship of a light-weight refractory Al 0.1 CrNbVMo high entropy alloy fabricated by powder metallurgical process", Journal of Alloys and Compounds, 2018, 767, pp. 1012-1021.

[56] S. Maiti and W. Steurer, "Structural-disorder and its effect on mechanical properties in single-phase TaNbHfZr high-entropy alloy", Acta Materialia, 2016, 106, pp. 87-97.

[57] M. Gao and D. Alman, "Searching for Next Single-Phase High-Entropy Alloy Compositions", Entropy, 2013, 15(10), pp. 4504-4519

[58] C. Lee, G. Song, M. C. Gao, R. Feng, P. Chen, J. Brechtl, Y. Chen, K. An, W. Guo, J. D. Poplawsky, S. Li, A. T. Samaei, W. Chen, A. Hu, H. Choo and P. K. Liaw, "Lattice Distortion in a Strong and Ductile Refractory High-entropy Alloy", Acta Materialia, 2018.

[59] P. P. Bhattacharjee, G. D. Sathiaraj, M. Zaid, J. R. Gatti, C. Lee, C.-W. Tsai and J.-W. Yeh, "Microstructure and texture evolution during annealing of equiatomic CoCrFeMnNi high-entropy alloy", Journal of Alloys and Compounds, 2014, 587, pp. 544-552.

[60] O. N. Senkov, D. B. Miracle, K. J. Chaput and J.-P. Couzinie, "Development and exploration of refractory high entropy alloys—A review", Journal of Materials Research, 2018, pp. 1-37.

[61] S. I. Rao, C. Varvenne, C. Woodward, T. A. Parthasarathy, D. Miracle, O. N. Senkov and W. A. Curtin, "Atomistic simulations of dislocations in a model BCC multicomponent concentrated solid solution alloy", Acta Materialia, 2017, 125, pp. 311-320..

Appendix

Table 2. 1. The average grain sizes of the HfNbTaTiZr HEAs, including our samples cold-rolled to a 70% thickness reduction and annealed at various temperatures and times, as well as those compiled from literature [34, 36].

Temperature (℃)	*t* (h)	D (μm) 70%	D (μm) [34] 65%	D (μm) [34] 84.6%	D (μm) [36] 89%
1,000	0.5	27	-	-	-
	2	31.5	35	22	21.9
	6	39.1	-	-	-
	24	62	-	-	-
1,100	0.5	43	-	-	24.4
	2	62.5	-	-	38.4
	6	87	-	-	-
	24	151	-	-	-
1,200	0.5	53	-	-	-
	2	79	91	76	75.5
	6	111.7	-	-	-
	24	206	-	-	-

Table 2. 2. The n and k values evaluated at different annealing temperatures

Temperature (℃)	n	k (m^n/s)
1,000	2.4	1.8×10^{-15}
1,100	2.4	7.9×10^{-15}
1,200	2.2	1×10^{-13}

Table 2. 3. The dependence of yield strength, UTS, and elongation on grain sizes.

Grain size (μm)	Yield strength (MPa)	UTS (MPa)	Fracture elongation (in strain)
40	985	1,004	0.157
87	972	999.5	0.126
112	967	980.6	0.108

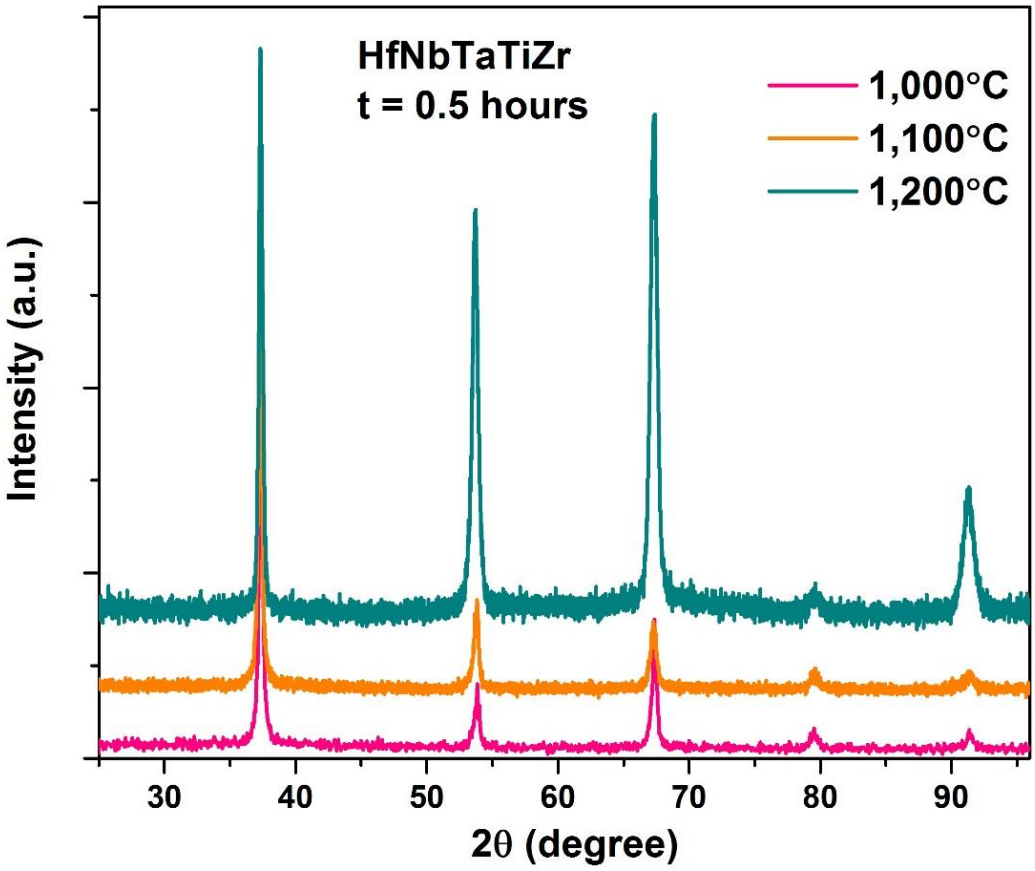

Figure 2. 1. XRD patterns of the HfNbTaTiZr HEAs annealed at 1,000, 1,100, and 1,200 ^{o}C for 0.5 hours.

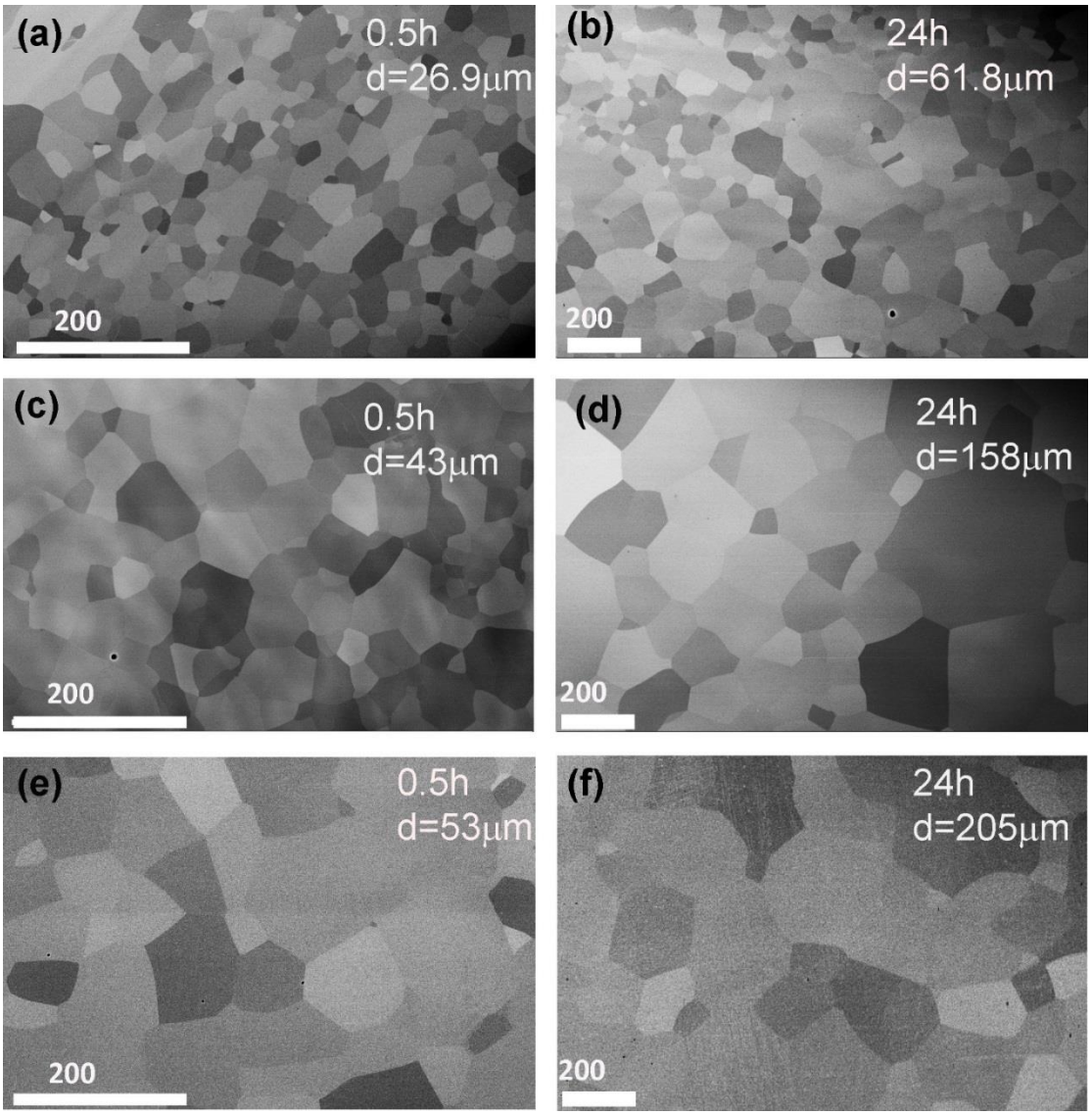

Figure 2. 2. SEM images of the microstructures of the HEAs, annealed at 1,000 ºC for (a) 0.5 and (b) 24 hours, 1,100 ºC for (c) 0.5 and, (d) 24 hours, and 1,200 ºC for (e) 0.5 and (f) 24 hours.

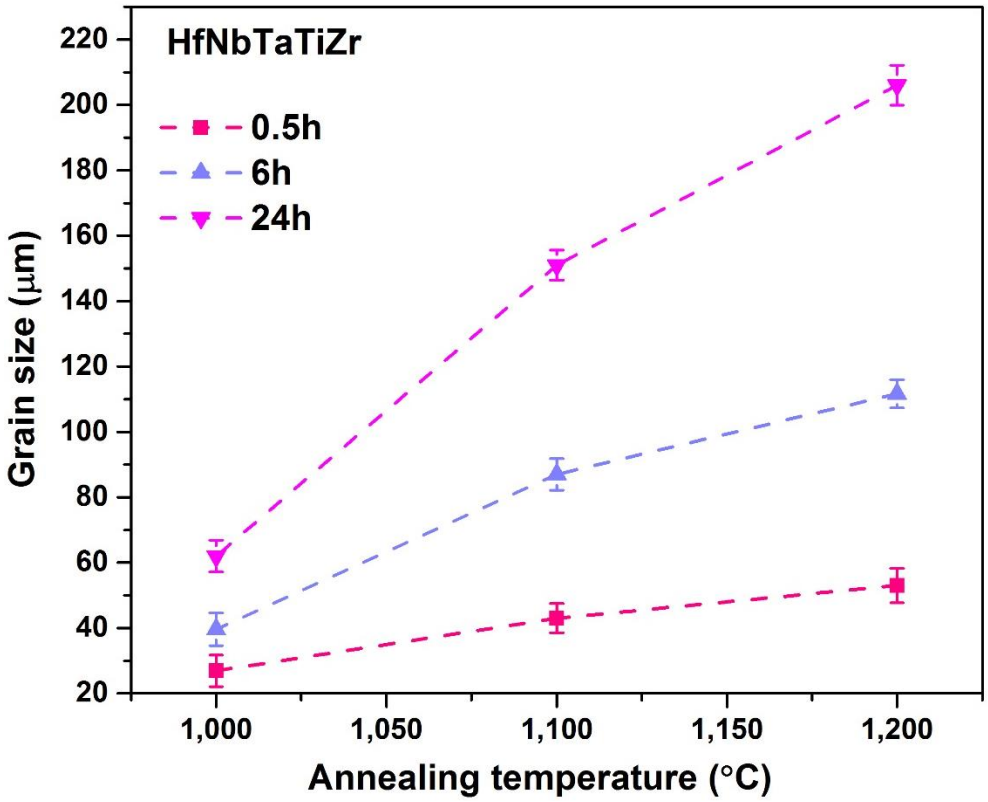

Figure 2. 3. The variations of the average grain sizes of the HfNbTaTiZr HEAs with the annealing temperature and time. The average grain sizes are determined by applying the linear-intercept method to the SEM images of the microstructures.

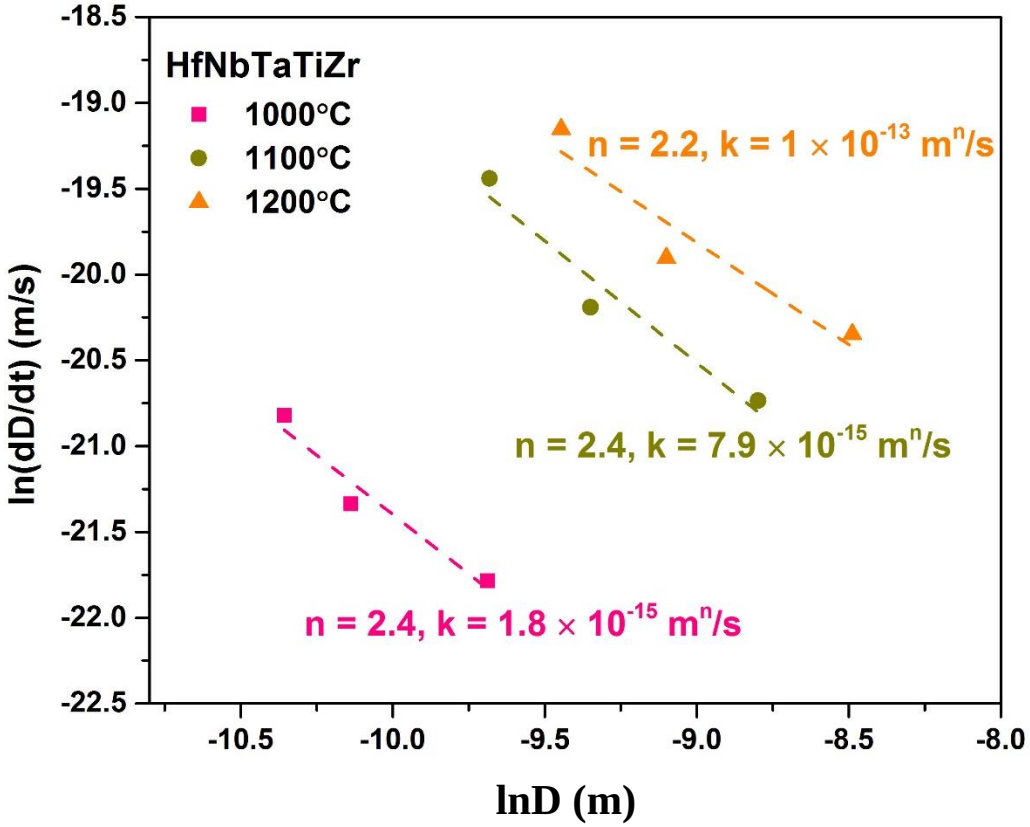

Figure 2. 4. Linear fitting of Eq. (2) to the logarithm of the average grain size versus the logarithm of the dD/dt for the HfNbTaTiZr HEAs annealed at 1,000, 1,100, and 1,200 ^{o}C. From the slopes, the values of the grain growth-exponents, *n*, are determined.

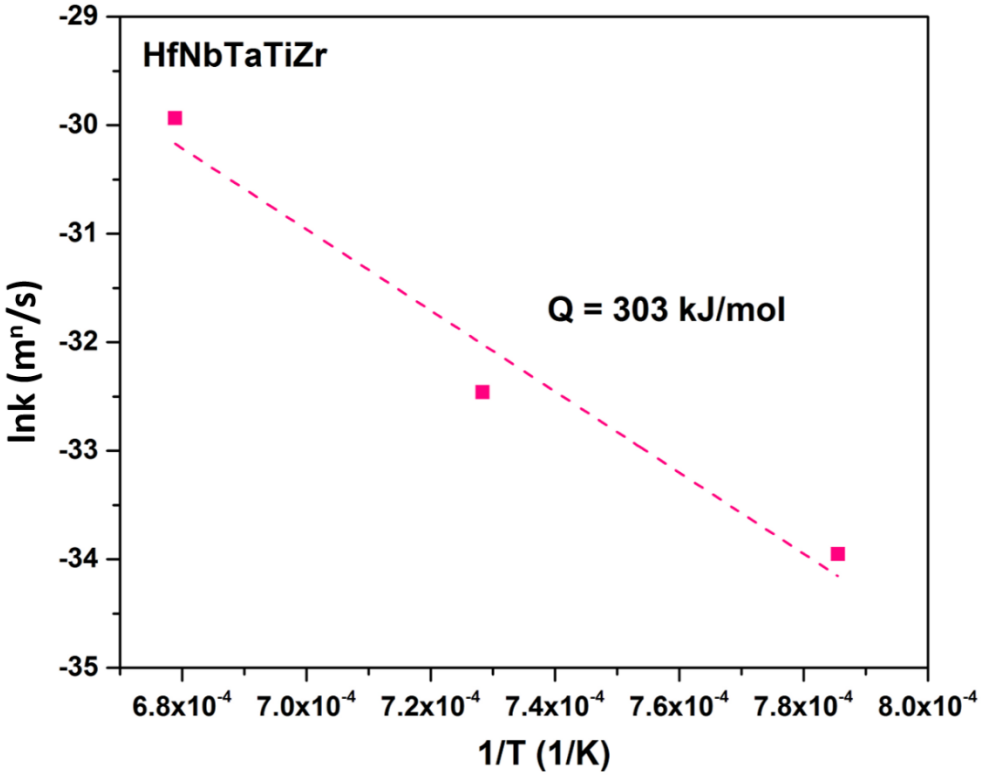

Figure 2. 5. Linear fitting of Eq. (5) to lnk data against $1/T$, from which the activation energies, Q_g, is obtained from the slope.

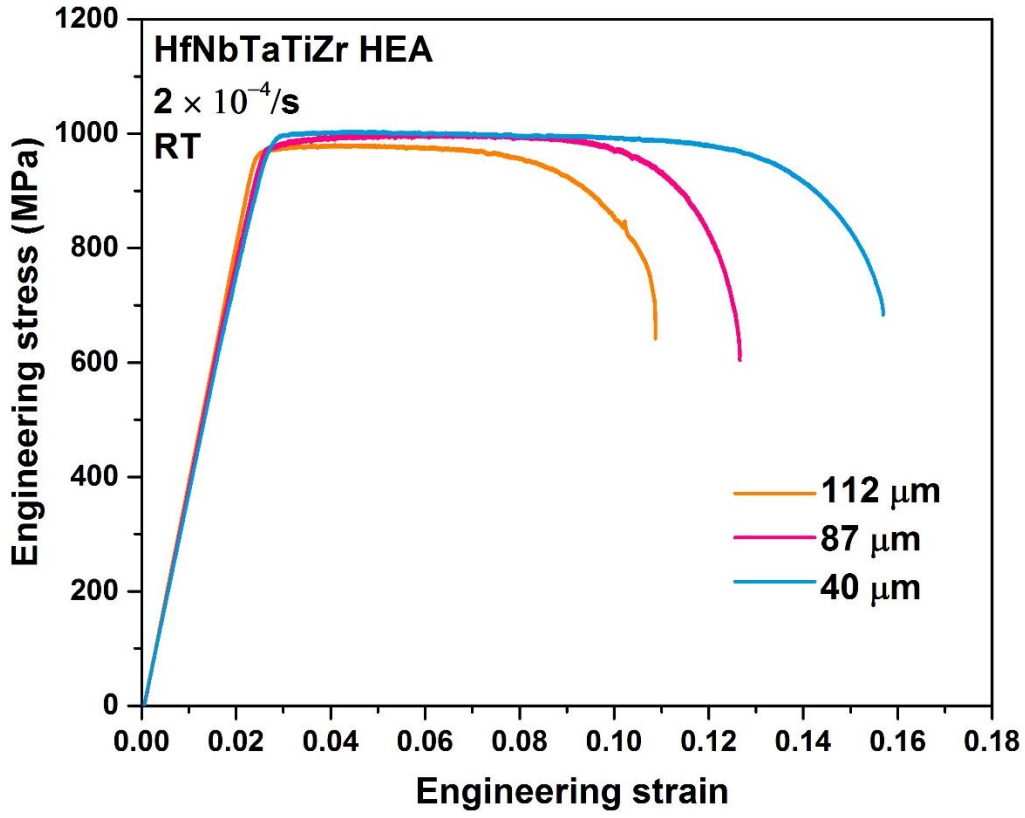

Figure 2. 6. Uniaxial tensile true stress – strain curves of the HfNbTaTiZr HEAs with the grain sizes of 40, 87, and 112 μm, tested at room temperature and a strain rate of 2×10^{-4} s^{-1}.

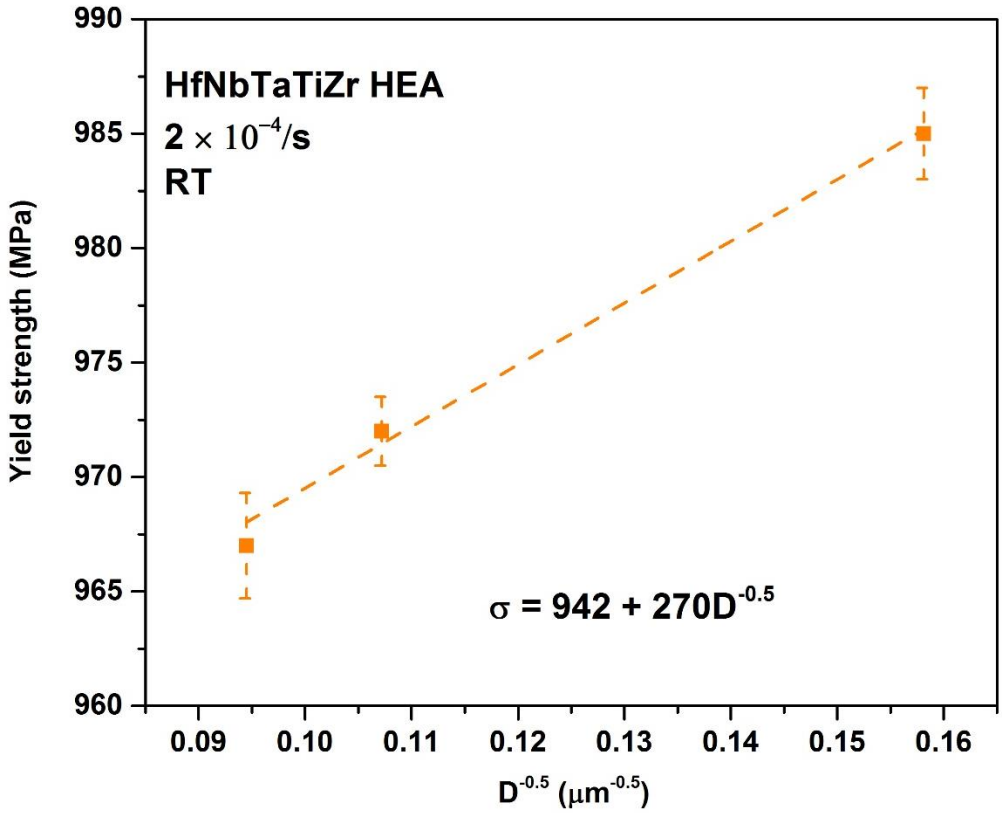

Figure 2. 7. Linear fitting of Hall-Petch relation [i.e., Equation (6)] to the experimental yield strength data as a function of $D^{-0.5}$ for the HfNbTaTiZr HEAs, from which σ_0 and k_{HP} are determined to be 942 MPa and 270 MPa/μm$^{-1/2}$ from the intercept and slope, respectively.

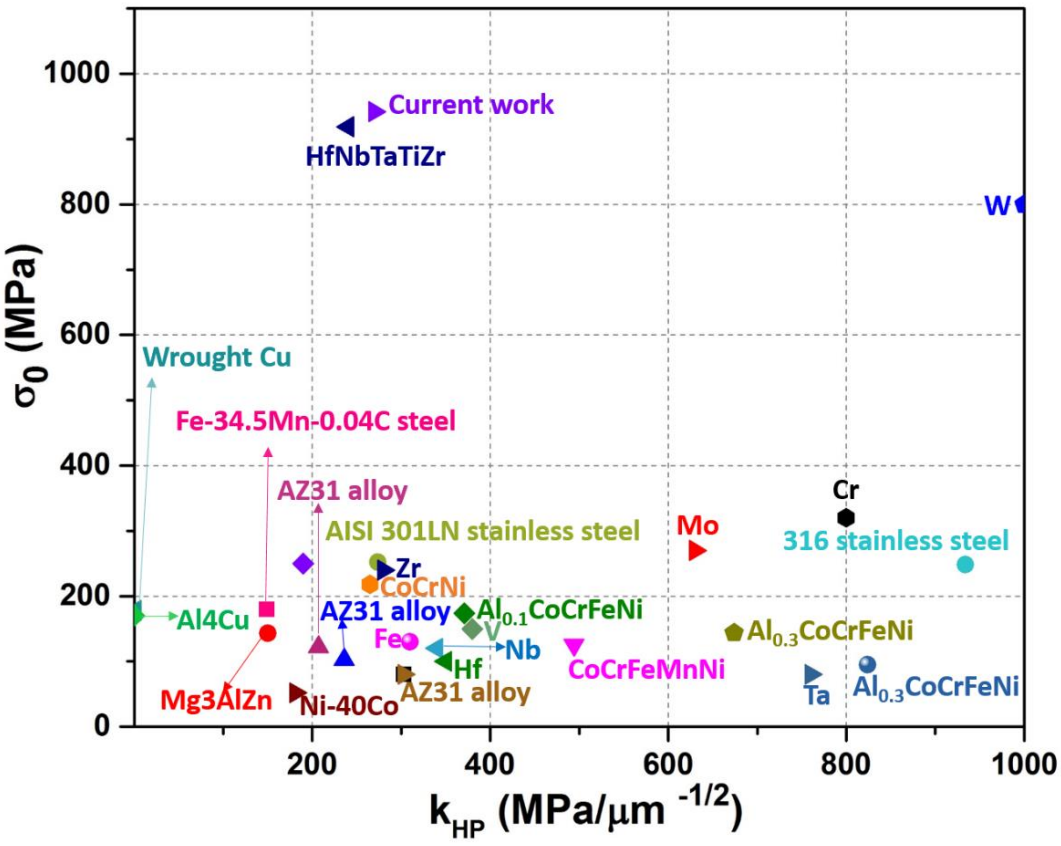

Figure 2. 8. The comparison of σ_0 and k_{HP} between the current HEA and conventional alloys [33-55].

CHAPTER III TEMPERATURE DEPENDENCE OF THE MECHANICAL PROPERTIES OF THE BODY-CENTERED CUBIC HFNBTATIZR HEA

This article in the same form will be submitted to Scripta Materialia.

Authors:

S.Y. Chen, L. Wang, W.D. Li, Yang Tong, Y. Ren, and P.K. Liaw

Department of Materials Science and Engineering, The University of Tennessee, Knoxville, TN 37996, USA

K.-K. Tseng and J.-W. Yeh

Department of Materials Science and Engineering, National Tsing Hua University, Hsinchu, 30013, Taiwan

Y. Ren

X-ray Science Division, Argonne National Laboratory, Argonne, IL 60439, USA

Abstract

The temperature effect on the mechanical properties of the HfNbTaTiZr HEA was investigated by conducting uniaxial tensile tests in the temperature range from 77 to 673 K. The decrease of the yield strength with increasing temperature was mechanistically analyzed by considering contributions from various strengthening mechanisms, ultimately leading to an estimate of the dislocation width of $\omega_0 = 0.74b$, where b is the magnitude of the Burgers vector. An anomaly in strain hardening was observed at elevated temperatures – the strain-hardening exponent decreases expectedly from 77 K to 298 K but reverts to an anomalous ascending trend afterwards. Microstructural probing (Synchrotron diffractions, TEM, and APT) precludes precipitation hardening. Flow serrations at 673 K implies the dynamic strain aging (DSA) as an extra strengthening mechanism contributing to the intensified strain hardening at elevated temperatures. A model was constructed to split the overall strain hardening into forest hardening and DSA hardening, both of which were theoretically quantified at all temperatures considered.

The concept of high-entropy alloys (HEAs), a new strategy to design alloys, was proposed and developed in 2000's [1, 2]. Five or more principal elements, with an equal or near-equal atomic percentage, are included in alloys, which can be distinguished from conventional alloys with one or two based elements as major constituents.

Many different multi-components HEA systems have been investigated since the concepts was first proposed. Even though some multi-component alloys include intermetallic compounds, simple single phase structure, for example, face-centered-cubic (FCC) [3-6],

body-centered-cubic (BCC) [7-9], or hexagonal-closed-packed (HCP) [10-13] structure is typically observed in most HEAs.

The refractory HEAs were proposed by Senkov et al. [7], composing of elements with high melting temperatures, to meet the high-temperature load-bearing and thermal protection for the aerospace industry. The compression tests from room temperatures to 1200C in the as-cast HfNbTaTiZr refractory alloy with a single BCC structure have been investigated by Senkov et al [14]. Later, tension experiments at room temperature were performed in as-cast and annealed specimens as well [15-22]. Surprisingly, they demonstrate superior yield strength and good ductility. Actually, temperature effect on tensile properties in BCC solid solution HEAs have been investigated less comprehensively than fcc HEA. For instance, most of the mechanical behavior at cryogenic temperature were investigated in fcc HEA, rare studies were conducted in bcc HEAs. Only Podolskiy et al. [23] firstly investigate the compression properties in Ti30Zr25Hf15Nb20Ta10 HEA at cryogenic temperatures, i.e. from 4.2 K to 230K. On the one hand, more than 1.5GPa of yield strength with good ductility could be found in samples compressed at temperature of 77K and above. On the other hand, specimen deformed at 4.2K present much higher yield strength but limited ductility, which was explained in terms of the nucleation and expansion of the kink pairs at dislocation lines [23]. The research on bcc refractory alloys has increased enormously in view of their prospective technical importance. Thus, it is essential to study the temperature effect on the tensile properties in HfNbTaTiZr bcc HEA.

The preparation and processing of the HfNbTaTiZr alloy followed the steps in Ref. [9]. Flat dog-bone tensile specimens with a 19 mm gauge were machined from the finally

cold-rolled alloy sheets, with their longitudinal axes perpendicular to the rolling direction. Grinding and polishing was applied to each specimen, after which the sample thickness and gauge section width are about 0.9 mm and 3.15 mm, respectively. Uniaxial tensile tests were conducted on a Material Test System (MTS) servohydraulic machine under displacement control, at a strain rate of 1×10^{-4} s^{-1} and temperatures of 77 K, 298K, 573K, and 673K. At least three tests were repeated for each testing condition. The carry-out of the cryogenic tests followed the procedure described in Ref. [24]. The microstructures of the deformed samples at varied temperatures were characterized with high-energy X-ray diffraction on the 11-ID-C beamline with a beam energy of 115.27 keV, located at the Advanced Photon Source (APS) of the Argonne National Laboratory. Fracture surface morphology and crack propagation trajectories in all samples were imaged with the LEO-1525 scanning electron microscope (SEM).

Figure 3. 1(a) representatively presents the tensile engineering stress – strain curves of the HfNbTaTiZr HEA tested at temperatures from 77 K to 673 K. Analogous to the vast majority of crystalline metals, the increase in temperature intensifies ductility and yet brings downs the yield stress and flow stress, as shown separately by symbols in Figure 3. 1(b) and (c). Also noted in Figure 3. 1(a) is that the flow serration takes place on the 673 K curve, as demonstrated by the inset.

A feature in Figure 3. 1(a) that distinguishes this HEA from other crystalline metals and HEAs is that its strain hardening after 298 K seems to enhance as temperature goes high. According to the Hollomon power law of $\sigma = A\varepsilon_{\mathrm{p}}^{n}$, where the strain-hardening exponent,n, for each temperature is computed by performing a $\log\sigma$ – $\log\varepsilon_{\mathrm{p}}$ fit to the true

flow stress against the true plastic strain up to necking. n values evaluated at all temperatures are plotted in Figure 3. 1(d). The plot confirms the visual inspection in Figure 3. 1(a), that is, the strain-hardening capability, as reflected by n values, first decreases from 77 K to 298 K, then reverts to an ascending trend as temperature further increases. The decline in strain hardening from 77 K to 298 K is somewhat expected. However, its increase from 298 K to 673 K is completely counterintuitive, because strain hardening in most metals, e.g., all subsets of the fcc FeNiCoCrMn HEA [24], is deteriorated by elevated temperatures. This anomaly in strain hardening is intriguing and will be examined in detail shortly.

The specimens failed at 298 K and 673 K are selected for fractographic analyses. Their side and top views are presented in the first and second column in Figure 3. 2, respectively. Up on failure, the degrees of macroscopic necking at these two temperatures are quite comparable (at least no significant difference is noticed). Recalling from Figure 3. 1(a) and (b) that the alloy's ductility indeed increases significantly from 298 K to 673 K, we can reason that intensified strain hardening has already occurred to the alloy at 673 K in comparison to that at 298 K so as to postpone the onset of necking instability. This fractographic observation is essentially consistent with the strain-hardening trend reported in Figure 3. 1(a) and (d), that is, the alloy at 673 K has a greater strain hardening capability than the alloy at 298 K. Microscopically, the specimen at 673 K exhibits more extensive slip lines than that at 298 K, as evidenced from comparing Figure 3. 2(a_3) and (b_3). Also, a larger-scale dimples of varying sizes are detected in the former than in the latter, as seen

from Figure 3. 2(a_4) and (b_4). All these reaffirm that the alloy at a higher temperature has a manifestation of larger ductility.

The temperature dependence of the yield strength σ_y can by analyzed by firstly considering all possible strengthening mechanisms contributing to σ_y, i.e.,

$$\sigma_y = \sigma_{fr} + \sigma_{\rho i} + \sigma_{ss} + \sigma_{ppt} + \sigma_{gb}, \quad (1)$$

where σ_{fr}, $\sigma_{\rho i}$, σ_{ss}, σ_{ppt}, and σ_{gb} are the contributions from the lattice friction, initial dislocation density, solid-solution hardening, precipitation hardening, and grain-boundary hardening, respectively. Given that the alloy examined was well annealed, $\sigma_{\rho i}$ should be very limited and is approximated as zero. σ_{ppt} is treated as zero also considering the absence of precipitates at all temperatures (microscopic evidences will be provided shortly). σ_{gb} is assumed to be zero in light of Ref. [24]. Finally, analogous to Wu et al. [24], σ_{ss} is folded into σ_{fr} to form the average lattice friction over all solute atoms in a concentrated solid solution, i.e., $\bar{\sigma}_{fr}$. $\bar{\sigma}_{fr}$ is normally represented by the Peierls stress, σ_p, and its dependence on temperature is theoretically expressed as [1]

$$\sigma_y(T) = \bar{\sigma}_{fr}(T) = \sigma_p = \frac{2G}{1-\nu} \exp\left(\frac{-2\pi\omega_0}{b}\right) \exp\left(\frac{-2\pi\omega_0}{b} \alpha T\right), \quad (2)$$

where G is the shear modulus, ν is the Poisson's ratio, ω_0 is the dislocation width at 0 K, b is the magnitude of the Burgers vector, α is a constant, and T is the temperature. Experimentally, the temperature dependence of σ_y may be empirically fitted by the following exponential decay

$$\sigma_y = \sigma_a \exp\left(\frac{-T}{C}\right) + \sigma_b, \quad (3)$$

where σ_a, σ_b, and C are all fitting constants. Fitting Eq. (3) to the measured σ_y at different temperatures in Figure 3. 1(c) yields the values of three fitting parameters, as listed in Table 3. 1. By examining the functional form of Eqs. (2) and (3), it is not difficult to recognize that $\sigma_a = \frac{2G}{1-v}\exp\left(\frac{-2\pi\omega_0}{b}\right)$ and $C = \frac{b}{2\pi\omega_0\alpha}$. With $\sigma_a = 892.8$ MPa, $G =$ 31 GPa, $v = 0.32$, $\frac{\omega_0}{b}$ is calculated to be 0.74, i.e., $\omega_0 = 0.74b$. Further, with $C = 874.6$ K and $\frac{\omega_0}{b} = 0.74$, α is computed to be 2.5×10^{-4} K^{-1}.

The importance of the analysis on the temperature dependence of yield strength is that it confirms that the equiatomic bcc HfNbTaTiZr HEA has a narrower dislocation width than the equiatomic fcc solid solution alloys who have $\omega_0 = b$ [24]. This trend indicates that the former has a stronger Peierls barrier than the latter.

Also interesting is the anomalous temperature dependence of the strain-hardening exponent in Figure 3. 1(d) at temperatures greater than 298 K – normally strain hardening of metals drops as temperature increases due to the high-temperature dynamic recovery [24-26]. The strengthened strain hardening at elevated temperatures in Figure 3. 1(d) implies the involvement of one or more extra hardening mechanisms. The first possible extra hardening mechanism is precipitation hardening, likely caused by the high-temperature-promoted precipitation of second phases. The second possible source is the dynamic strain aging (DSA), as clued from the serrated plastic flow on the stress-strain curve at 673 K in Figure 3. 1(d).

We first examine the likelihood of precipitation hardening. The synchrotron diffractions on the failed specimens at four temperatures are provided in Figure 3. 3(a).

From the diffraction peaks, the bcc structure is identified as the only phase at all temperatures, affirming the nonexistence of second phases in an appreciable amount or large sizes. The possibility of second phases appearing in a small amount or nano sizes is surveyed by conducting transmission electron microscope (TEM) and atom probe tomography (APT) analyses at multiple randomly-selected locations on the failed samples. All investigations do not reveal any detectable second phases at the nano scale, as representatively shown by the TEM image of the samples at 77 K in Figure 3. 3(b) and 673 K in Figure 3. 3(c), also the uniform APT elemental distributions in Figure 3. 3(d). The TEM and APT analyses further preclude the precipitation of nano-sized second-phase particles in any amount. Accordingly, precipitation hardening is eliminated as an extra hardening mechanism at elevated temperatures.

Up to this point, it is rational to assert that the enhanced strain hardening in the present HEA at temperatures greater than 298 K stems from dynamic strain aging (DSA), an acknowledged strengthening mechanism in alloys that could cause serrations on their stress-strain curves [27, 28]. In solid-solution alloys without DSA, strain hardening is exclusively attributed to the mutual interaction of mobile dislocations and obstacles (i.e., forest dislocations) [29]. In this case, forest hardening is the only source of strain hardening [29, 30], i.e.,

$$\Delta\sigma = \sigma_f(\varepsilon, T), \tag{4}$$

where $\Delta\sigma$ is the extent of strain hardening defined as the difference between the flow stress and the yield strength, $\sigma_f(\varepsilon, T)$ is the forest hardening depending on the plastic strain and temperature. In the presence of DSA, solute atoms diffuse around dislocations

while they are arrested by obstacles for a certain time [30, 31]. This process strengthens the obstacles held on the dislocations and, therefore, provides an additive strengthening on top of the foresting hardening [31, 32]. In such a scenario, the extent of strain hardening consists of two contributions given by

$$\Delta\sigma = \sigma_f(\varepsilon, T) + \sigma_{DSA}(\dot{\varepsilon}, T), \quad (5)$$

where $\sigma_{DSA}(\dot{\varepsilon}, T)$ is the strengthening effect from DSA, which depends on the temperature and strain rate according to prior reports [33, 34].

With the above framework laid out, it is likely to quantify the contribution of forest hardening and DSA hardening to strain hardening in the HfNbTaTiZr HEA at various temperatures. Here we reason that the strain hardening at low temperatures (77 and 298 K) is merely attributed to forest hardening. On the other hand, forest hardening and DSA hardening constitute the strain hardening at high temperatures (573 and 673 K). The reasoning is on the basis of the contrasting strain-hardening trends at low and high temperature ranges [cf. Figure 3. 1(d)] as well as the observation of flow serrations at 673 K. It is worth noting that although serrations are absent at 573 K, most likely DAS is still an valid strengthening mechanism at this temperature, considering (1) the alloy at this temperature exhibits similar hardening characteristics with that at 673 K and (2) the serrated flow is not necessarily always visible up on DSA [34]. Given that forest hardening presents in the alloy at all temperatures, we first evaluate its contribution to strain hardening. According to Ref. [30], forest strengthening in an alloy can be written as

$$\sigma_f = \omega A \frac{\sqrt{\rho_f}}{b}, \quad (6)$$

where ω is a constant, b is the magnitude of Burgers vector, ρ_f is the forest dislocation density, and $A = \frac{3Gb^2}{4\pi(1-\nu)}$ with G and ν the shear modulus and Poisson's ratio, respectively. Eq. (6) essentially has the same functional form as the classical Taylor model [35]. The evolution of the forest dislocation density with plastic strain follows the general form of [30]

$$\rho_f(\varepsilon_p) = \rho_f^{sat}\left(1 - \exp\left(-\left(\varepsilon_p/\bar{\varepsilon}_p\right)^p\right)\right), \tag{7}$$

where $\bar{\varepsilon}_p$ and p are constants, ρ_f^{sat} is the saturated forest dislocation density at a given temperature. Apparently, ρ_f^{sat} decreases with increasing temperature. Inspired by prior reports [36, 37], the dependence of ρ_f^{sat} on temperature is assumed to follow an exponential decay

$$\rho_f^{sat}(T) = \rho_{f,0}^{sat}\exp(-\zeta T), \tag{8}$$

where $\rho_{f,0}^{sat}$ is the zero-temperature forest dislocation density, ζ is a constant, and T is the temperature. Combining Eqs. (6) – (8), one can obtain the ultimate forest-strengthening model as a function of the plastic strain, ε_p and temperature, T

$$\sigma_f(\varepsilon_p, T) = \xi\frac{A}{b}\sqrt{\exp(-\zeta T)\left(1 - \exp\left(-\left(\varepsilon_p/\bar{\varepsilon}_p\right)^p\right)\right)}, \tag{9}$$

where $\xi = \omega\sqrt{\rho_{f,0}^{sat}}$ is a constant. For the HfNbTaTiZr HEA, b and A are determined to be 2.944 Å and 0.6 eV/Å, respectively; ξ, ζ, $\bar{\varepsilon}_p$, and p are adjustable parameters that need to be evaluated by fitting the model to the measurement data.

The extent of strain hardening ($\Delta\sigma = \sigma_{flow} - \sigma_y$) vs. true plastic strain (ε_p) for the HfNbTaTiZr from 77 to 673 K are provided in Figure 3. 4(a) (Note that in the process of

generating these strain-hardening curves, data are downsampled and the flow serrations are consequently erased). Given that forest hardening is the only strain-hardening source in the alloy at 77 and 298 K, ξ, ζ, $\bar{\varepsilon}_p$ and p values are determined through a simultaneous fitting of Eq. (9) to the strain-hardening curves at these two temperatures by meeting an objective of minimizing $wt_{77}\sum_{i=1}^{n}\left(\frac{\Delta\sigma_i^p-\Delta\sigma_i^m}{\Delta\sigma_i^m}\right)^2+wt_{298}\sum_{j=1}^{k}\left(\frac{\Delta\sigma_j^p-\Delta\sigma_j^m}{\Delta\sigma_j^m}\right)^2$, where $wt_{77}=0.5$ and $wt_{298}=0.5$ are the weights of the 77 and 298 K data sets, n and k are the total numbers of data points in the 77 and 298 K data sets, $\Delta\sigma_i^p$, $\Delta\sigma_i^m$, $\Delta\sigma_j^p$, and $\Delta\sigma_j^m$ are the predicted and measured $\Delta\sigma$ of the 77 and 298 K data sets. With the best-fit curves at 77 and 298 K shown in Figure 3. 4(a), the parameter values thereby determined are listed in Table 3. 2. It is appropriate to believe that the resulting forest-hardening model is applicable to the same alloy at 573 and 673 K. With the parameter values in Table 3. 2, the model in Eq. (9) predicts the forest hardening at 573 and 673 K as the blue and green curves in Figure 3. 4(a). Two striking features are noted in Figure 3. 4(a). Firstly, if only looking at the predicted curves, forest hardening becomes weakened as temperature increases, a trend in line with that in conventional metals [35] and FCC HEAs [24]. Secondly, the difference between the measured overall strain hardening and the predicted forest strain hardening at 573 and 673 is due to the DSA hardening according to Eq. (5).

The magnitude of DSA hardening at 573 and 673 K may be estimated by simply subtracting the predicted curves from the measured data in Figure 3. 4(a). The resulting DSA hardening as a function of plastic strain at the two temperatures is graphed in Figure 3. 4(b). DSA hardening boosts with increasing plastic strain because larger plastic

deformation is inclined to induce more dislocations, thereby expanding the scale of the DSA occurrence. The DSA hardening estimated in this way accounts for the integrated effect from both mobile dislocations and forest dislocations. With more rigorous theoretical treatments, the DSA hardening resulting from these two different types of dislocations may be separated [30, 38], which can be the future work.

As a final note, it is noticed that the dislocations in Figure 3. 3(b) and (c) manifest different appearances: a relatively low density of bent dislocations with the occasional formation of loops at 77 K versus a relatively-high density of straight dislocations at 673 K. It is conjectured that the difference is associated with the solute drag in the DSA process occurring merely at 673 K – the solute drag likely exerts constraints at two ends of a dislocation line to straighten it. Certainly, this conjecture requires future justification.

In conclusion, the temperature effect on the mechanical properties of the was investigated by conducting uniaxial tensile tests in the temperature range from 77 to 673 K. The decrease of the yield strength with increasing temperature was mechanistically analyzed by considering contributions from various strengthening mechanisms, ultimately leading to an estimate of the dislocation width of $\omega_0 = 0.74b$, where b is the magnitude of the Burgers vector. An anomaly in strain hardening was observed at elevated temperatures – the strain-hardening exponent decreases expectedly from 77 K to 298 K but reverts to an anomalous ascending trend afterwards. Microstructural probing (Synchrotron diffractions, TEM, and APT) precludes precipitation hardening. Flow serrations at 673 K implies the dynamic strain aging (DSA) as an extra strengthening mechanism contributing to the intensified strain hardening at elevated temperatures. A model was constructed to

split the overall strain hardening into forest hardening and DSA hardening, both of which were theoretically quantified at all temperatures considered.

References

[1] J. W. Yeh, S. K. Chen, S. J. Lin, J. Y. Gan, T. S. Chin, T. T. Shun, C. H. Tsau, and S. Y. Chang, "Nanostructured high-entropy alloys with multiple principal elements: novel alloy design concepts and outcomes", Advanced Engineering Materials, 2004, 6(5), pp. 299-303.

[2] B. Cantor, I. T. H. Chang, P. Knight, and A. J. B. Vincent, "Microstructural development in equiatomic multicomponent alloys", Materials Science and Engineering A, 2004, 375-377, pp. 213-218.

[3] S. Y. Chen, X. Xie, B. L. Chen, J. W. Qiao, Y. Zhang, Y. Ren, K. A. Dahmen, and P. K. Liaw, "Effects of temperature on serrated flows of $Al_{0.5}$CoCrCuFeNi high-entropy alloy", Jom, 2015, 67(10), pp. 2314-2320.

[4] Y. Zhang, T. T. Zuo, Z. Tang, M. C. Gao, K. A. Dahmen, P. K. Liaw, and Z. P. Lu, "Microstructures and properties of high-entropy", Progress in Materials Science, 2014, 61, pp. 1-93.

[5] S. Chen, X. Xie, W. Li, R. Feng, B. Chen, J. Qiao, Y. Ren, Y. Zhang, K. A. Dahmen and P. K. Liaw, "Temperature effects on the serrated behavior of an Al 0.5 CoCrCuFeNi high-entropy alloy", Materials Chemistry and Physics, 2018, 210, pp. 20-28.

[6] J. Brechtl, S.Y. Chen, X. Xie, Y. Ren, J.W. Qiao, P.K. Liaw and S. J. Zinkle, "Towards a Greater Understanding of Serrated Flows in an Al-Containing High Entropy-Based", International Journal of Plasticity, 2019, 115, pp. 71–92.

[7] O. N. Senkov, G. B. Wilks, D. B. Miracle, C. P. Chuang, and P. K. Liaw, "Refractory high-entropy ", Intermetallics, 2010, 18, pp. 1758-1765.

[8] O. N. Senkov, J. M. Scott, S. V. Senkova, D. B. Miracle, and C. F. Woodward, "Microstructure and room temperature properties of a high-entropy TaNbHfZrTi alloy", Journal of Alloys and Compounds 2011, 509, pp. 6043-6048.

[9] S. Y. Chen, Y. Tong, K.-K. Tseng, J. W. Yeh, D. Poplawsky, J. G. Wen, M. C. Gao, G. Kim, W. Chen, Y. Ren, R. Feng, W. D. Li, and P. K. Liaw, "Phase transformations of HfNbTaTiZr high-entropy alloy at intermediate temperatures", Scripta Materialia, 2019, 158, pp. 50-56.

[10] M. Feuerbacher, M. Heidelmann, and C. Thomas, "Hexagonal High-entropy Alloys", Materials Research Letters, 2014, 3(1), pp. 1-6.

[11] L. Lilensten, J. P. Couzinié, L. Perrière, J. Bourgon, N. Emery, and I. Guillot, "TaNbHfZrTi New structure in refractory high-entropy alloys", Materials Letters, 2014, 132, pp. 123-125.

[12] K. M. Youssef, A. J. Zaddach, C. Niu, D. L. Irving, and C. C. Koch, "A novel low-density, high-hardness, high-entropy alloy with close-packed single-phase nanocrystalline structures", Materials Research Letters, 2014, 3(2), pp. 95-99.

[13] M. C. Gao, B. Zhang, S. M. Guo, J. W. Qiao and J. A. Hawk, "High-Entropy Alloys in Hexagonal Close-Packed Structure", Metallurgical and Materials Transactions A, 2015, 47(7), pp. 3322-3332.

[14] O. N. Senkov, J. M. Scott, F. Meisenkothen, S. V. Senkova, D. B. Miracle, and C. F. Woodward, "Microstructure and elevated temperature properties of a refractory TaNbHfZrTi alloy", J Mater Sci, 2012, 47, pp. 4062-4074

[15] G. Dirras, J. Gubicza, A. Heczel, L. Lilensten, J. P. Couzinié, L. Perrière, I. Guillot and A. Hocini, "Microstructural investigation of plastically deformed Ti20Zr20Hf20Nb20Ta20 high entropy alloy by X-ray diffraction and transmission electron microscopy", Materials Characterization, 2015, 108, pp. 1-7.

[16] O. N. Senkov and S. L. Semiatin, "Microstructure and properties of a refractory high-entropy alloy after cold working", Journal of Alloys and Compounds, 2015, 649, pp. 1110-1123.

[17] G. Dirras, L. Lilensten, P. Djemia, M. Laurent-Brocq, D. Tingaud, J. P. Couzinié, L. Perrière, T. Chauveau and I. Guillot, "Elastic and plastic properties of as-cast equimolar TiHfZrTaNb high-entropy alloy", Materials Science and Engineering: A, 2016, 654, pp. 30-38.

[18] C.-C. Juan, M.-H. Tsai, C.-W. Tsai, W.-L. Hsu, C.-M. Lin, S.-K. Chen, S.-J. Lin and J.-W. Yeh, "Simultaneously increasing the strength and ductility of a refractory high-entropy alloy via grain refining", Materials Letters, 2016, 184, pp. 200-203.,

[19] L. Lilensten, J.-P. Couzinié, J. Bourgon, L. Perrière, G. Dirras, F. Prima and I. Guillot, "Design and tensile properties of a bcc Ti-rich high-entropy alloy with transformation-induced plasticity", Materials Research Letters, 2016, 5(2), pp. 110-116.

[20] L. Lilensten, J. P. Couzinié, L. Perrière, A. Hocini, C. Keller, G. Dirras and I. Guillot, "Study of a bcc multi-principal element alloy: Tensile and simple shear properties and underlying deformation mechanisms", Acta Materialia, 2017.

[21] B. Schuh, B. Völker, J. Todt, N. Schell, L. Perrière, J. Li, J. P. Couzinié and A. Hohenwarter, "Thermodynamic instability of a nanocrystalline, single-phase TiZrNbHfTa alloy and its impact on the mechanical properties", Acta Materialia, 2018, 142, pp. 201-212.

[22] O. N. Senkov, A. L. Pilchak and S. L. Semiatin, "Effect of Cold Deformation and Annealing on the Microstructure and Tensile Properties of a HfNbTaTiZr Refractory High Entropy Alloy", Metallurgical and Materials Transactions A, 2018, 49(7), pp. 2876-2892.

[23] A. V. Podolskiy, E. D. Tabachnikova, V. V. Voloschuk, V. F. Gorban, N. A. Krapivka and S. A. Firstov, "Mechanical properties and thermally activated plasticity of the Ti30Zr25Hf15Nb20Ta10 high entropy alloy at temperatures 4.2–350 K", Materials Science and Engineering: A, 2018, 710, pp. 136-141.

[24] Z. Wu, H. Bei, G. M. Pharr and E. P. George, "Temperature dependence of the mechanical properties of equiatomic solid solution alloys with face-centered cubic crystal structures". Acta Mater. 2014;81:428-41.

[25] R. Abbaschian, R.E. Reed-Hill, Physical metallurgy principles. fourth ed. Stamford: Cengage Learning; 2008.

[26] E. Poliak, J. Jonas, "Initiation of dynamic recrystallization in constant strain rate hot deformation". ISIJ Int. 2003;43:684-91.

[27] R.A. Mulford, U.F. Kocks, "New observations on the mechanisms of dynamic strain aging and of jerky flow". Acta Metall. 1979;27:1125-34.

[28] Dynamic strain aging, https://en.wikipedia.org/wiki/Dynamic_strain_aging.

[29] R. Madec, B. Devincre, L.P. Kubin, "From Dislocation Junctions to Forest Hardening". Phys Rev Lett. 2002;89:255508.

[30] M.A. Soare, W.A. Curtin, "Solute strengthening of both mobile and forest dislocations: The origin of dynamic strain aging in fcc metals". Acta Mater. 2008;56:4046-61.

[31] A. van den Beukel, "Theory of the effect of dynamic strain aging on mechanical properties". physica status solidi (a). 1975;30:197-206.

[32] K.G. Samuel, S.L. Mannan, P. Rodriguez, "Another manifestation of dynamic strain ageing". J Mater Sci Lett. 1996;15:1697-9.

[33] E. Rizzi, P. Hähner, "On the Portevin–Le Chatelier effect: theoretical modeling and numerical results". Int J Plast. 2004;20:121-65.

[34] P. Hähner, "On the physics of the Portevin-Le Châtelier effect part 1: The statistics of dynamic strain ageing". Mater Sci Eng A. 1996;207:208-15.

[35] G.E. Dieter, D.J. Bacon, Mechanical metallurgy. New York: McGraw-Hill; 1986.

[36] V. Torganchuk, A. Belyakov, R. Kaibyshev, "Effect of rolling temperature on microstructure and mechanical properties of 18%Mn TWIP/TRIP steels". Mater Sci Eng A. 2017;708:110-7.

[37] Christopher J, Choudhary BK. "Kinetics of Uniaxial Tensile Flow and Work Hardening Behavior of Type 316L(N) Austenitic Stainless Steel in the Framework of Two-Internal-Variable Approach". Metall Mater Trans A. 2015;46:674-87.

[38] Keralavarma SM, Bower AF, Curtin WA. "Quantum-to-continuum prediction of ductility loss in aluminium–magnesium alloys due to dynamic strain aging". Nat Commun. 2014;5:4604.

Appendix

Table 3. 1. Parameters and their values used in Eqs. (2) and (3).

Parameter	σ_a (MPa)	C (K)	σ_b (MPa)	$\frac{\omega_0}{b}$	α (K^{-1})
Value	892.8	874.6	334.8	0.74	2.5×10^{-4}

Table 3. 2. Parameters and their values used in Eq. (9) for predicting the forest-hardening effect at all temperatures

Parameter	b (Å)	A (eV/Å)	ξ (m^{-1})	ζ	$\bar{\varepsilon}$	p
Value	2.944	0.60	2×10^{5}	3.9×10^{-3}	0.86	1.38

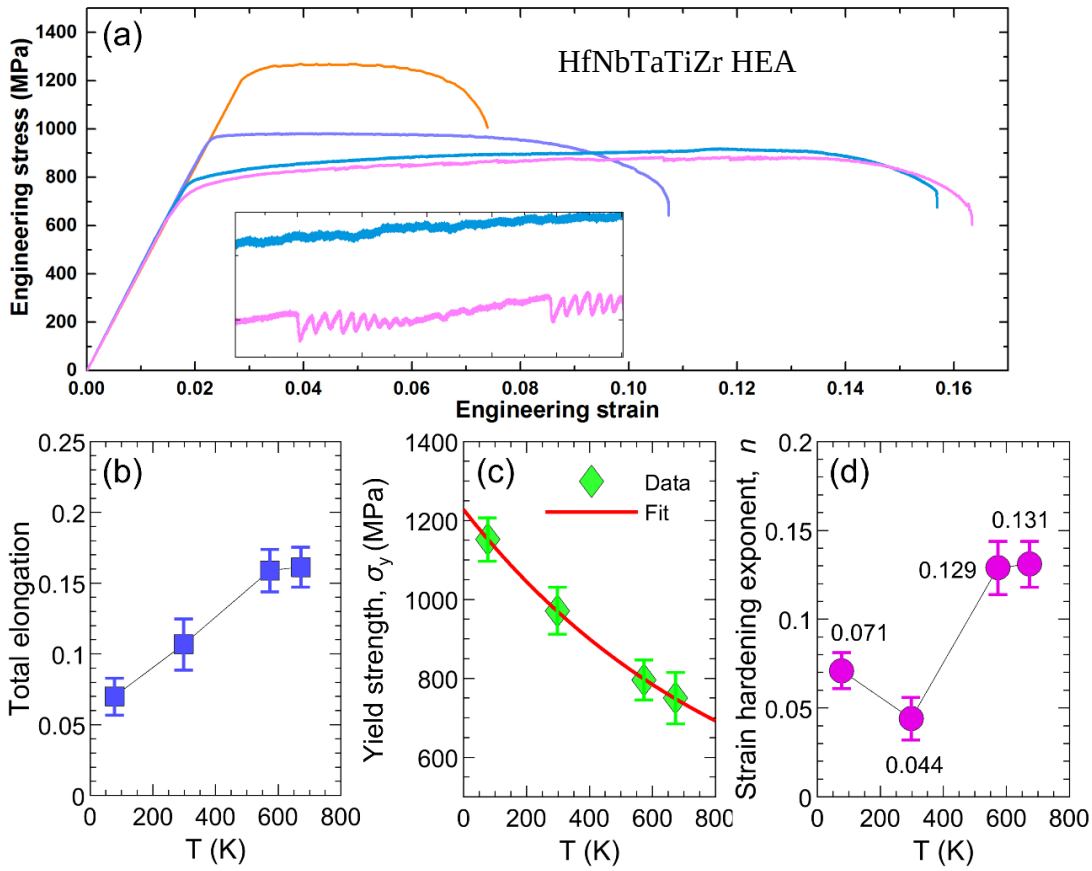

Figure 3. 1. Uniaxial tensile behavior of the BCC HfNbTaTiZr HEAs at 77 – 673 K. (a) Engineering stress – strain curves. (b) Ductility against temperature. (c) Yield strength against temperature. (d) Strain-hardening exponent against temperature.

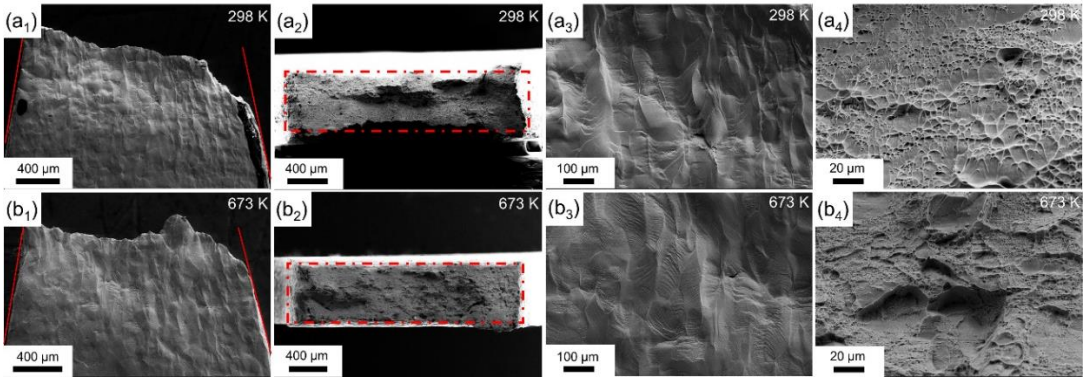

Figure 3. 2. Macroscopic and microscopic fractographs of the tensile HfNbTaTiZr samples failed at (a_{1-4}) 298 K and (b_{1-4}) 673 K.

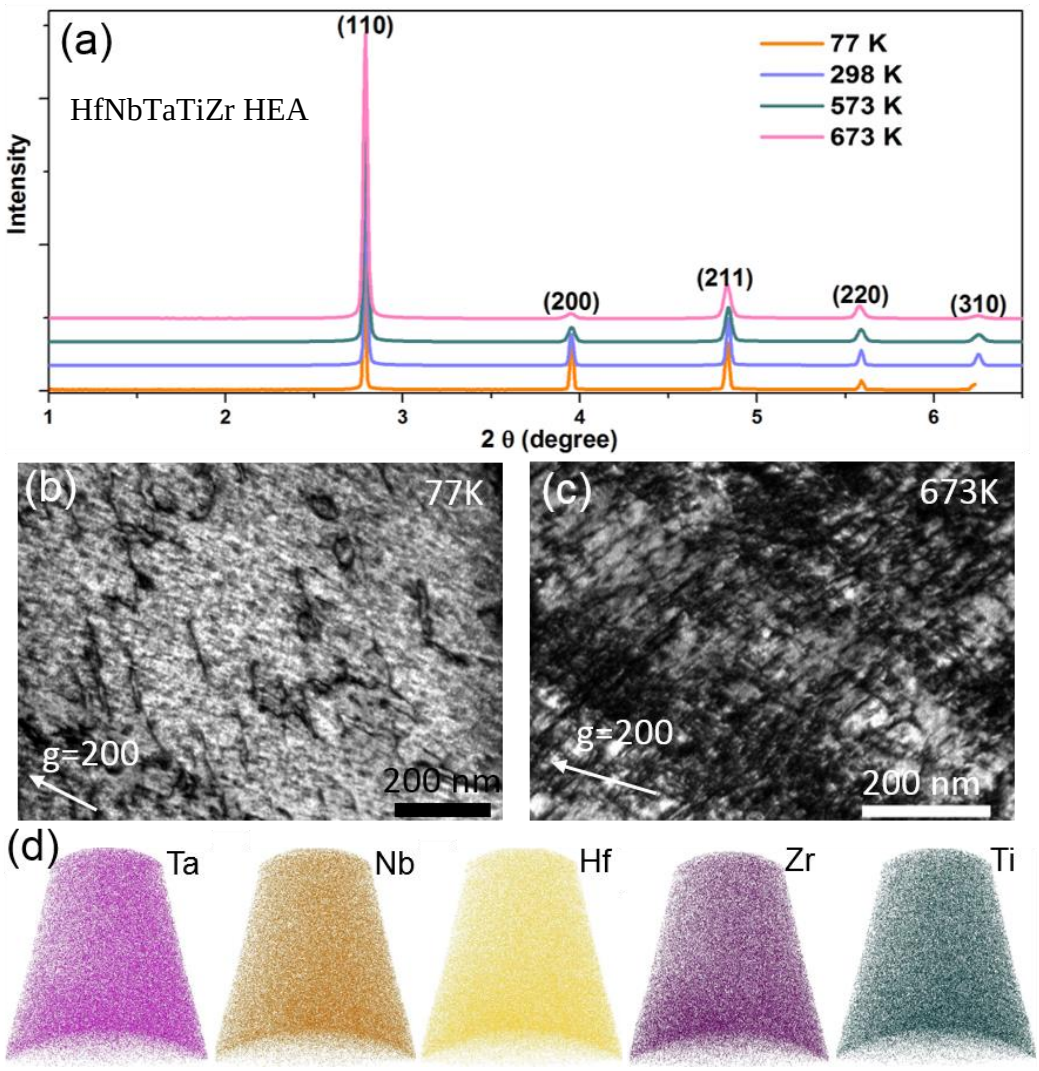

Figure 3. 3. Representative microstructural probing of the HfNbTaTiZr HEA. (a) Synchrotron diffractions of the samples failed at 77 – 673 K. TEM image of the samples failed at (b) 77 K and (c) 673 K. (c) Reconstructed APT tip showing the elemental distribution.

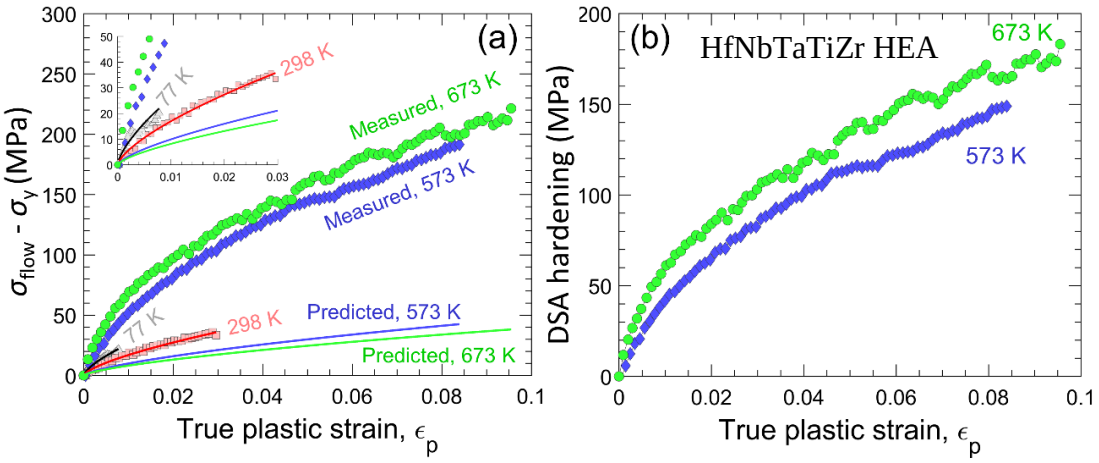

Figure 3. 4. Strain hardening in the HfNbTaTiZr HEA. (a) Strain-hardening portion of the flow stress ($\Delta\sigma = \sigma_{flow} - \sigma_y$) vs. true plastic strain (ε_p) at temperatures from 77 to 673 K. Symbols stand for measurements whereas lines are the predictions by the forest hardening model defined in Eqs. (4) and (9). (b) Estimated DSA hardening for the HEAs at 573 and 673 K

CHAPTER IV PHASE TRANSFORMATIONS OF HFNBTATIZR HIGH-ENTROPY ALLOY AT INTERMEDIATE TEMPERATURES

A version of this chapter was originally published by S. Y. Chen; Peter K Liaw; Yang Tong; K. - K. Tseng; J.- W. Yeh; J. D. Poplawsky; J. G. Wen; M. C. Gao; G. Kim; W. Chen; Y. Ren; R. Feng; W. D. Li in 2018:

S. Y. Chen, Y. Tong, K.-K. Tseng, J.-W. Yeh, D. Poplawsky, J. G. Wen, M. C. Gao, G. Kim, W. Chen, Y. Ren, R. Feng, W. D. Li and P. K. Liaw, "Phase transformations of HfNbTaTiZr high-entropy alloy at intermediate temperatures", Scripta Materialia, 2019, 158, pp. 50–56.

Authors:

S. Y. Chen, Yang Tong, R. Feng, W. D. Li, and Peter K Liaw

Department of Materials Science and Engineering, The University of Tennessee, Knoxville, TN 37996, USA

K. - K. Tseng; J.- W. Yeh

High Entropy Materials Center, Department of Materials Science and Engineering, National Tsing Hua University, Hsinchu 30013, Taiwan

J. D. Poplawsky

Center for Nanophases Materials Sciences, Oak Ridge National Laboratory, Oak Ridge, TN 37831, USA

J. G. Wen

Center for Nanoscale Materials, Argonne National Laboratory, Argonne, IL 60439, USA

M. C. Gao

National Energy Technology Laboratory, Albany, OR 97321, USA

AECOM, P.O. Box 618, South Park, PA 15129, USA

G. Kim and W. Chen

Department of Mechanical, Materials and Aerospace Engineering, Illinois Institute of Technology, Chicago, IL 60616, USA

Y. Ren

X-ray Science Division, Argonne National Laboratory, Argonne, IL 60439, USA

S. Chen's involvement in the article: design experimental procedures, prepared the samples, performed the heat treatment and microstructural characterization, analyzed the experimental data, wrote and revised the article.

Co-researcher's contributions are listed as follow:

Y. Tong, R. Feng and W. Li helped Shuying with the discussion of experimental data and revised the article.

K. Tseng helped Shuying with the fabrication of samples.

J. D. Poplawsky helped Shuying with the atom probe tomograph experiment.

M. C. Gao provide the thermo`analysis

G. Kim and W. Chen provide the analysis on the phase transformation

Y. Ren helped Shuying with the synchrotron diffraction experiment.

J.-W. Yeh and P.K. Liaw provided research guidelines and helped with the data analysis and paper revision.

Abstract

The strong and ductile single-phase body-centered-cubic (BCC) HfNbTaTiZr refractory high-entropy alloy (RHEA) is a potential structural material for high-temperature applications. However, the BCC phase stability in the intermediate temperature range (500–900 °C) needs to be better understood to make this alloy applicable to industry. In the present work, the phase decomposition of the HfNbTaTiZr RHEA is examined at different temperatures (500–1000 °C). Additionally, the formation of BCC Ta-Nb-rich and hexagonal-close-packed (HCP) Hf-Zr-rich precipitates are studied as a function of annealing time at 700 °C using a combination of atom probe tomography, transmission electron microscopy, and X-ray diffraction. We found that these BCC and HCP precipitates have preferred orientations with the BCC matrix.

Refractory high-entropy alloys (RHEAs) have motivated rapidly increasing investigations due to their exceptional high-temperature mechanical properties and great application potential in thermally-harsh environments (e.g., aerospace and power-generation industries) [1-9]. However, a key bottleneck that hinders their real-world applications is the brittleness and poor malleability at low temperatures. It was recently reported that the HfNbTaTiZr RHEA could overcome this hurdle by exhibiting a combination of high strength and good ductility [6, 9]. To promote applications of this alloy at elevated temperatures, maintaining the high phase stability in a broad temperature range during a prolonged service time is crucial to retain its stable structural performance. The HfNbTaTiZr RHEA in the as-cast state as well as after annealing above ~1000°C [6, 9-12] is generally regarded as a single-phase body-centered-cubic (BCC) solid solution

with high stability because of a large contribution of the configurational entropy to the Gibbs free energy. However, contrary to the commonly-expected high-entropy effect that should stabilize the BCC phase at high temperatures, recent investigations by Senkov et al. [9, 10] demonstrated that two BCC phases corresponding to Nb-Ta-rich precipitate and Hf-Zr-rich matrix were formed after annealing a cold-rolled HfNbTaTiZr RHEA at 800 °C for 2 h. Furthermore, they found that the diffusion of Na and Ta may control the precipitate coarsening in the HfNbTaTiZr at 800°C, due to their low self-diffusivities and interdiffusion, compared with that of Ti and Zr [10]. Controversy also exists for the phase stability of the HfNbTaTiZr RHEA at intermediate temperatures of 500 – 900 °C. For example, Stepanov et al. [11] reported the formation of two phases with hexagonal-closed-packed (HCP) and BCC structures after annealing a homogenized HfNbTaTiZr at 800 °C for 100 h. Schuh et al. [12] recently examined the stability of the nanocrystalline HfNbTaTiZr RHEA and reported the formation of three phases (two BCC and one HCP phases) after annealing at 800 °C for 1 h or at 500 °C for 100 h. Moreover, Calphad simulation results suggest that the single phase at high temperatures starts to decompose into three phases when the temperature is below 800C, which is in agreement with the experimental results found in the nanocrystalline HfNbTaTiZr RHEA [12]. Compared with the bulk form, precipitation behavior in the nanocrystalline alloys, however, may behave differently under annealing due to a high fraction of grain boundaries acting as heterogeneous nucleation sites. Aimed to clarify above controversy, the microstructural evolution of the bulk HfNbTaTiZr alloy in the intermediate temperature range was detailed in the present study.

The HfNbTaTiZr buttons were prepared by arc-melting in an argon atmosphere. The solidified buttons were cut into slabs with dimensions of 13.5 mm × 25 mm × 50 mm, and then cold-rolled to a final thickness of 4 mm (a total reduction of ~ 70%) with the imposed per-pass thickness reduction of 0.25 mm. The rolled sheets were then sealed in vacuum-quartz tubes and then homogenized at 1,200 ℃ for 10 min., followed by water quenching. The as-homogenized alloys were subsequently annealed at (550 – 1,000 ℃) for 96 h or at 700 ℃ for 2.5 h, 96 h, and 192 h, respectively.

The crystal structures of the heat-treated samples were examined by synchrotron X-ray diffraction (XRD) with an energy of 111 keV (λ = 0.1173 Å) at the ID-11 Advanced Photon Sources (APS), Argonne National Laboratory (ANL). The diffraction data were collected with a two-dimensional (2D) detector, which was placed about 1,200 mm behind the sample. The 2D diffraction data were processed with the Fit2D software [13]. Besides, the crystal structures of annealed samples were identified by a Panalytical Empyrean X-ray diffractometer with Cu Kα radiation as well. To further investigate the microstructure evolution, several advanced characterization methods were employed, including scanning electron microscopy (SEM) operated in a back-scattered electron (BSE) mode, transmission electron microscopy (TEM) with energy-dispersive X-ray spectroscopy (EDS), and atom probe tomography (APT). The standard bright-field images and selected area diffraction patterns were obtained, using a FEI Talos F200X and the Argonne Chromatic Aberration-corrected TEM (ACAT) at ANL, respectively. An FEI Nova 200 dual-beam focused ion beam (FIB) instrument was used to perform site-specific lift-outs of specimen regions-of-interest (ROI) and annular milling to fabricate the needle-shaped

APT specimens. The APT measurements were performed with a CAMECA Instruments LEAP 4000X HR in a laser mode with a 50 pJ pulse energy at 30 K and a detection rate of 0.005 atoms per pulse. The collected dataset was reconstructed by CAMECA IVAS 3.8 software [14,15].

Figure 4. 1(a) shows that the homogenized specimen has the typical recrystallization microstructure with equiaxed-grains. The corresponding EDS mapping in Figure 4. 1(b-f) reveals a homogeneous distribution of composition in the as-homogenized sample. The phase of the homogenized specimen was verified by synchrotron XRD measurement, shown in Figure 4. 2(a). The homogenized sample has a single BCC phase with a lattice constant of 3.408 Å. Figure 4. 2(a) also presents the synchrotron XRD patterns of the specimens annealed at 550, 700, 900, and 1,000 ℃ for 96 h. For the sample annealed at 1,000 ℃, only a single BCC phase was found. When annealed at 900 ℃, the BCC phase becomes unstable by showing peak splitting. Multiple phases were observed at 550 and 700 ℃, which were confirmed as two BCC phases and one HCP phase, consistent with the previous phase diagram calculation results [12]. Specifically, several minor peaks corresponding to the BCC matrix disappear when the specimen annealed at 550 ℃, compared with that at 700 ℃. The phases present after annealing experiments at various temperatures are summarized in Table 4. 1. Figure 4. 2(b) shows the synchrotron XRD patterns of specimens annealed at the specific temperature of 700 ℃ for 2.5 h, 96 h, and 192 h. The specimen annealed at 700 ℃ for 2.5 h has a major BCC phase and another minor BCC phase (confirmed as Ta-Nb-rich BCC phase later). After annealing at 700 ℃ for 96 and 192 h, three phases are formed, identified as two major BCC phases and one minor

HCP phase. The two BCC phases have a lattice parameter of 3.447 Å (denoted as BCC1) and 3.323 Å (denoted as BCC2), respectively. The lattice parameters of the HCP phase are: a = 3.143 Å and c = 5.042 Å. The microstructures of the samples annealed at 700 ℃ for 2.5, 96 and 192 h were shown in Figure 4. 2(c-h). After the short annealing time of 2.5 h, precipitates with an irregular morphology formed along the grain boundaries, with the volume fraction of about 3.23%. After annealing at 700 ℃ for 96 h [Figure 4. 2(e, f)], precipitates with a lamellar shape were formed along grain boundaries and meanwhile round-shape precipitates were developed within grains, with increasing total volume fraction of about 41.2%. With increasing the annealing time to 8 192 h [Figure 4. 2(g, h)], precipitate coarsening occurs within the grains, while a morphology change of the precipitates at grain boundaries from the lamellar to spherical shapes occurs due to a reduction of the total interface energy. The total volume fraction of precipitates is about 39.8%.

Figure 4. 3(a-g) shows a bright-field (BF) scanning transmission electron microscopy (STEM) image of the sample annealed at 700 ℃ for 96 h and its corresponding elemental-distribution maps obtained by STEM-EDS. The TEM image of the microstructure is taken from a grain interior containing precipitates. Consistent with the XRD results, the elemental maps reveal three phases: the Ta-Nb-rich phase found in the area denoted as N1 in Figure 4. 3(a) and (g), the Hf-Zr-rich phase indicated as the N2 area, and the phase with almost evenly-distributed elements in the area denoted as N3. The compositions of the three multi-element phases based on the TEM-EDS analysis are summarized in the "TEM" row of Table 4. 2. The SEM-EDS analysis (not shown) is unable

to tell the compositional difference due to the phase size being smaller than 1 μm. Figure 4. 3(h-k) show the APT atom maps and proximity histograms of the Ta-Nb-rich and Hf-Zr-rich phases. For the sample annealed at 700 ℃ for 2.5 h, the XRD result suggests a major BCC phase with a small amount of Ta-Nb-rich and Hf-Zr-rich precipitates, which was observed in the compositional analysis by APT [Figure 4. 3(h)]. The sample annealed at 700 ℃ for 96 h presents three phases with different elemental compositions, which was further characterized by APT as well [Figure 4. 3(i)]. The tip sample was taken from the grain-boundary (GB) region. The analyzed APT area was close to a GB. The elemental-concentration profiles generated from an iso-concentration surface (proximity histograms) between the Ta-Nb-rich and Hf-Zr-rich precipitates presented in Figure 4. 3(h, i) are exhibited in Figure 4. 3(j, k). The compositional analysis of the sample annealed for 96 h is listed as the "APT" row in Table 4. 2. It should be noticed that there are some compositional differences for the Ta-Nb-rich and Hf-Zr-rich phases between TEM-EDS and APT results, which might be due to the inherent composition difference from solidification at grain boundaries and grain interiors. This trend does not influence the phase transformation in the present study. The corresponding compositions for each phase obtained from APT are summarized in Table 4. 2 as well.

Selected area electron diffraction (SAED) was performed to obtain the information regarding the crystal structure of each phase in Figure 4. 3 (a). Figure 4. 4(a) and 4(b) show the SAED patterns of N1 together with the matrix, N3. Both the Ta-Nb-rich phase (N1) and the matrix (N3) have a BCC crystal structure but with different lattice parameters. Moreover, two sets of diffraction spots, as indicated by the red arrow along the [111] and

[100] zone axes, suggest that the Ta-Nb-rich precipitate has an orientation similar to the BCC matrix but with a slight tilt due to the lattice mismatch. The SAED patterns of the N2 area along the zone axes of $[011\bar{1}]$ and $[2\bar{1}\bar{1}0]$ are shown in Figure 4. 4(c, d), confirming a Hf-Zr-rich HCP phase. Figure 4. 4 (e, f) present the mixed diffraction patterns of the HCP phase and the BCC matrix. The crystallographic-orientation relationship between this HCP phase and the matrix is revealed as $\{0001\}_{hcp}//\{1\bar{1}0\}_{BCC}$ and $[2\bar{1}\bar{1}0]_{HCP}//[111]_{BCC}$, a classical Burgers orientation relationship (OR) [16].

The equilibrium mole fraction of stable phases as a function of temperature for the HfNbTaTiZr RHEA was calculated in [12], which predicts the formation of a single BCC solid-solution phase in a temperature range from 1,020 to 1,200 °C. At 1,020 °C, another BCC phase enriched with Nb and Ta starts to precipitate, and an HCP phase mainly consisting of Hf, Ti, and Zr starts to form at 800 °C [12]. In other words, below 1,020 °C, the single BCC phase is no longer thermodynamically stable and begins to decompose into a multi-phase structure. At 700 °C, the database predicts co-existing Ta-Nb-rich BCC and Hf-Zr-rich HCP phases. However, some disagreements exist between the CALPHAD calculations [12] and the present experiments at 550 and 700 °C. Calculations [12] predict that two phases co-exist at 550 and 700 °C. But the annealing experiment at 550 °C for 96 h presents that three phases co-exist and annealing at 700 °C for 96 h shows the formation of the HCP phase in a minor fraction. Note that the annealing time may be too short to reach the equilibrium state. In fact, Figure 4. 2(a) shows that the diffraction peaks from the residual BCC matrix at 550 °C become weak with only one major peak existing in the

diffraction pattern. The calculation predicts very well for Ta, Ti, and Zr contents in the BCC phase and Ta, Nb, Zr, and Hf contents in the HCP phase, compared with experiments (Table 4. 2), but the Nb and Hf contents in the BCC phase and Ti content in the HCP phase do not match the experimental result in both phases.

Even though most of the published literatures found a single BCC structure after the homogenization at high temperatures, the HfNbTaTiZr alloy exhibits phase decomposition when annealed in the intermediate temperature range [6, 9-12]. It is known that the Nb and Ta elements possess a stable BCC structure in a wide range of temperatures, while Ti, Zr, and Hf manifest an HCP structure at low temperatures but a BCC structure at high temperatures [17]. To explain the anomalous phase decomposition in the HfNbTaTiZr alloys upon the post-heat treatment, the crystal structure of the constituent metal and the binary diagrams formed by the alloy's constituents should be considered. As suggested by the Ta-Nb phase diagram, a solid-solution alloy forms for all concentrations and maintains a BCC structure at both low and high temperatures, but the HCP structure is the low-temperature stable phase for Hf, Zr, and Ti, and their binary phase diagrams show a BCC-to-HCP phase transformation above a certain temperature. Thus, it is highly possible that an extra HCP phase is formed in the single-phase HfNbTaTiZr RHEA during the post-heat treatment process. Furthermore, in a recent study [12] of the annealing effect on the nanocrystalline HfNbTaTiZr RHEA made by high-pressure torsion, three phases were detected and confirmed as BCC1, BCC2, and HCP structure by synchrotron XRD. However, it is not the case in the present work. The decomposition found in the current work, which occurs during the annealing process at 700 ℃, is from the as-quenched state

obtained by water quenching after homogenizing at 1,200 °C. This trend means that the effect of the cold-worked structure on free energies of different phases and thus the equilibrium state could be avoided in the present work. Therefore, the present experimental design could clearly reveal the evolution and the approach to the equilibrium state during annealing without the cold-worked structure effect.

The phase stability of the as-cast HEAs is often predicted, based on some widely-adopted empirical parameters, including the mixing enthalpy (ΔH_{mix}), mixing entropy (ΔS_{mix}), and atomic-size misfit (δ %) [18]. The empirical criteria for the formation of a single-phase BCC HEA are -15 kJ/mol < ΔH_{mix}< 5 kJ/mol [19], valence electron concentration (VEC) < 6.87, and 1% < δ < 6% [18, 20]. Table 4. 3 lists the VEC and atomic size for each composing element [21], and Table 4. 4 presents the mixing enthalpy of all possible atomic pairs among the five constituents [22]. For the HfNbTaTiZr RHEA, VEC = 4.4, δ = 4%, and ΔH_{mix} = 2.72 kJ/mol meet the criteria, which is consistent with the single-phase formation in the high-temperature range. However, this prediction is essentially for the phase equilibrium at high temperatures close to the melting point, where the mixing-entropy effect could be fully utilized to enhance the formation of solid solutions.

As for the phase decomposition in the sample annealed at 700 ℃, it can be thermodynamically explained with the decreased high-entropy effect, since some other factors would become significant, as compared to the decreased high-entropy effect at lower temperatures. In fact, the three criteria mentioned above relate with the chemical bonding, crystal-structure tendency, and atomic-size difference, respectively, and affect the

Gibbs free energy. From the basic relation, $\Delta G_{mix} = \Delta H_{mix} - T\Delta S_{mix}$, for each kind of structure, ΔH_{mix} is actually the chemical-bonding-energy change, ΔH_{chem}, plus the strain-energy-induced ΔH_{strain}. So the "ΔH_{mix}" in the criteria is ΔH_{chem}, and "VEC" and "δ" relate with ΔH_{strain} [18]. As these three factors basically do not change with temperature, its influence on the free energy for different temperatures can be regarded to be small, which means that the mixing entropy effect becomes the main factor as the temperature is a multiplier of entropy in the ΔG_{mix} equation. Under this condition, the free energy of the fully-random solid solution of the equiatomic composition is raised, relative to other non-equiatomic compositions when temperature is lowered.

In conclusion, the crystal structure and microstructure of the homogenized HfNbTaTiZr alloy after annealing at different temperatures (550 °C, 700 °C, 900 °C and 1000 °C) for 96 h or at 700 °C for 2.5 h, 96 h, and 192 h are systematically investigated. The TEM study of crystal structure and composition reveals that the HfNbTaTiZr RHEA decomposes into three phases, the BCC matrix, BCC Ta-Nb-rich and HCP Zr-Hf-rich precipitates when annealing at 700 °C even after a short-period of annealing time, 2.5 h. SEAD study further unveils that both the BCC and HCP precipitates have preferred orientations with the BCC matrix, the orientation of the BCC precipitates similar to the matrix but with a slight tilt due to large lattice mismatch and a orientation relationship between the matrix and the HCP as $\{0001\}_{hcp} // \{1\bar{1}0\}_{BCC}$ and $[2\bar{1}\bar{1}0]_{HCP} // [111]_{BCC}$.

References

[1] O. N. Senkov, S. V. Senkov, C. Woodward, and D. B. Miracle, "Low-density, refractory multi-principal element alloys of the Cr–Nb–Ti–V–Zr system: microstructure and phase analysis", Acta Materialia 61(2012) 1545-1557.

[2] S.-P. Wang and J. Xu, "TiZrNbTaMo high-entropy alloy designed for orthopedic implants: as-cast microstructure and mechanical properties", Materials Science and Engineering: C 73(2016) 80-89.

[3] Y. Zhang, T. T. Zuo, Z. Tang, M. C. Gao, K. A. Dahmen, P. K. Liaw and Z. P. Lu, "Microstructures and properties of high-entropy", Progress in Materials Science 61(2014) 93.

[4] D. B. Miracle and O. N. Senkov, "A critical review of high entropy alloys and related concepts", Acta Materialia 122(2017) 448-511.

[5] Y. Zhang, Y. Liu, Y. Li, X. Chen, and H. Zhang, "Microstructure and mechanical properties of a refractory HfNbTiVSi0.5 high-entropy alloy composite", Materials Letters 174(2016) 82-85.

[6] O. N. Senkov, J. M. Scott, F. Meisenkothen, S. V. Senkova, D. B. Miracle, and C. F. Woodward, "Microstructure and elevated temperature properties of a refractory HfNbTaTiZr alloy", Journal of Materials Science 47(2012) 4062-4074.

[7] S. Vrtnik, P. Koželj, A. Meden, S. Maiti, W. Steurer, M. Feuerbacher, and J. Dolinšek, "Superconductivity in thermally annealed Ta-Nb-Hf-Zr-Ti high-entropy alloys', Journal of Alloys and Compounds 695(2016) 3530-3540.

[8] A. D. Pogrebnjak, I. V. Yakushchenko, O. V. Bondar, O. V. Sobol, V. M. Beresnev, K. Oyoshi, H. Amekura and Y. Takeda, “The microstructure of a multielement nanostructured (TiZrHfVNbTa)N coating and its resistance to irradiation with Au–ions”, Technical Physics Letters 41(2015) 1054-1057.

[9] O. N. Senkov and S. L. Semiatin, “Microstructure and properties of a refractory high-entropy alloy after cold working”, Journal of Alloys and Compounds 649(2015) 1110-1123.

[10] O. N. Senkov, A. L. Pilchak and S. L. Semiatin, "Effect of Cold Deformation and Annealing on the Microstructure and Tensile Properties of a HfNbTaTiZr Refractory High Entropy Alloy", Metallurgical and Materials Transactions A, 2018, 49(7), pp. 2876-2892.

[11] N. D. Stepanov, N. Y. Yurchenko, S. V. Zherebtsov, M. A. Tikhonovsky and G. A. Salishchev, “Aging behavior of the HfNbTaTiZr high entropy alloy”, Materials Letters 211(2017) 87-90.

[12] B. Schuh, B. Völker, J. Todt, N. Schell, L. Perrière, J. Li, J. P. Couzinié and A. Hohenwarter, “Thermodynamic instability of a nanocrystalline, single-phase TiZrNbHfTa alloy and its impact on the mechanical properties”, Acta Materialia 142(2018) 201-212.

[13] A.P. Hammersley, S.O. Svensson, A. Thompson, H. Graafsma, Å. Kvick, J.P. Moy, “Calibration and correction of distortions in 2D detector systems”, Review of Scientific Instruments, (SRI-94) 66(1995) 2729-2733.

[14] W. Guo, D. A. Garfinkel, J. D. Tucker, D. Haley, G. A. Young, and J. D. Poplawsky. “An atom probe perspective on phase separation and precipitation in duplex stainless steels”, Nanotechnology 27(2016) 254004.

[15] K. Thompson, D. Lawrence, D.J. Larson, J.D. Olson, T.F. Kelly, and B. Gorman, “In situ site-specific specimen preparation for atom probe tomography”, Ultramicroscopy 107(2007) 131-139.

[16] W.G. Burgers, "On the process of transition of the cubic-body-centered modification into the hexagonal-close-packed modification of zirconium”, Physica 1(1934) 561-586.

[17] H. Okamoto: Desk Handbook: Phase Diagrams for Binary Alloys, ASM International, Materials Park, OH, 2000.

[18] Y. Zhang, Y. J. Zhou, J. P. Lin, G. L. Chen, and P. K. Liaw, “Solid-solution phase formation rules for multi-component alloys”, Advanced Engineering Materials 10(2007) 534-538.

[19] J.- W. Yeh, “Physical Metallurgy of High-Entropy Alloys”, JOM 67(2015) 2254-2261.

[20] S. Guo, C. Ng, J. Lu, and C. T. Liu, “Effect of valence electron concentration on stability of fcc or bcc phase in high entropy alloys”, Journal of Applied Physics 109(2011) 103505.

[21] S. Guo and C. T. Liu, “Phase stability in high entropy alloys: Formation of solid-solution phase or amorphous phase”, Progress in Natural Science: Materials International 21(2011) 433-446.

[22] A. Takeuchi and A. Inoue, “Classification of bulk metallic glasses by atomic size difference, heat of mixing and period of constituent elements and its application to characterization of the main alloying element”, Materials Transactions 46(2006) 2817-2829.

Appendix

Table 4. 1. The phase formation in samples annealed in the temperature range of 550 – 1,000 ℃

Temperatures (℃)	550	700	900	1,000	As-homogenized
Phases	TaNb BCC + minor matrix BCC + HfZr HCP	TaNb BCC + matrix BCC + HfZr HCP	Minor TaNb BCC + matrix BCC	matrix BCC	matrix BCC

Table 4. 2. The compositions of each phase in the sample annealed at 700 ℃ for 96 h

Phase		Ta (at. %)	Nb (at. %)	Ti (at. %)	Zr (at. %)	Hf (at. %)
Ta-Nb-rich BCC	TEM-EDX	42.81	29.67	15.27	5.32	6.93
	APT	38.52	33.44	17.46	4.05	6.53
	CALPHAD	40.95	40.57	12.22	3.54	2.73
Hf-Zr-rich HCP	TEM-EDX	7.62	0.75	10.43	43.99	37.21
	APT	5.87	0.39	9.31	49.04	35.39
	CALPHAD	0.57	0.92	27.21	35.27	36.02
Matrix BCC	TEM-EDX	21.10	13.37	22.09	20.28	23.16
	APT	20.53	21.10	20.10	19.50	18.77

Note

TEM-EDX: data was collected in the grain interior; APT: data was collected at the location close to the grain boundary

Table 4. 3. The atomic size and VEC of composing elements

Element	Ta	Nb	Ti	Zr	Hf
Atomic size (Å)	1.430	1.429	1.462	1.603	1.578
VEC	5	5	4	4	4

Table 4. 4. The mixing enthalpies (kJ/mol) between composing elements

	Nb	Ti	Hf	Zr
Ta	0	1	3	3
Nb	0	2	4	4
Ti	-	0	0	0
Hf	-	-	0	0
Zr	-	-	-	0

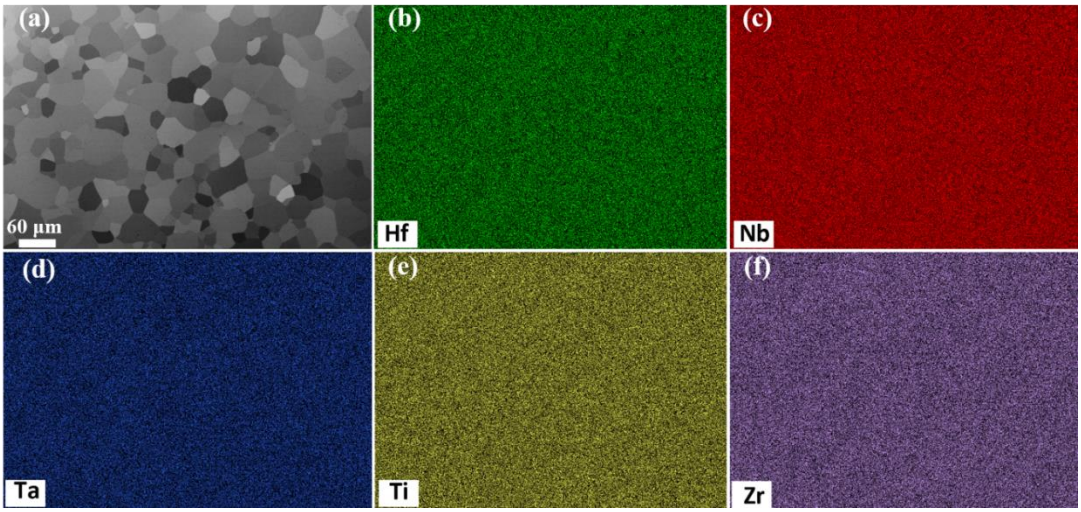

Figure 4. 1. SEM image (a) and the corresponding EDX maps (b-f) of as-homogenized specimen.

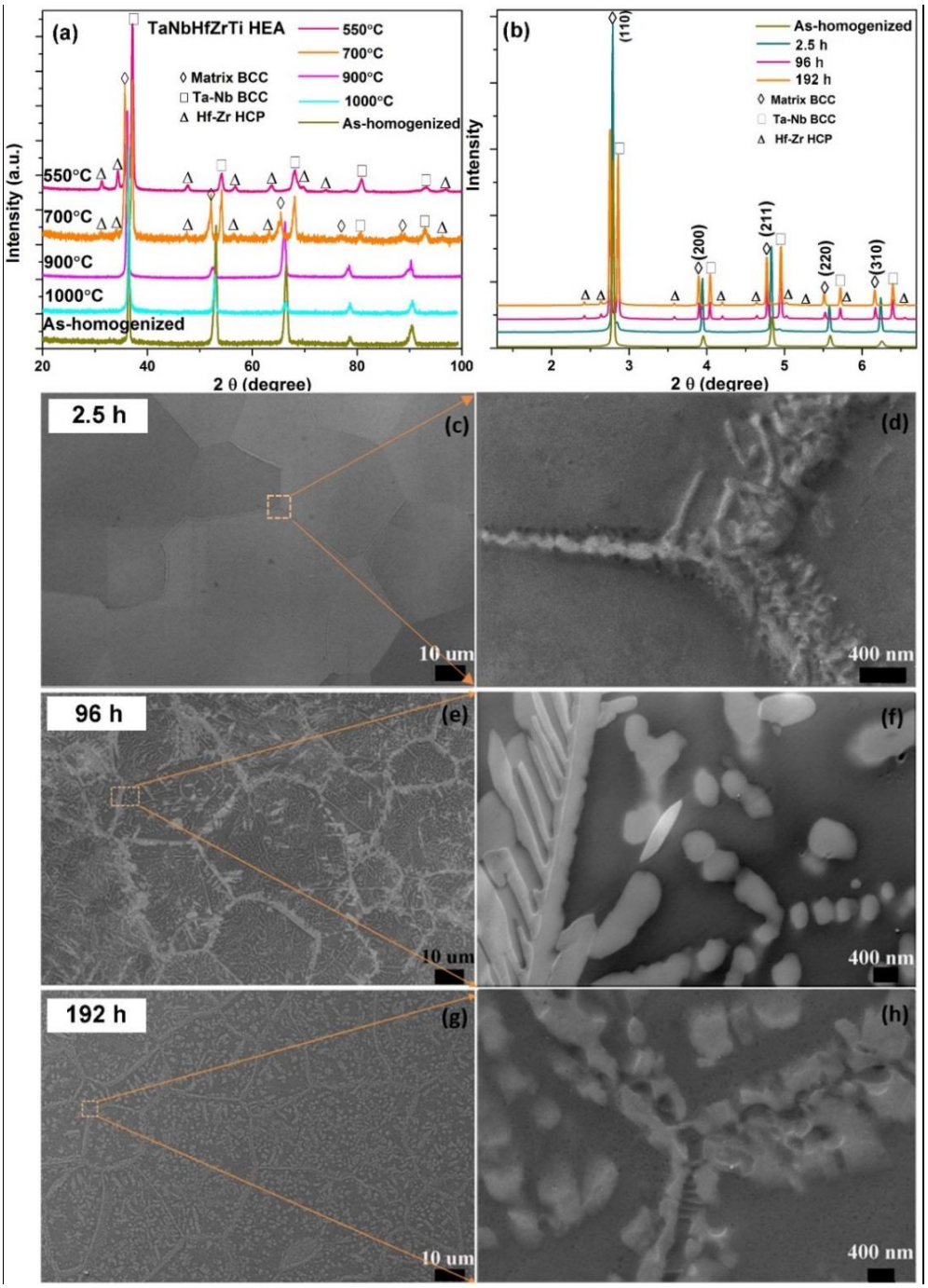

Figure 4. 2. Synchrotron XRD patterns of specimens annealed at different temperatures for 96 h (a) and annealed at the temperature of 700 °C for 2.5 h, 96 and 192 h (b). The synchrotron XRD pattern from as-homogenized sample is also included; (c-h) SEM images of specimens annealed at 700 °C for 2.5 h (c, d), 96 h (e, f) and 192 h (g, h).

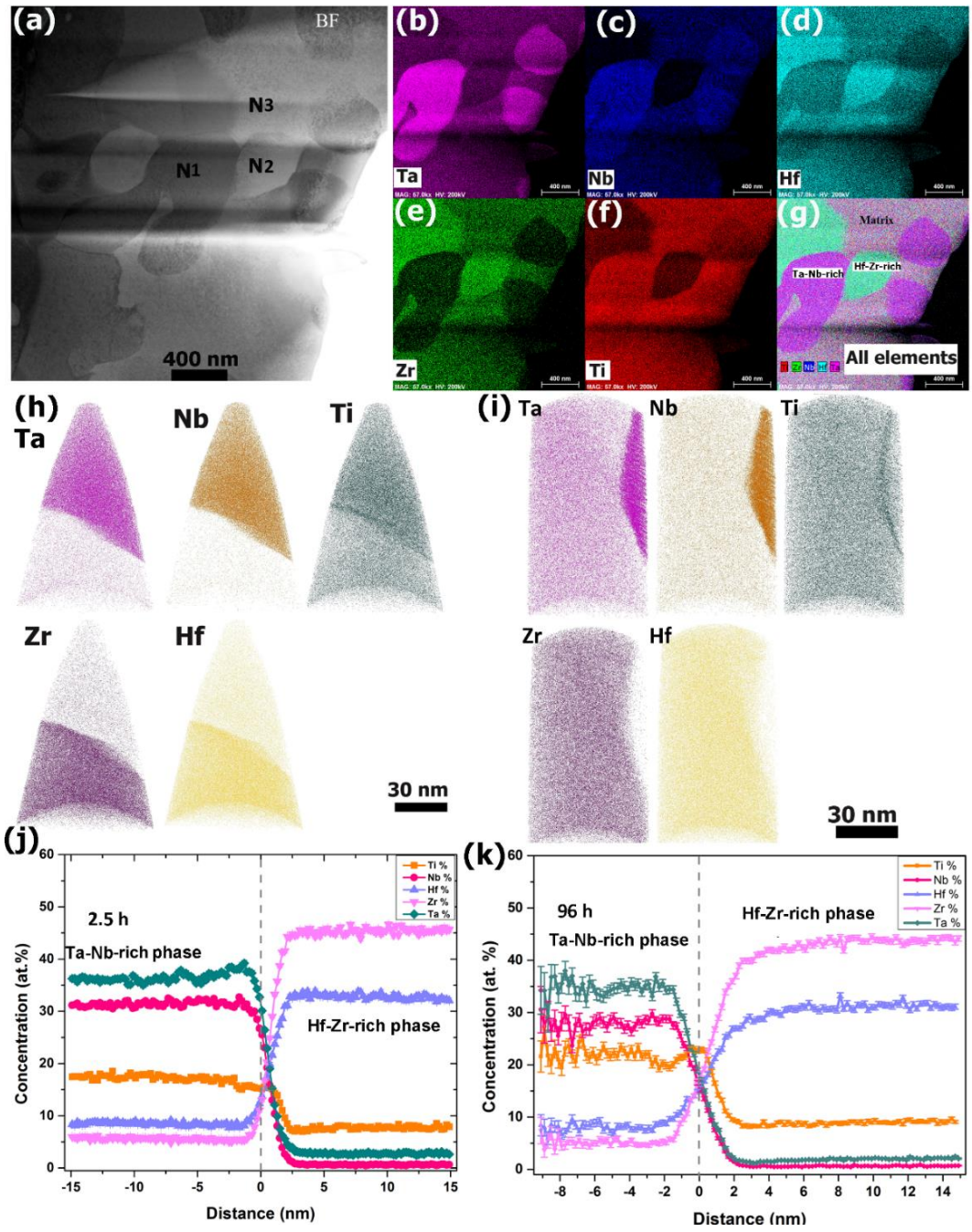

Figure 4. 3. (a) Bright-field (BF) TEM image of the specimen after aging at 700 °C for 96 h; the corresponding elemental-distribution maps (b-f) and overall map (g) obtained by STEM-EDS; atom maps of samples annealed for 2.5 h (h) and 96 h (i) reconstructed from the APT analysis; proximity histograms of concentration profiles of samples annealed for 2.5 h (j) and 96 h (k).

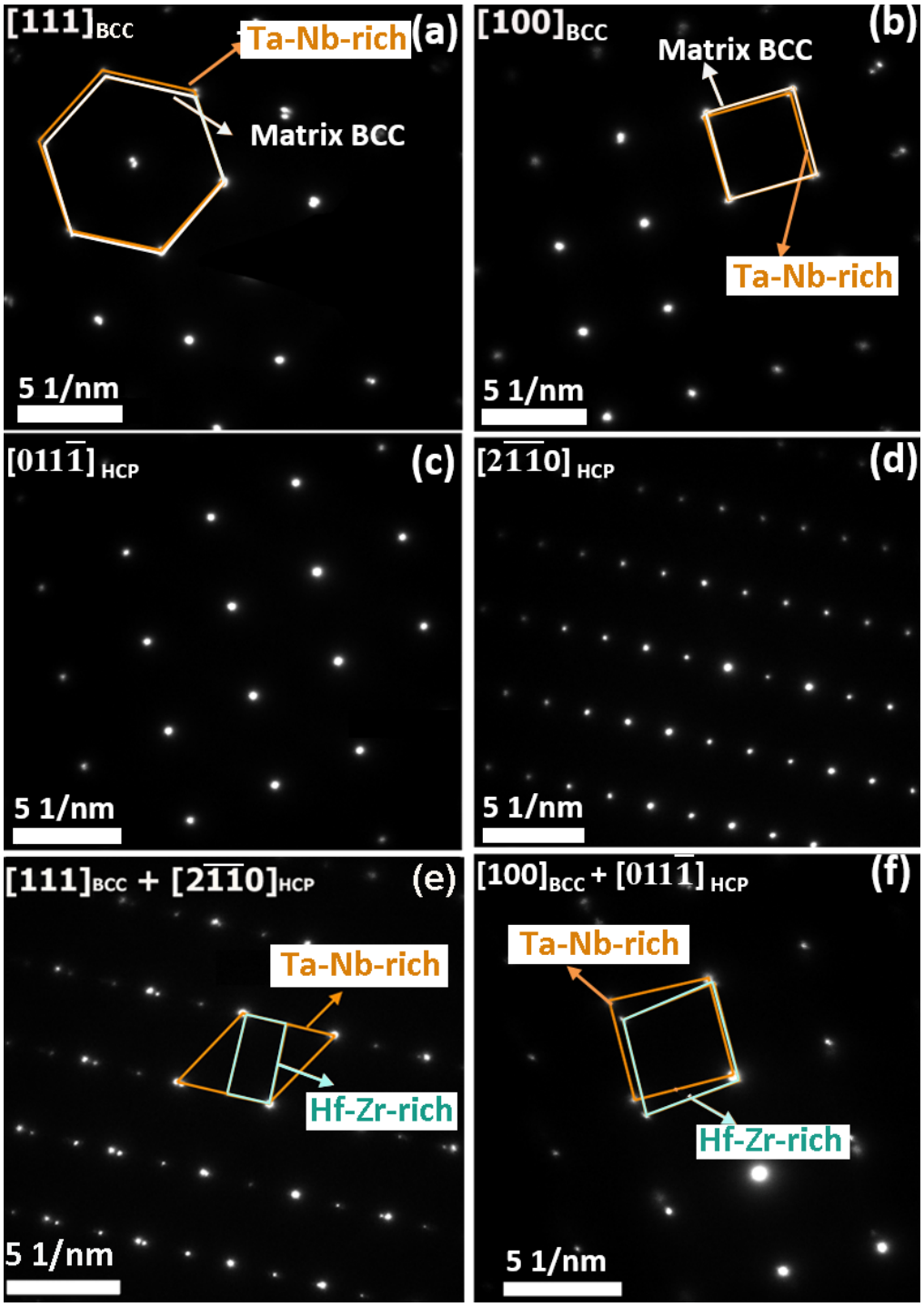

Figure 4. 4. SAED patterns from both BCC1 and BCC2 phases taken along the [111] (a) and [100] (b) zone axes (ZA) of the matrix; SAED patterns from the HCP phase taken from the [0111̄] (a) and [2112̄0] (b) ZAs; SAED patterns from both BCC1 and HCP phases taken along the [111] (a) and [100] (b) ZAs of the matrix.

CHAPTER V THE FATIGUE BEHAVIOR IN HFNBTAZRTI REFRACTORY HIGH-ENTROPY ALLOYS

This article will be submitted to Materials Research Letters.

Authors:

S.Y. Chen, L. Wang, K.-K. Tseng and J.-W. Yeh, W.D. Li, Yang Tong, Tao Yuan, Y. Ren, and P.K. Liaw

Department of Materials Science and Engineering, The University of Tennessee, Knoxville, TN 37996, USA

K.-K. Tseng and J.-W. Yeh

Department of Materials Science and Engineering, National Tsing Hua University, Hsinchu, 30013, Taiwan

Department of Industrial and Systems Engineering, Ohio University, Athens, OH 45701, USA

Y. Ren

X-ray Science Division, Argonne National Laboratory, Argonne, IL 60439, USA

Abstract

The HfNbTaTiZr high-entropy alloys (HEAs) with single BCC structure were tested under the four-point bending experiment. The S-N curve of cyclic life provide a superior fatigue properties with endurance limit of 512.5 MPa and fatigue ratio of 0.42, which is comparable and may outperform many conventional alloys. From the microstructure and dislocation substructure analysis under scanning electron microscope (SEM) and transmission electron microscope (TEM), the excellent properties were explained in terms of followings: 1) the delay of crack propagation by the closure and crack branch which could release the stress concentration caused by the local inhomogeneous deformation; 2) the dislocation network, which could hinder the movement of mobile dislocations, further improving the fatigue properties. In addition, the statistical model as well was applied in current study to predict the average fatigue life, which will be helpful for the material design and optimization.

5.1 Introduction

A novel design concept, high-entropy alloys (HEAs), proposed by Yeh [1], have been widely investigated and developed during last decade, due to their unique structures, compositions and attractive properties. Specifically, HEAs consist of at least three principal elements with equiatomic or near-equiatomic percentage, and they tend to form single solid-solution such as body-centered-cubic (BCC), face-centered cubic (FCC), and hexagonal-closed packed structure (HCP) [2-11]. They were characterized by four core effect, including high mixing entropy, lattice distortion, sluggish diffusion, and cocktail effect due to their unique multiple-element mixtures [12]. Up to date, various HEA systems have been developed, and present many promising properties, including high strength [13], outstanding wear, corrosion resistance, as well as good oxidation resistance [14-16], excellent cryogenic and elevated temperature properties [17], which make them potential candidates for nuclear, turbine, and aerospace application. However, the cyclic fatigue resistance in HEAs are rarely investigated, which is crucial for structural component in-service alloys subjecting to a non-monotonic loading. Only several articles introduced the fatigue properties in HEAs. Specifically, the cyclic loading and lifetime prediction have been firstly studied in the $Al_{0.5}$CoCrCuFeNi FCC HEA by Tang and Hemphill [18,19]. Their results have exhibited the impressive fatigue resistance in the Al0.5, compared with that in conventional alloys. Tang et al. [19] have presented that the nanotwin evolution during cyclic loading may cause the working hardening, leading to their higher resistance to crack initiation. The fatigue crack propagation of single phase CrMnFeCoNi HEA have been studied at room temperature and 198K by Thurston et al. [20]. They found that the

crack propagation was dominated by the transgranular fracture at room temperature, while intergranular fracture at cryogenic temperature. The improved fatigue properties in AlCoCrFeNi2.1 with hierarchical microstructure have been investigated by Shukla et al. [21]. They suggest that BCC(B2) precipitate could hinder the path of PSBs formed in FCC(L12) lamellae, which delayed the fatigue initiation in AlCoCrFeNi2.1 HEA. However, the fatigue behavior in HEAs materials with BCC structure have not been investigated to the same extent. Little emphasis appears to have been focused on the fundamental understanding during fatigue testing of BCC materials and thus the state of knowledge is far behind that for FCC materials. Even though BCC structure alloys usually have less slip systems and lower ductility than that in FCC structure, they possess superior mechanical strength, especially in HfNbTaTiZr alloys. As previously studied, the HfNbTaTiZr alloys can be a potential candidate material for elevated -temperature applications [13,22]. The outstanding combination of yield strength and ductility have been obtained when monotonically deformed at room temperature [23-25]. However, its suitability for use in hostile environment, i.e. cyclic loading, is still unknown. It is necessary to carefully examine the resistance of HfNbTaTiZr alloys to fatigue behavior to obtain a comprephensive view of the resistance of this particular material to cyclic loading. Thus, in order to reveal the fatigue response of BCC materials, four-point-bending experiments were conducted in the HfNbTaTiZr alloys with BCC crystal structure to investigate macroscopic rules of the fatigue behaviors and the dislocation substructure occurring in them.

5.2 Experimental procedure

The HfNbTaTiZr alloy was prepared by vacuum arc-melting in a water-cooled copper crucial under an argon atmosphere. The solidified ingots were cut into the dimensions of 13.5 mm × 25 mm × 50 mm. Then, they were cold-rolled by the imposed per-pass thickness reduction of 0.25 mm, and the final thickness is 4 mm by a total reduction of 70%. The rolled sheets were, then, sealed in a vacuum quartz tube. The heat treatment in an air furnace was 1,200 °C for 10 min, and, then, the sheets were quenched in water (this is the condition for samples "after annealing"). The rolled sheets were subsequently machined to fatigue samples with dimensions of 25 x 3 x 3 mm for four-point-bending-fatigue experiments, as described below, i.e., the 25-mm length of the sample ran parallel to the rolling direction. Thus, the applied stress on the tensile edge was parallel to the rolling direction. To remove as many surface defects as possible, the samples were polished on a Buehler rotating grinder and polisher. 400, 600, 800, and 1,200 grits were used in that order. The sample was turned through 90°after each polishing step, finished with the 1,200 grit running parallel along the length direction of the sample.

To study the fatigue behavior of the HEA samples, four-point-bending tests were conducted at various applied loads and run until the failure of the specimen or 10^7 cycles had been reached. The maximum stress, σ, on the tensile surface within the span of the two outer pins in the four-point-bending-fatigue experiment was calculated, using the beam theory relationship [26]

$$\sigma = \frac{3P(S_0 - S_i)}{2BW^2} \quad (1)$$

where P is the applied load, S_0 is the outer span length of 20 mm, S_i is the inner span length of 10 mm, B is the thickness, and W is the height. In this investigation, B = W = 3 mm. The samples were tested as 10 Hz with a loading ratio of $R = \sigma_{min.}/ \sigma_{max.} = 0.1$ [26], where $\sigma_{min.}$ and $\sigma_{max.}$ are the minimum and maximum applied stressed, respectively. In order to investigate the deformation mechanism and evolution of microstructure, the fracture morphology and the surface near the fracture were determined, using SEM equipped with the backscatter-electron (BSE) imaging capability. The surface around the fracture was ground by SiC papers, and, then, polished via a vibration machine to obtain the smooth surface.

The TEM (transmission electron microscopy) samples were prepared via focused ion beam (FIB)lift-out techniques with Ga+ ions at 30 kV and a finishing energy of 5 kV using a Zeiss Crossbeam Auriga FIB-SEM system. TEM examination was performed using a JEOL 2100F TEM/STEM instrument operated at 200 kV.

5.3 Results

Figure 5. 1(a) present the microstructure before the fatigue experiment. Equiaxed grains after the cold rolling and heat treatment could be obtained, with average grain size of 40-50 um. Tensile test is performed at room temperature with strain rate of $1x10^{-3}$ to obtain its yield strength 1190 MPa, ultimate strength (UTS) of 1260 MPa, and ductility of 0.12, as shown in Figure 5. 1(b), which is comparable or even higher than that in the previous reports [25]. Senkov et al. suggest that the solid-solution and grain boundary-strengthening mechanism could be responsible for the excellent yield strength and ductility

in the single phase of HfNbTaTiZr HEA. Based on its tensile results, different stress amplitude [(σ_{max}- σ_{min}) /2] was chosen to conduct the fatigue experiments and the results of the fatigue tests were plotted as a typical stress amplitude vs. number of cycles to failure (S–N) curve, presented in Figure 5. 1(c) to characterize its cyclic loading properties. The S-N curve of HfNbTaTiZr HEA illustrate a general trend, number of cycles decreasing with increasing the stress amplitude. To better reveal the fatigue property in HfNbTaTiZr HEA, the comparison of fatigue ratio (endurance limit of stress amplitude/UTS) with $Al_{0.5}$CoCrCuFeNi HEA is presented in Figure 5. 1(d). It is apparent that the HfNbTaTiZr HEA displays a much higher endurance limit regarding with fatigue ratio, 0.504, than that in $Al_{0.5}$CoCrCuFeNi HEA, 0.27 [19]. Moreover, a small amount of scattering data could be found from the S-N curve. Tang et al. [19] suggest that these scatters could be caused not only by the stress concentration, corrosion, and temperature, but also the microstructural defects, such as oxides, shrinkage pores, preexisting cracks.

Figure 5. 2 presents the microstructural evolution after the cyclic loading to explore the reason of excellent fatigue properties HfNbTaTiZr BCC HEA. Small cracks are tending to initiate at the specimen surface because the cyclic plastic deformation at or near the surface is higher than the interior one due to the reduced constraint of the surface layer [27]. Various toughening microstructures [28], such as zig-zag, crack deflection, crack closure, and crack branch could be observed in the crack path. These features play an important role in enhancing the resistance to crack growth.

Multiple crack branches at certain angle to the main crack are observed along the crack path, which could greatly reduce the stress concentration and crack driving force, thus, energy available for the advancement of main fatigue crack. Generally, crack branches (secondary-cracks) stop their propagation soon after they left the main crack. The crack deflection was observed at the grain boundary and within grains, as indicated in Figure 5. 2(b). A closer look at the crack path suggest that a dual-slip system occur during the crack propagation, as indicated by the red dot line, and these secondary growth in directions at an angle with the main crack plane could further dissipate energy at crack tip as well to increase the resistance to fatigue [29]. The grain misorientation is one of the main factors that affect the crack propagation path. It is suggested that the propagation path may deflect a certain angle when the crack traverse along grain boundary to enter into a new grain or extend with the grain, which could reduce the pile up of dislocations at the front of crack, thus leading to a low stress concentration [30]. Microstructurally-induced crack deflection could increase the resistance against cyclic crack growth and maintain high strength level that provide an improved resistance to crack initiation [31]. Zig-zag feature could be found as well. It is suggested by Gray et al. [32] that the zig-zag feature in the crack path, which increase with grain size, will produce the variation in the surface roughness, further influencing the amount of crack closure. Besides, the crystallographically caused zig-zag could reduce crack growth because of an increased crack length traveled per unit crack advance, i.e. absorbs some energy by increasing crack path tortuosity to release stress concentration, which could enhance their fatigue properties [32].

Figure 5. 3 presents the microstructural evolution of sample deformed at σ_a = 522 MPa. TEM was performed in order to investigate the dislocation arrangement after cyclic loading. During cyclic loading, dislocations arrange themselves into preferred defect structures to minimize the total elastic strain energy of the system [33]. TEM foil was prepared from the primary crack initiation site, which located at the tensile side of specimen and close to the facture surface. A complex dislocation structures were given in Figure 5. 3. The TEM image was obtained under two beam bright field imaging condition with g=[110] in [111] zone axis. Apparent slip bands consisting of thin dislocations, intersect the whole investigated grain. The dislocations structure was inhomogeneous, with some regions showing a less or more dense dislocations. Couple of incipient cells were found during cyclic loading, leading to the fatigue hardening [34]. Some dislocation lines still exist in the interior zones of cells, indicating the uncompleted formation of cells. Deformed substructures varied in networks, dimension, dislocation lines, and arrays in sub-boundaries and different regions. Many dislocation loops were found at the dislocation lines, as indicated by the orange arrows, and at the nodes of network as well (shown in Figure 5. 3(1)). The dislocation jogs or kinks are formed for both dislocation lines and dislocation networks in the process of dislocation movement, as indicated by red arrows.

Moreover, the dislocation arrays were found from the post-fatigue sample as well, located at different regions. To further clarify the formation of these dislocation substructures, a series magnified figures taken from different locations were presented in Figure 5. 3(1-6). The network with quadrangular cells were observed in the area 1 [shown in Figure 5. 3 (1)], with dislocation loops at the node and the slip band intersecting. Two

dislocations periodically form nodes, forming a net. The very similar quadrangular cells were also observed in tungsten single crystal when creeped at elevated temperature [35]. Prevailing dislocation network with high dislocation density could be found at region 2 and 3 with different orientation and are easy to identify, making them a good structure to investigate the effect of different fatigue loads (room temperature) [36]. Specifically, quadrangular cells with regular shape and arrangement were found in the lower part of the figure, and they transform to a more complex network with irregular shape in the upper left part of the figure. Curved dislocation lines were found to intersect these irregular cells to produce more complex network. Additionally, the fine network within large cells was observed in the right region as well, as indicated by the orange dash line. However, in the neighboring region of 3, the regular and well-developed quadrangular cells at right side gradually change to irregular hexagonal cell at left hand side, with dislocation lines passing through. A gradual transition structure exist between these two types of network. Elongated hexagonal cells with regular arrangement were observed in region 4, with quadrangular cells network forming at the right hand side. Such elongated network may be caused by the mutual overlapping of a row of boundary dislocation [35]. A closer look at the end of elongated hexagonal cells exhibit a opening feature without surrounding by the rim. Region 5 present the quadrangular cells with a long curved dislocation line passing through them, without interaction. Region 6 provides another type of dislocation network with low dislocation density and large cell size, composing of kinked or jogged dislocation along the observable line length, indicated by the red arrows. They cannot be simply defined as quadrangular or hexagonal network because of the kinks and jogs existence.

The dislocation structure of foil taken at primary crack initiation of sample deformed at σ_a = 585 MPa was presented in Figure 5. 4 for comparison. The TEM image was obtained under two beam bright field imaging condition with g=[$\bar{1}0\bar{1}$] in [111] zone axis. It exhibit typical slip bands with high dislocation density. Few dislocations were found between slip bands. Highly tangled dislocations in a disorganized manner (shown in the magnified figure of b and c), and dislocation loops were produced during cyclic loading in the Figure 5. 4(d), which indicate that slip irreversibility plays a strong tole in the deformation process in current alloy [37]. The formation of slip bands present that the localized cyclic plastic deformation into the bands with a higher slip activity than the surrounding matrix occurs when the present existing dislocation structure cannot accommodate further cyclic plastic deformation under the given condition. These bands would provide preferential sites for crack initiation and crack propagation along these bands would also be easier [27]. No apparent dislocation network was found in this foil.

5.4 Discussion

The analyses of crack propagation and fracture surface morphology indicate that a number of extrinsic toughening mechanisms are also available in the HfNbTaZrTi HEA to shield the crack tip, causing increased resistance to fatigue crack propagation.

In principle, fatigue crack extension in a material is driven by the globally applied stress intensity range $\Delta K = K_{\max} - K_{\min}$, where $K_{\max}$ and $K_{\min}$ are the maximum and minimum applied stress intensities derivable from the maximum and minimum applied stresses $\sigma_{\max}$ and $\sigma_{\min}$ [38]. For idealized mode I crack propagation without any crack tip

shielding, the global characterizing parameter ΔK can neatly quantify the driving force of fatigue crack growth [38]. Nevertheless, once extrinsic toughening presents, the local driving force experienced at the crack tip turns to differ from the global ΔK. In fact, extrinsic shielding causes an extra stress intensity K_{s}, which negatively contributes to the global driving force ΔK to result in a reduced near-tip stress intensity range, i.e., $\Delta K_{\mathrm{tip}} = \Delta K - K_{\mathrm{s}}$. Since the fatigue crack growth rate $\frac{\mathrm{d}a}{\mathrm{d}N}$ has a power law dependence on the stress intensity range ΔK according to the Paris law $\frac{\mathrm{d}a}{\mathrm{d}N} = C\Delta K^m$, where C and m are constants [38], the reduction of ΔK to ΔK_{tip} at the crack tip by any form of extrinsic toughening is expected to significantly decelerate the fatigue crack growth rate $\frac{\mathrm{d}a}{\mathrm{d}N}$. For the HEA under investigation, all four extrinsic toughening mechanism identified are anticipated to retard fatigue crack extension, though in distinct manners,.

A series of change in the dislocation structures occurs during cyclic plastic deformation, and the cyclic stable structure shown in Figure 5. 3 consist of dislocations arranged in clearly defined network. Typically, similar dislocation network are usually observed in the creep or fatigue at elevated temperatures, which go extensive cross slip such as nickel-based superalloys [27, 35, 39-50], and rarely found in the specimens deformed at room temperature. It is proposed that the dislocation network is resulting from the interaction between the matrix dislocations or between the dislocation and precipitates. Since there is no precipitates existence in current alloys, the only way for dislocation network formation should be the matrix dislocations. Thus, the dislocation reaction tends

to take place with different slip systems when the dislocation density increase in the matrix with the deformation proceeding.

On the one hand, dislocation networks are reposted to be relatively stable and can accommodate certain amount of cyclic plastic deformation to minimize the total strain energy [39]. On the other hand, the formed networks can hinder the movement of the dislocations during the deformation, which may improve the cyclic hardening of material [27]. As mentioned above, two types of network were found in the fatigued specimen, quadrangular and hexagonal network. Specifically, the hexagonal network was formed by the interaction between two sets of moving dislocations in the same plane with different Burgers vector. However, quadrangular networks were formed by two groups of dislocations without reaction between them because they moved on different slip planes. In terms of the Frank's rule, the formation of dislocation network is energetically favorable. It should be noted that during cyclic loading the development of a dislocation structure and its quantitative characteristics was independent on the crystallographic orientation of the compression axis [35]. However, not all the crossing dislocation segments can react to form third-type segments, as indicated by yellow arrow in Figure 5. 3, the dislocation line that traverse the dislocation network but failed to react and form new network, even though they were not orthogonal dislocation lines [51]. Thus, it is acceptable that at the crack tip or a growing crack, the dislocation tend to rearrange into low energy dislocation configurations, including hexagonal or quadrangular cell.

Generally speaking, the dislocation in BCC materials can start to move when the lattice friction resistance is overcome by applied stress. When a gliding dislocation encounters forest dislocations along its path where it can be held back as the unsupported part of the dislocation bows out and result in intersection, leading to dislocation jogs [41]. Except the BCC materials, dislocation network was observed in the compression experiment at high temperature or room temperature in HCP titanium, Ti-6Al-4V alloys and Zircaloy-4 alloys as well. It was found that the formed dislocation networks during the deformation can hinder the motion of dislocation and promote cross slip [36, 50]. Link et al. investigated the dislocation network formed through the self-organization process in nickel based superalloys, which is related to the dislocation types at different creep stage, but is consistent with the mentioned mechanism, reaction between two sets of dislocations moving in same crystal plane [43]. When dislocations are activated in the matrix and start to react with the network, their reaction may change the direction of the original moving dislocation, which will promote the climbing of dislocations and delay the occurrence of the stress concentration. In one word, the dislocation networks appear to be a sessile dislocation substructure which can provide strengthening by affecting the strength of the sub-grain boundaries and by interacting with mobile dislocations. The formation of dislocation network may release the stress concentration to delay the crack initiation and propagation, thus enhancing the resistance to cyclic loading. [46, 48].

The Weibull predictive model presented in Hemphill *et al*. [18] was adopted to model and analyze the experimental data. The Weibull predictive model is built based on two assumptions [18].

We, first, assume that at each fixed stress range, S, the fatigue life, $N(S)$, follows the Weibull distribution with a shape parameter, β, and a scale parameter, $\alpha(S)$. The scale parameter is assumed to be stress dependent. Then, the fatigue-failure probability by $N(S)$ cycles at the stress range, S, is predicted by the Weibull cumulative distribution function (CDF) given by Equation (2),

$$F(N(S)\,|\,\alpha(S),\beta) = 1 - \exp\left(-\left(\frac{N(S)}{\alpha(S)}\right)^{\beta}\right). \tag{2}$$

We, next, assume a log-linear life-stress relationship for the Weibull scale parameter, $\alpha(S)$, given by

$$\log(\alpha(S)) = \gamma_0 + \gamma_1 \log(S), \tag{3}$$

where γ_0 and γ_1 are, respectively, the intercept and slope. Given the experimental *S-N* data, the maximum likelihood method presented by Hemphill *et al*. [18] can be used to estimate the unknown model parameters, γ_0, γ_1, and β. Once the model parameters are estimated, the fatigue-life characteristics at a stress range, S, can be predicted by estimating the p-quantile life given by Equation (4)

$$N_p(S) = \exp(\gamma_0 + \gamma_1 \log(S))(-\log(1-p))^{1/\beta}. \tag{4}$$

The median fatigue life with p = 0.5 can be used to describe the relationship between the applied stress and the average fatigue life. The 0.025 and 0.975 quantiles can be used to construct a 95% predictive interval for the fatigue life to quantify the scatter in the fatigue life.

The maximum likelihood estimates of the model parameters, γ_0, γ_1, and β, were found to be 76.6811, -45.5433, and 0.4575, respectively. Figure 5. 5 shows the predicted

median, 0.025 quantile, and 0.975 quantile fatigue lives. The predicted median-life curve can reasonably describe the average life-stress trend. The 0.025 and 0.975 quantile-life curves form the 95% predictive intervals for the fatigue life. The 95% predictive interval covers all the observed data points. The fatigue-endurance limits can be estimated from Equation (4) by finding the stress range corresponding to the 10^7 cycles. The estimated the median fatigue-endurance limit was found to be 503.06 MPa with a 95% confidence interval of (429.18 MPa, 545.09 MPa).

Comparisons with conventional fatigue-resistant materials of stress amplitude vs. cycles to failure, shown in Figure 5. 6(a), present the HEAs with a lower-bound endurance limit comparable with the 15–5PH stainless steel and Ti-6Al-4V, and an upper bound only surpassed by some bulk-metallic glasses (BMGs). The HEAs illustrate a much higher endurance limit than the conventional alloys and BMGs. Specifically, the HfNbTaTiZr HEA present the highest endurance limit compared with other HEAs, i.e., eutectic $AlCoCrFeNi_{2.1}$ HEA [21], $Al_{0.3}CoCrFeNi$ ultrafine grained triplex HEA [54], and $Al_{0.5}CoCrCuFeNi$ HEAs [18, 19]. To better compare the fatigue performance of the HEAs with other structural counterparts with respect to their UTS, the fatigue ratios (defined as the ratio of the fatigue-endurance limit, based on the stress amplitude, to the UTS) are used and shown in Figure 5. 6(b). The lower bound of the fatigue ratios of the HEAs compares favorably with those of steels, Ti-alloys, and Ni-alloys. Moreover, for some materials, such as ultra-high strength steels and wrought aluminum alloys, their high tensile strengths result in lower fatigue ratios due to their brittle nature. the HfNbTaTiZr HEA present much higher fatigue ratio except the $Al_{0.3}CoCrFeNi$ ultrafine grained triplex HEA, suggesting that the

fatigue properties in HEAs could be improved by material processing and optimizing microstructure. It is apparent that the upper bound of the fatigue ratio of HEAs is remarkably higher than those of other conventional structural counterparts and even BMGs [Figure 5. 6(b)], which suggest that it is potential for these materials to be replaced by HEAs in structural applications with improved fabrication and processing.

5.5 Conclusions

HfNbTaTiZr HEA with single BCC structure are investigated in four-point bending experiments and superior fatigue properties were presented from S-N curve, compared with the reported results. The microstructure after fatigue experiments exhibits interesting features such as zig-zag, crack branch, crack closure, and crack deflection, which are important to enhance the fatigue behaviors. Additionally, the dislocation network was formed by the interaction between dislocations with different Burgers vectors, which can act as the obstacle to dislocation motion to strengthen the fatigue behavior and release the strain energy and stress concentration to improve the resistance to cyclic loading.

References

[1] J.-W. Yeh, Advanced Engineering Materials, 2004, 6(5), pp. 299-303.

[2] W. Guo, W. Dmowski , J.-Y. Noh, P. Rack, P. K. Liaw and T. Egami, "Local atomic structure of a high-entropy alloy: an X-ray and neutron scattering study", Metallurgical and Materials Transactions A 2012, 44A, pp. 4, p. 1994.

[3] S. Maiti and W. Steurer, "Structural-disorder and its effect on mechanical properties in single-phase TaNbHfZr high-entropy alloy", Acta Materialia, 2016, 106, pp. 87-97.

[4] S. Y. Chen, X. Yang, K. Dahmen, P. Liaw and Y. Zhang, "Microstructures and Crackling Noise of AlxNbTiMoV High Entropy Alloys", Entropy, 2014, 16(2), pp. 870-884.

[5] C.-J. Tong, Y.-L. Chen, S.-K. Chen, J.-W. Yeh, T.-T. Shun, C.-H. Tsau, S.-J. Lin and S.-Y. Chang, "Microstructure Characterization of AlxCoCrCuFeNi High-Entropy Alloy System with Multiprincipal Elements", Metall. Mater. Trans. A, 2005, 36A, pp. 881-893.

[6] Y. Zhang, T. T. Zuo, Z. Tang, M. C. Gao, K. A. Dahmen, P. K. Liaw and Z. P. Lu, "Microstructures and properties of high-entropy", Progress in Materials Science, 2014, 61, pp. 93, p. 1.

[7] S. Y. Chen, X. Xie, B. L. Chen, J. W. Qiao, Y. Zhang, Y. Ren, K. A. Dahmen and P. K. Liaw, "Effects of temperature on serrated flows of Al0.5CoCrCuFeNi high-entropy alloy", Jom, 2015, 67(10), pp. 2314-2320.

[8] S. Chen, L. Yu, J. Ren, X. Xie, X. Li, Y. Xu, G. Zhao, P. Li, F. Yang, Y. Ren and P. K. Liaw, "Self-Similar Random Process and Chaotic Behavior In Serrated Flow of High Entropy Alloys", Scientific reports, 2016, 6, pp. 29798.

[9] Y. Zhang, Y. J. Zhou, J. P. Lin, G. L. Chen and P. K. Liaw, "Solid-solution phase formation rules for multi-component alloys", Advanced Engineering Materials, 2007, 10, pp. 534-538.

[10] S. Chen, X. Xie, W. Li, R. Feng, B. Chen, J. Qiao, Y. Ren, Y. Zhang, K. A. Dahmen and P. K. Liaw, "Temperature effects on the serrated behavior of an Al 0.5 CoCrCuFeNi high-entropy alloy", Materials Chemistry and Physics, 2017.

[11] S. Chen, W. Li, X. Xie, J. Brechtl, B. Chen, P. Li, G. Zhao, F. Yang, J. Qiao, K. A. Dahmen and P. K. Liaw, "Nanoscale serration and creep characteristics of Al 0.5 CoCrCuFeNi high-entropy alloys", Journal of Alloys and Compounds, 2018, 752, pp. 464-475.

[12] J.-W. Yeh, "Physical Metallurgy of High-Entropy Alloys", Jom, 2015, 67(10), pp. 2254-2261.

[13] O. N. Senkov, J. M. Scott, S. V. Senkova, D. B. Miracle and C. F. Woodward, "Microstructure and room temperature properties of a high-entropy TaNbHfZrTi alloy", Journal of Alloys and Compounds 2011, 509, pp. 6043–6048.

[14] X.-W. Qiu, Y.-P. Zhang, L. He and C.-g. Liu, "Microstructure and corrosion resistance of AlCrFeCuCo high entropy alloy", Journal of Alloys and Compounds, 2013, 549, pp. 195-199.

[15] Y. Shi, B. Yang, X. Xie, J. Brechtl, K. A. Dahmen and P. K. Liaw, "Corrosion of $Al_xCoCrFeNi$ high-entropy alloys: Al-content and potential scan-rate dependent pitting behavior", Corrosion Science, 2017, 119, pp. 33-45.

[16] A. Raphel, S. Kumaran, K. V. Kumar and L. Varghese, "Oxidation and Corrosion resistance of AlCoCrFeTiHigh Entropy Alloy", Materials Today: Proceedings, 2017, 4(2), pp. 195-202.

[17] S. Yoshida, Scripta Materialia, 2017, 134, pp. 33-36.

[18] M. A. Hemphill, T. Yuan, G. Y. Wang, J. W. Yeh, C. W. Tsai, A. Chuang and P. K. Liaw, "Fatigue behavior of Al0.5CoCrCuFeNi high entropy alloys", Acta Materialia, 2012, 60(16), pp. 5723-5734.

[19] Z. Tang, T. Yuan, C.-W. Tsai, J.-W. Yeh, C. D. Lundin and P. K. Liaw, "Fatigue behavior of a wrought Al0.5CoCrCuFeNi two-phase high-entropy alloy", Acta Materialia, 2015, 99, pp. 247-258.

[20] K. V. S. Thurston, B. Gludovatz, A. Hohenwarter, G. Laplanche, E. P. George and R. O. Ritchie, "Effect of temperature on the fatigue-crack growth behavior of the high-entropy alloy CrMnFeCoNi", Intermetallics, 2017, 88, pp. 65-72.

[21] S. Shukla, T. Wang, S. Cotton and R. S. Mishra, "Hierarchical microstructure for improved fatigue properties in a eutectic high entropy alloy", Scripta Materialia, 2018, 156, pp. 105-109.

[22] O. N. Senkov, J. M. Scott, F. Meisenkothen, S. V. Senkova, D. B. Miracle and C. F. Woodward, "Microstructure and elevated temperature properties of a refractory TaNbHfZrTi alloy", J Mater Sci, 2012, 47, pp. 4062-4074

[23] O. N. Senkov and S. L. Semiatin, "Microstructure and properties of a refractory high-entropy alloy after cold working", Journal of Alloys and Compounds, 2015, 649, pp. 1110-1123.

[24] B. Schuh, B. Völker, J. Todt, N. Schell, L. Perrière, J. Li, J. P. Couzinié and A. Hohenwarter, "Thermodynamic instability of a nanocrystalline, single-phase TiZrNbHfTa alloy and its impact on the mechanical properties", Acta Materialia, 2018, 142, pp. 201-212.

[25] O. N. Senkov, A. L. Pilchak and S. L. Semiatin, "Effect of Cold Deformation and Annealing on the Microstructure and Tensile Properties of a HfNbTaTiZr Refractory High Entropy Alloy", Metallurgical and Materials Transactions A, 2018, 49(7), pp. 2876-2892.

[26] K. M. Flores, W. L. Johnson, R. H. Dauskardt, Scripta Materialia 2003;49:1181.

[27] Y. Liu, J. J. Yu, Y. Xu, X. F. Sun, H. R. Guan and Z. Q. Hu, "High cycle fatigue behavior of a single crystal superalloy at elevated temperatures", Materials Science and Engineering: A, 2007, 454-455, pp. 357-366

[28] M. Mehrali, E. Moghaddam, S. F. Seyed Shirazi, S. Baradaran, M. Mehrali, S. T. Latibari, H. S. Metselaar, N. A. Kadri, K. Zandi and N. A. Osman, "Mechanical and in vitro biological performance of graphene nanoplatelets reinforced calcium silicate composite", PLoS One, 2014, 9(9), pp. e106802.

[29] G. Nicoletto, R. Konecna and A. Pirondi, "Fatigue crack paths in coarse-grained magnesium", Fracture of Engineering Materials and Structures, 2005, 28(1-2), pp. 237-244.

[30] H. Jian, F. Jiang, L. Wei, X. Zheng and K. Wen, "Crystallographic mechanism for crack propagation in the T7451 Al–Zn–Mg–Cu alloy", Materials Science and Engineering: A, 2010, 527(21-22), pp. 5879-5882.

[31] S. Suresh, "Fatigue crack deflection and fracture surface contact Micromechanical models", Metallurgical Transactions A, 1985, 16A, pp. 249-260.

[32] G.T. Gray, J.C. Williams and A. W. Thompson, Metallurgical Transactions A, 1983(14A), pp. 421-433. 2. M. Mehrali, PLoS One, 2014, 9(9), pp. e106802

[33] M. D. Sangid, H. J. Maier and H. Sehitoglu, "A physically based fatigue model for prediction of crack initiation from persistent slip bands in polycrystals", Acta Materialia, 2011, 59(1), pp. 328-341.

[34] J.H. Zhang, Z.Q. Hu, Y.B. Xu and Z. G. Wang, "Dislocation Structure in a Single-Crystal Nickel-Base Superalloy during Low Cycle Fatigue", Metallurgical Transactions A, 1992, 23A, pp. 1253-1258.

[35] M. M. Myshlyaev, Y. A. Romanov, O. N. Senkov, I. I. Khodos and V. G. Glebovskii, "High-temperature creep and the dislocation structure of tungsten single crystals", Institute of Solid Physics, 1979, 5, pp. 26-34.

[36] P. O. Tympel, T. C. Lindley, E. A. Saunders, M. Dixon and D. Dye, "Influence of complex LCF and dwell load regimes on fatigue of Ti–6Al–4V", Acta Materialia, 2016, 103, pp. 77-88.

[37] V. Sinha, C. Mercer and W. O. Soboyejo, "An investigation of short and long fatigue crack growth behavior of Ti–6Al–4V", Materials Science and Engineering A, 2000, 287, pp. 30–42.

[38] S. Suresh, Fatigue of materials: Cambridge university press; 1998.

[39] Stephen D. Antolovich, Paul omas and J. L. Strudel, "Low Cycle Fatigue of Rene 80 as Affected by Prior Exposure", Metallurgical Transactions A, 1979, 10A, pp. 1859-1878.

[40] S. Kraft, and H. Muchrab, "Aspects of high-temperature low-cycle thermomechanical fatigue of a single crystal nickel-base superalloy", Fatigue Fract. Engng Mater. Struci. , 1993, 16(2), pp. 231-253.

[41] E. P. Busso and F. A. McClintock, "A dislocation mechanics-based crystallographic model of a B2-type intermetallic alloy", International Journal of Plasticity, 1996, 12, No.(1), pp. 1-28.

[42] T. Sugui, Z. Huihua, J. Zhang, H. Yang, Y. Xu and Z. Hu, "Formation and role of dislocation networks during high temperature creep of a single crystal nickel–base superalloy", Materials Science and Engineering A, 2000, 279 pp. 160–165.

[43] T. Link, A. Epishin, M. Klaus, U. Brückner and A. Reznicek, "〈100〉 Dislocations in nickel-base superalloys: Formation and role in creep deformation", Materials Science and Engineering: A, 2005, 405(1-2), pp. 254-265.

[44] X. Wang, M. Jahazi and S. Yue, "Substructure of high temperature compressed titanium alloy IMI 834", Materials Science and Engineering: A, 2006, 434(1-2), pp. 188-193.

[45] C. Stöcker, M. Zimmermann, H. J. Christ, Z. L. Zhan, C. Cornet, L. G. Zhao, M. C. Hardy and J. Tong, "Microstructural characterisation and constitutive behaviour

of alloy RR1000 under fatigue and creep–fatigue loading conditions", Materials Science and Engineering: A, 2009, 518(1-2), pp. 27-34.

[46] J. Yu, X. Sun, T. Jin, N. Zhao, H. Guan and Z. Hu, "High temperature creep and low cycle fatigue of a nickel-base superalloy", Materials Science and Engineering: A, 2010, 527(9), pp. 2379-2389.

[47] P. Li, Q. Q. Li, T. Jin, Y. Z. Zhou, J. G. Li, X. F. Sun and Z. F. Zhang, "Comparison of low-cycle fatigue behaviors between two nickel-based single-crystal superalloys", International Journal of Fatigue, 2014, 63, pp. 137-144.

[48] J. Xie, S. Tian, L. J. Shang and X. Zhou, "Creep behaviors and role of dislocation network in a powder metallurgy Ni-based superalloy during medium-temperature", Materials Science and Engineering: A, 2014, 606, pp. 304-312.

[49] I. S. Kim, "Effect of microstructural characteristics on the low cycle fatigue behaviors of cast Ni-base superalloys", Materials Characterization, 2015, 106, pp. 375-381.

[50] B. Kombaiah and K. L. Murty, "Dislocation cross-slip controlled creep in Zircaloy-4 at high stresses", Materials Science and Engineering: A, 2015, 623, pp. 114-123.

[51] H. Zhang, C. Zhang, T. Hu, X. Zhan, X. Wang and Y. Zhou, "On the small angle twist sub-grain boundaries in Ti3AlC2", Scientific reports, 2016, 6, pp. 23943.

[52] X. Wang, P. Vo, M. Jahazi and S. Yue, "Dwell Fatigue Microstructure in a Near-α Titanium Alloy", Metallurgical and Materials Transactions A, 2007, 38(4), pp. 831-839.

[53] G. Kang, Y. Dong, Y. Liu and H. Jiang, "Macroscopic and microscopic investigations on uniaxial ratchetting of two-phase Ti–6Al–4V alloy", Materials Characterization, 2014, 92, pp. 26-35.

[54] K. Liu, M. Komarasamy, B. Gwalani, S. Shukla and R. S. Mishra, "Fatigue behavior of ultrafine grained triplex Al0.3CoCrFeNi high entropy alloy", Scripta Materialia, 2019, 158, pp. 116-120.

Appendix

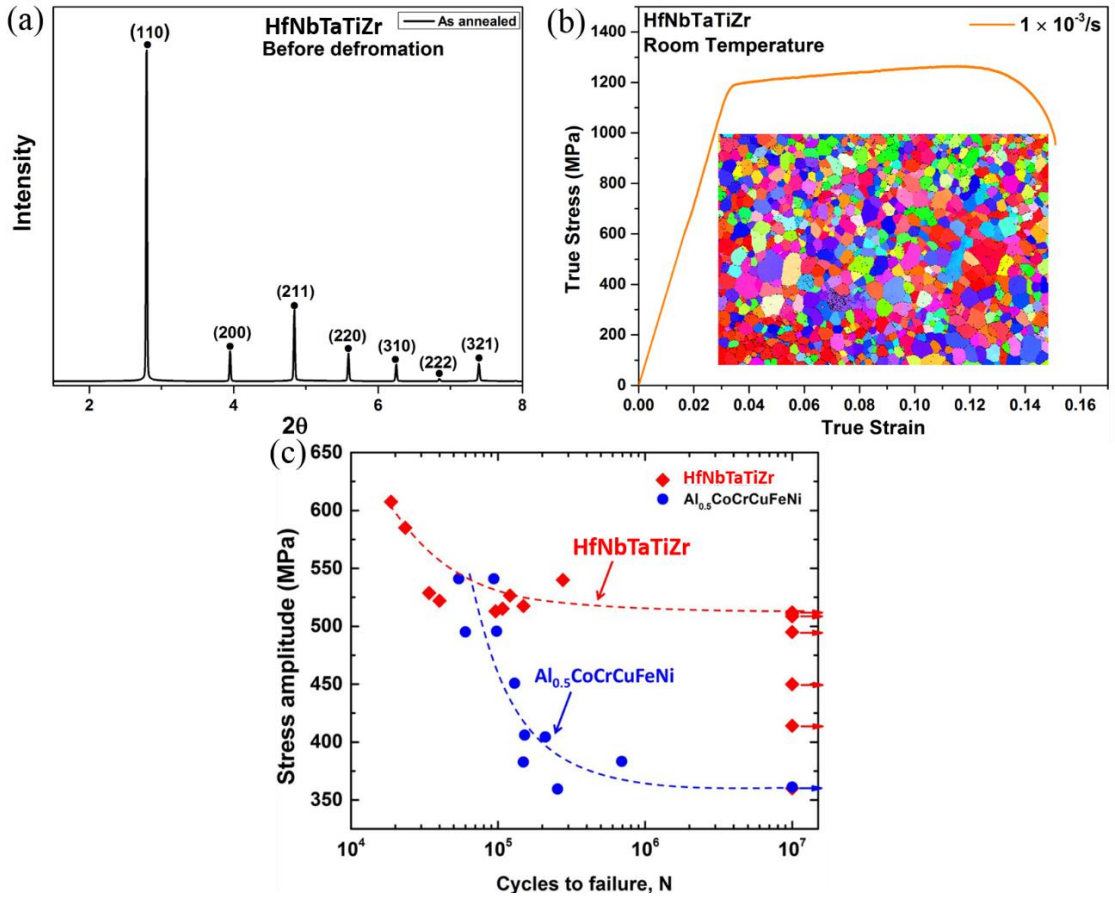

Figure 5. 1. (a) the microstructure before deformation; (b) the true stress-strain tensile curve at room temperature; (c) the S-N curve of HfNbTaTiZr HEA compared with $Al_{0.5}CoCrCuFeNi$ HEA

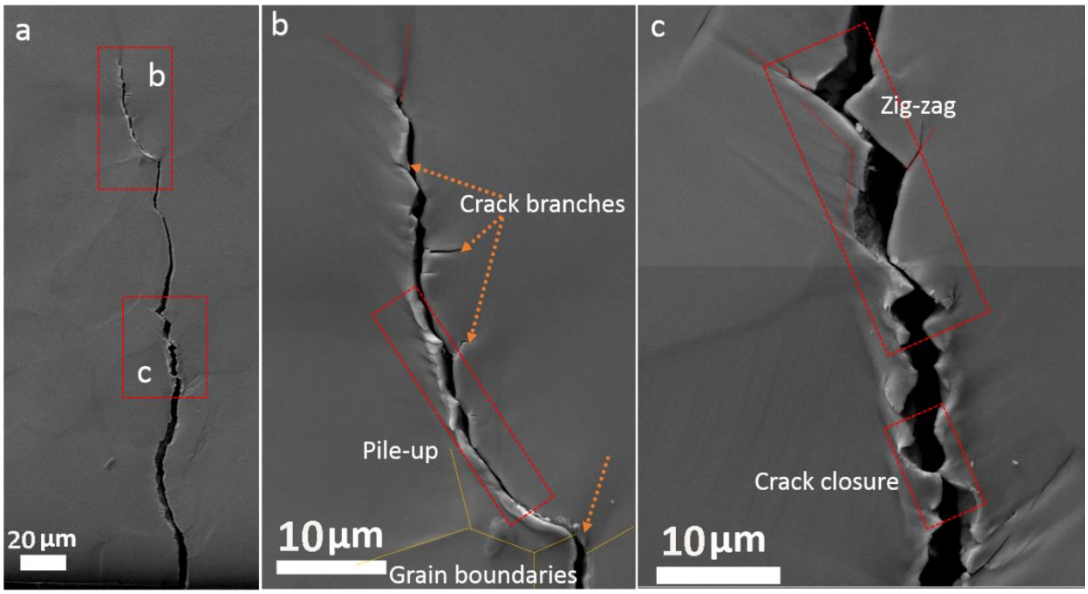

Figure 5. 2. (a-c)The SEM picture of crack propagation of post-fatigue specimen; (d, e) the EBSD image of slip plane during the crack propagation

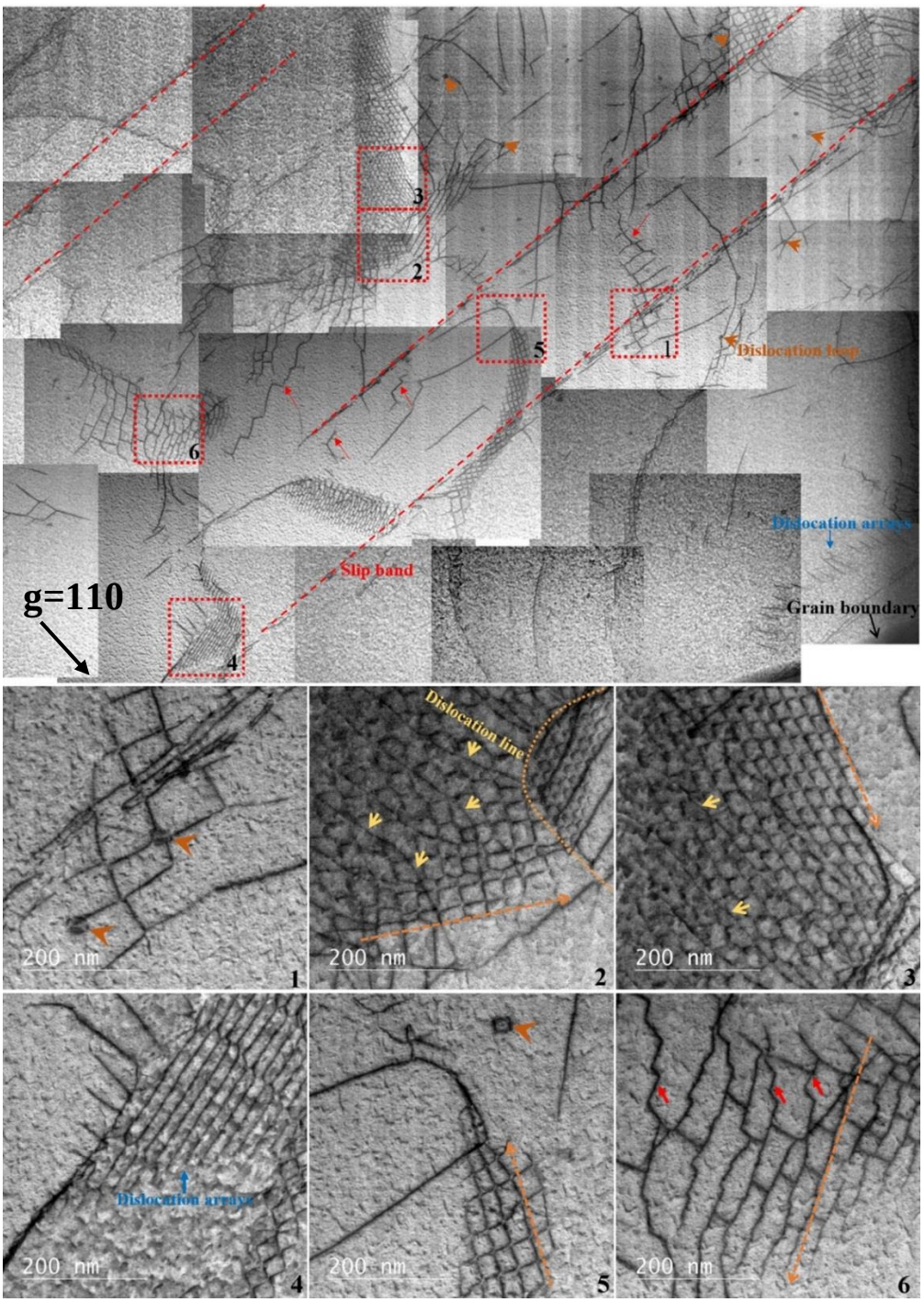

Figure 5. 3. The TEM image taken from the primary crack initiation site of sample deformed at σ_a = 522 MPa, characterized by the dislocation networks and dislocation cells. ZA=[111], g=[110]

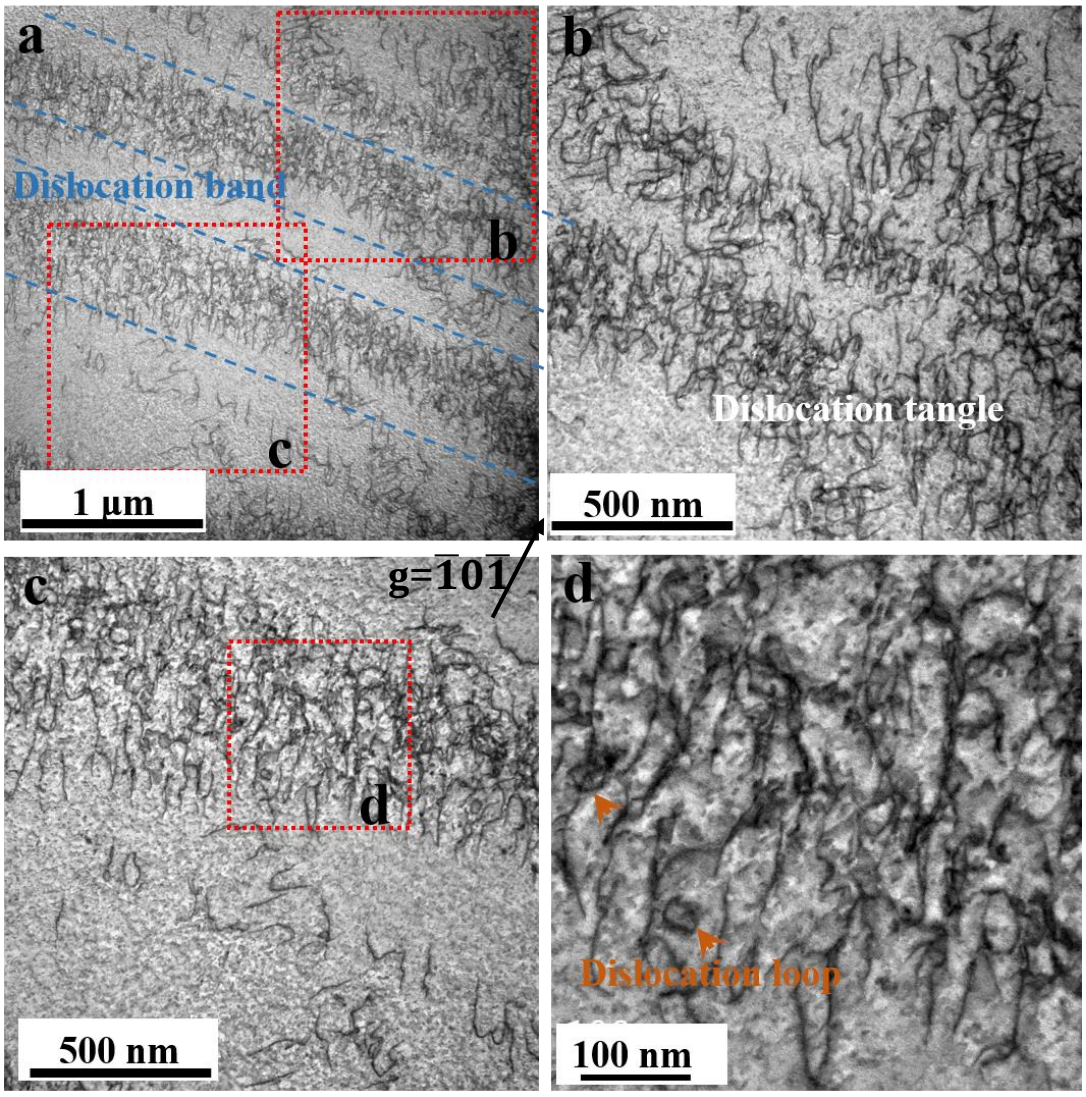

Figure 5. 4. (a) The TEM image taken from the primary crack initiation site of sample deformed at σ_a = 585 MPa, characterized by the dislocation tangles, dislocation loops, and curved dislocation lines. (b) and (c) is the magnification of band seen in a; (d) is a high magnification of the band seen in c.

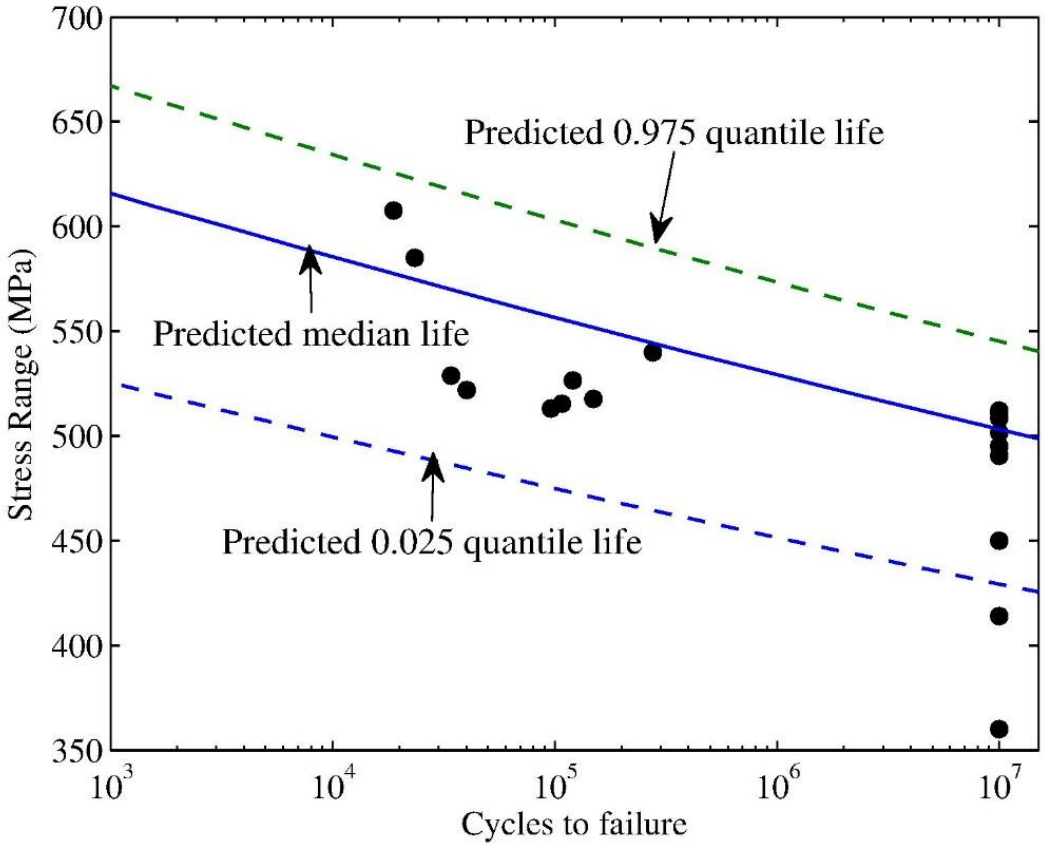

Figure 5. 5. The predicted quantile lives by the Weibull predictive model

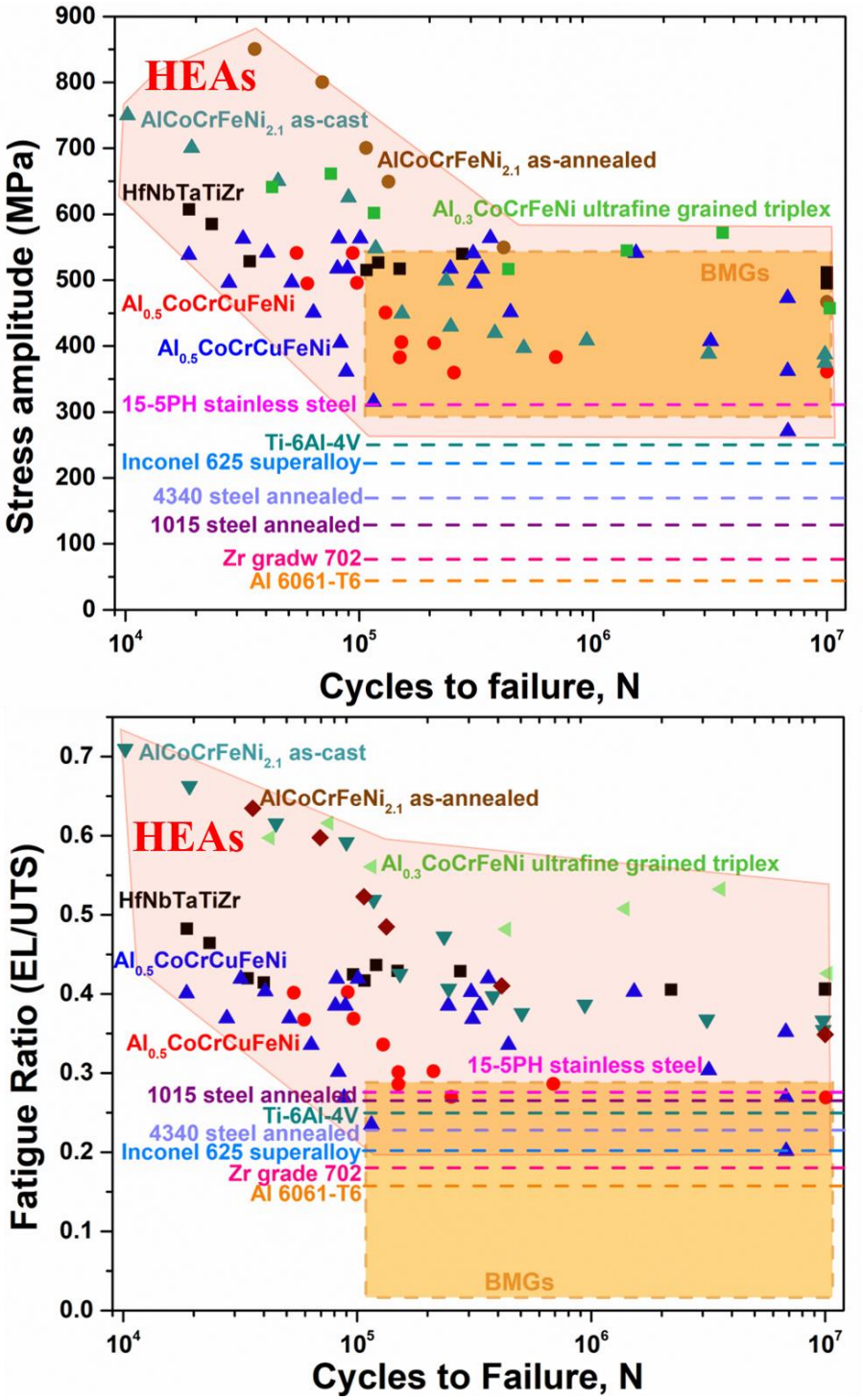

Figure 5. 6. S–N curves comparing (a) the fatigue-endurance limits at 10^7 cycles and (b) the fatigue ratios of the HfNbTaTiZr, $Al_{0.5}CoCrCuFeNi$ HEA, other conventional alloys, and BMGs. Colored dashed lines denote the endurance limit of each alloy.

CHAPTER VII FUTURE WORK

1. Investigate precipitation kinetics as well as to design a heat treatment route encompassing the chemical homogenization and precipitation hardening of the HEA.

2. Elaborate a valid thermodynamic and mobility database to allow the calculation of driving forces for precipitation and simulate other relevant morphological features using Thermo-Calc or Phase Field Models with the consideration of the effect of mechanical strains on the phase stability and phase selection of HEAs.

3. Conduct the TEM studies of the samples in tensile/fatigue experiments to investigate the dislocation evolution and reveal the deformation mechanism in a wide range of temperatures and further understand the serration behavior.

CHAPTER VIII CONCLUSIONS

1. The grain growth of the cast HfNbTaTiZr HEA, subsequent to cold-rolling and annealing at 1,000 – 1,200 ℃ for up to 24 hours, was investigated. Experimental results determine the grain-growth exponent and average activation energy to be n = 2.2 – 2.4 and Q_g = 303 kJ/mol, respectively. The higher activation energy relates with higher degree of disorder, i.e., more random state. Grain boundary migration needs the volume diffusion through the chemically-homogeneous lattice, whose rate is controlled by the slowest species, Nb and Ta. The grain-size strengthening follows the Hall-Petch relation in the form of $\sigma_y = 942+270D^{-0.5}$.

2. The temperature effect on the mechanical properties of the HfNbTaTiZr HEA was investigated by conducting uniaxial tensile tests in the temperature range from 77 to 673 K. The decrease of the yield strength with increasing temperature was mechanistically analyzed by considering contributions from various strengthening mechanisms, ultimately leading to an estimate of the dislocation width of $\omega_0 = 0.74b$, where b is the magnitude of the Burgers vector. An anomaly in strain hardening was observed at elevated temperatures – the strain-hardening exponent decreases expectedly from 77 K to 298 K but reverts to an anomalous ascending trend afterwards. Microstructural probing (Synchrotron diffractions, TEM, and APT) precludes precipitation hardening. Flow serrations at 673 K implies the dynamic strain aging (DSA) as an extra strengthening mechanism contributing to the intensified strain hardening at elevated temperatures. A model was constructed to split the overall strain hardening into forest hardening and DSA hardening, both of which were theoretically quantified at all temperatures considered

3. The crystal structure and microstructure of the homogenized HfNbTaTiZr alloy after annealing at different temperatures (550℃, 700 ℃, 900 ℃, and 1,000 ℃) for 96 h or at 700 ℃ for 2.5 h, 96 h, and 192 h are systematically investigated. The XRD/TEM study of the crystal structure and composition reveals that the HfNbTaTiZr RHEA decomposes into three phases, the BCC matrix, BCC Ta-Nb-rich and HCP Zr-Hf-rich precipitates;

4. The HfNbTaTiZr HEA with single BCC structure are investigated in four-point bending experiments and superior fatigue properties were presented from S-N curve, compared with the reported conventional alloys. The microstructure after fatigue experiments exhibits interesting features such as zig-zag, crack branch, crack closure, and crack deflection, which are important to enhance the fatigue behaviors. Additionally, a series of deformed substructure, including dislocation loops, jogs and dislocation network were formed after the cyclic loading. Among them, the dislocation network was formed by the interaction between dislocations with different Burgers vectors slipping on the same crystal plane, which can act as the obstacle to dislocation motion to strengthen the fatigue behavior and release the strain energy and stress concentration to improve the resistance to cyclic loading.

VITA

Shuying Chen was born in Taian, China. She obtained her B.S. degree from the Department of Materials Science and Engineering at University of Jinan, Jinan, China, 2011, and Master degree from the State key Laboratory of New Metal Materials at University of Science and Technology, Beijing, China, 2014. She became a graduate student in Materials Science and Engineering at University of Tennessee-Knoxville in Spring, 2014. She obtained his Ph.D. degree in May 2019.